Electronic transport properties of $YBa_2Cu_3O_{7-x}$ /$PrBa_2Cu_{2.9}Ga_{0.1}O_{7-y}$ trilayers and superlattices perpendicular to the layer structure

Dissertation
zur Erlangung des Grades
Doktor der Naturwissenschaften (Dr. rer. nat.)
am Fachbereich Physik
der Johannes Gutenberg-Universität Mainz

vorgelegt von
Hernán Rodríguez
geb. in Bogotá (Kolumbien)

Mainz, 2004
D77

Tag der Einreichung : 05.07.2004
Tag der mündliche Prüfung : 14.10.2004

Contents

List of Figures

List of Tables

Introduction

The study of the anisotropic properties and dimensionality in layered superconductors and artificially prepared superlattices go back to the middle of the 1970's [1, 2]. Superconducting superlattices show for example unusually high superconducting critical fields, when the external magnetic field is applied parallel to the layers [3]. Additionally, the superconducting coupling between the layers changes with the layer spacing. Such superlattices allow to tune the character of the system in a continuous way from where the layers are three dimensional and weak coupled, to where the layers are two dimensional but strongly coupled [4]. A dimensional crossover in the intermediate region takes place as a function of the temperature when the Ginzburg–Landau $\xi_{GL}(T)$ coherence length is comparable with the layer's separation [4]. Lawrence and Doniach [5] proposed a theory to explain the temperature and angular dependence of the upper critical field of layered superconductors coupled by the Josephson effect.

After the discovery of the cuprate superconductors, the topics: layered superconductors, vortex dynamics, proximity effect, interplay between superconductivity and magnetism obtained enormous interest. Different well–known techniques for the preparation of metallic and semiconducting films like evaporation, sputtering, laser ablation etc. were used for the growth of thin films and multilayers of these new materials. One task of investigations on the high temperature superconductor (HTSC) superlattices was the dimensionality. At the beginning it was assumed that the HTS phenomenon takes places completely within a single CuO_2 plane. In this case the HTSC's can be modeled as a two-dimensional electron gas (2DEG) with some in–plane interactions (i.e., phonons, magnons, etc.) but without any out–of–plane interactions between the planes. An alternative is to consider a 2DEG with some external interactions (i.e., a quasi two–dimensional system), for example via out–of–plane oxygen vibrations or phonons involving atoms of the neighborhood (intra–cell interactions). This question about "2D" or "3D" was investigated with superlattices which contain HTSC blocks sepa-

rated by non superconducting spaces of increasing thickness [6, 7]. A striking experiment which elucidate the quasi two–dimensional (Q2D) Josephson coupled nature was done by Kleiner *et al.* [8] by detecting microwave emission from a $Bi_2Sr_2CaCu_2O_{10+y}$ single crystal.

Probably $YBa_2Cu_3O_{7-x}$ /$PrBa_2Cu_3O_{7-y}$ is the most intensively investigated HTSC superlattice. This system provides a very interesting physical situation. Both $YBa_2Cu_3O_{7-x}$ and $PrBa_2Cu_3O_{7-y}$ are very similar from the view point of the crystallographic structure, however, their transport properties are very different. $PrBa_2Cu_3O_{7-y}$ is not metallic and its resistivity increases at low temperatures showing a semiconductor-like behavior. Moreover, its Pr atoms at low temperature exhibit antiferromagnetic (AFM) ordering. Therefore, such a compound is very suitable to study the role of the interplay coupling between $YBa_2Cu_3O_{7-x}$ layers separated by $PrBa_2Cu_3O_{7-y}$ spacers [6, 9] and the interplay between superconductivity and magnetism in $Y_{1-x}Pr_xBa_2Cu_3O_7$ compounds.

The discovery of the intrinsic Josephson effect in HTSC [10] showed that a $Bi_2Sr_2CaCu_2O_{10+x}$, single crystal represents a native superlattice of Josephson junctions in series, where the order parameter modulation length is less than the scale of the unit cell. This effect received great attention because of both applications in microelectronics and fundamental physics. This fact motivated a previous work of A. Schattke [11] in order to detect this effect in artificial (Y/Pr)$Ba_2Cu_3O_7$ superlattices and to study the effect of the modulation of the order parameter on the transport properties in such a system.

The aim of this work is the study of the transport properties perpendicular to the superconducting CuO_2 planes in artificially prepared $YBa_2Cu_3O_{7-x}$ / $PrBa_2Cu_{3-p}Ga_pO_7$/$YBa_2Cu_3O_{7-x}$ trilayers and superlattices with $p = 0$ and $p = 0.1$ and their dependence on the preparation conditions, in particular on the substrate temperature during the deposition.

The first chapter of this work presents a summary of the electron tunneling theory and the Josephson effect, thereafter, the theoretical basis of inhomogenous superconductors are discussed, where the order parameter is spatially modulated. The central point is the Bogoliubov–de Gennes equations and their applications on such systems.

Details about the sample preparation are presented in chapter two. An important aspect of this work is the preparation of high quality HTSC multilayers with different modulations. This demands the control of the layers growth of the order of less than one unit cell. X-ray diffraction (XRD) constitutes an important tool

to check not only the modulation but also the structure of superlattices. Results of XRD together with their simulations are presented in this chapter. In order to measure the c–axis transport properties of $YBa_2Cu_3O_{7-x}/PrBa_2Cu_3O_{7-y}$trilayers and superlattices, it is necessary to pattern the multilayers into mesa structures, this procedure represents an essential part in this work, details are also presented in this chapter.

The third chapter concentrates on electrical transport measurements on trilayers. In order to study the influence of the deposition temperature on the transport properties, series of trilayers deposited at 840°C and 760°C were prepared. The tunneling conductance characteristics are discussed in the framework of the Blonder–Tinkham–Klapwijk and Anderson–Appelbaum theories.

The chapter four follows the scheme of the previous chapter on superlattices. The in–plane and out–of–plane transport properties of series of superlattices with different modulations prepared at 840°C and 760°C are presented in this chapter. The chapter five gives results on Raman spectroscopy of $(Y/Pr)Ba_2Cu_3O_7$ superlattices. The interplay between superconductivity and antiferromagnetism is discussed in this chapter. This work ends with a summary.

Chapter 1

Theoretical background

1.1 Superconductivity

The central idea of the BCS theory [12] was proposed by Cooper. He showed that a T = 0 K the ground state of an electron gas becomes unstable if an arbitrarily weak attraction between electrons near the Fermi surface exists. The origin of this attraction is due to the electron–phonon interaction. The crystal lattice responds to the motion of the conduction electrons creating a phonon i.e., a lattice polarization due to the ionic displacement around an electron. Since the characteristic phonon frequency is much lower than the plasma frequency in a metal $\omega_{ph} \ll \omega_0$, the electron leaves always a positive "cloud" behind. Such a cloud can interact with another electron, creating in this way an effective electron–electron interaction. An indication for this mechanism came from the "isotope effect". The transition temperature of metallic samples formed from different isotopes of the same element depends on the mass M of the lattice ions according to the law $T_c \propto M^{-\alpha}$ with $\alpha = 1/2$ (weak coupling). A new class of superconductors, the so–called High Temperature Superconductors (HTSC) exhibits zero isotope effect or α–values much less than conventional superconductors. The substitution ^{135}Ba$\rightarrow$ ^{138}Ba and ^{63}Cu$\rightarrow$ ^{65}Cu in $YBa_2Cu_3O_{7-x}$results in practically zero isotope effect, while the substitution $^{18}O \rightarrow {}^{16}O$ produces a change in the critical temperature ΔT_c between 0.3 K and 0.5 K. So the isotopic effect in HTSC is vanishing or much less than in ordinary superconductors, this is an argument against a phonon mediated mechanism of superconductivity in this class of materials [13, 14].

However, in the framework of the standard BCS–theory it is not possible to account the simultaneous occurrence of a high T_c and a small α. This theory was

developed for Fermi–liquid like metals and it has been successful in describing the conventional superconductors but it does not seem to have the appropriate foundation for the description of the HTSC. Other physical origins have been proposed to explain the pairing mechanisms e.g. spin fluctuation models, resonance valence bonding, marginal Fermi liquids, stripes etc., [15] but until now a theory that explains satisfactorily the mechanism causing the high T_c in these material has not been established.

1.2 Electron tunneling theory

A tunnel junction consists of two metallic electrodes separated by a thin dielectric barrier. From the point of view of the quantum mechanics, a tunneling junction can be described by the following hamiltonian [16, 17]

$$\mathcal{H} = \mathcal{H}_1 + \mathcal{H}_2 + \mathcal{H}_T. \tag{1.1}$$

Standing waves on both sides of the barrier can be described with $\mathcal{H}_1$ and $\mathcal{H}_2$ respectively. The barrier can be regarded as separating the whole system in two parts, so that the last term on the right is the tunneling interaction term which transfers electron from one metal to the other. The coupling part has the following form

$$\mathcal{H}_T = \sum_{\vec{k}\vec{q}\sigma} [\, T_{\vec{k}\vec{q}} c^{\dagger}_{\vec{k}\sigma} c_{\vec{q}\sigma} + h.c.], \tag{1.2}$$

where $T_{\vec{k}\vec{q}}$ represent a phenomenological tunneling matrix element. The charge transfer probability decays exponentially with the distance of separation and it depends on the insulating material and the transition probability i.e., the current is proportional to the square of the matrix element.
A simple scheme to visualize the tunneling characteristic of various types of junctions is the so–called "semiconductor model" (Fig. 1.1). The *I–V* characteristic of *NIS* and *SIS* junctions can be described assuming for the superconducting part a density of states symmetrically split about the Fermi level. At T = 0 K all states below the Fermi level are filled whereas for T > 0 K the occupation numbers are given by the Fermi function. When both electrodes are in the normal state, the expression for the tunneling current is

$$I_{NN} = A|T'|^2 \int_{-\infty}^{\infty} N_1(E) N_2(E + eV) [\, f(E) - f(E - eV)] dE,$$

where $f(E)$ is the Fermi function, V is the applied voltage across the junction, T' is the tunneling matrix element, which is assumed to be constant and $N_{1(2)}$ is the density of states in the 1(2) metal. For energies close to the Fermi energy one can take $N_{1(2)}(E) \approx$ constant. The application of a bias voltage shifts the densities of states relative to each other, thus a tunneling process involves the creation of two excitations, a hole in one metal and an electron in the other.

If one of the metal is in the superconducting state, its density of states is given by

$$N(E) \approx \begin{cases} N(0)\frac{|E|}{\sqrt{E^2-\Delta^2(E)}} & \text{for} \quad |E| \geq \Delta \\ 0 & \text{for} \quad |E| < \Delta, \end{cases} \tag{1.3}$$

the expression for the tunneling current across the junction becomes

$$I_{SN} = A|T'|^2 N_1(0)N_2(0) \int_{-\infty}^{\infty} \frac{|E|}{\sqrt{E^2-\Delta^2}}[\, f(E) - f(E-eV)]dE \tag{1.4}$$

(this integral excludes the range $|E| \leq \Delta$). At T = 0 K there is no tunneling current until $e|V| > \Delta$ (see Fig. 1.1), however, for T > 0 K the energy of the excitations already present allows that a current can flow at lower voltages. By

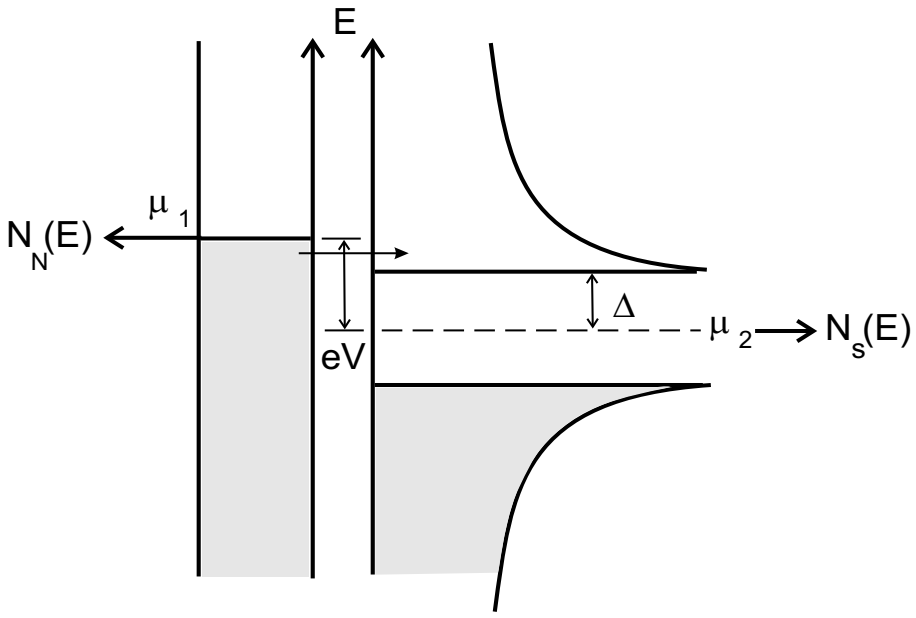

Figure 1.1: Representation of the normal metal–insulator–superconductor tunneling process in the semiconductor model. The density of states is plotted horizontally vs. energy vertically. The horizontal arrow denotes electrons tunneling form occupied states in the left into empty states on the right when the bias $eV > \Delta$. Taken from Ref. [18].

considering tunneling between two superconductors, the expression for the current $I_{SS'}$ is similar to the equation (1.4) but with the product of the superconducting densities of states of both metals

$$I_{SS'} = \frac{G_{NN}}{e}\int_{-\infty}^{\infty}\frac{|E|}{\sqrt{E^2-\Delta_1^2}}\frac{|E+eV|}{\sqrt{(E+eV)^2-\Delta_2^2}}[\,f(E)-f(E-eV)]dE, \quad (1.5)$$

where the conductance is $G_{NN} = A|T'|^2 N_1(0)N_2(0)e$. The range of integration of (1.5) excludes values of the energy such $|E| < |\Delta_1|$ and $|E+eV| < |\Delta_2|$. At T = 0 K no current can flow until $eV = \Delta_1 + \Delta_2$. At T > 0 K a current can also flow at lower voltages because of the existence of thermally excited quasiparticles. For instance the current reaches a maximum at $eV = |\Delta_1 - \Delta_2|$. The existence of features at both $|\Delta_1 - \Delta_2|$ and $\Delta_1 + \Delta_2$ allows the determination of $\Delta_1(T)$ and $\Delta_2(T)$ from the tunneling curves.

1.3 The Josephson equations

The phase dependence of the tunnel supercurrent between two weakly coupled superconductors is known as the Josephson effect. It was predicted in 1962 by B. D. Josephson [19]. Later Feynman showed that a single Josephson junction can be seen as a coupled two–level quantum system.

In a superconductor–barrier–superconductor structure, each superconductor can be described by a macroscopic wave function

$$\psi_1(\vec{r}) = \sqrt{\rho_1(\vec{r})}e^{i\gamma_1(\vec{r})} \qquad \psi_2(\vec{r}) = \sqrt{\rho_2(\vec{r})}e^{i\gamma_2(\vec{r})} \quad (1.6)$$

for the left and right side respectively. ρ represents the actual Cooper pair density and γ is the phase of the wave function. If the coupling between the two superconductors across the barrier is weak, an exchange of Cooper pairs between both systems can occur. The temporal evolution of the system is described by a Schrödinger equation

$$i\hbar\dot{\psi} = \mathcal{H}\psi, \quad (1.7)$$

here $\mathcal{H}$ is given by (1.1), $\mathcal{H}_{1(2)}$ is the operator of the unperturbed state on the left(right) side and $\mathcal{H}_T$ represent the interaction between them. After Feynman [20] the Hamiltonian associated with the system is the following

$$\mathcal{H}_0 = (\psi_1^*, \psi_2^*)\begin{pmatrix} E_1 & K/2 \\ -K/2 & E_2 \end{pmatrix}\begin{pmatrix}\psi_1 \\ \psi_2\end{pmatrix} \quad (1.8)$$

where K is a positive constant and depends on the barrier properties like: thickness, height, geometry etc.
If a d.c. potential difference V exists across the junction, the chemical potentials are shifted relative to each other by the quantity $E_1 - E_2 = e\mathrm{V}$. After a simple calculation one obtains, the first Josephson equation

$$J = J_0 sin(\gamma), \tag{1.9}$$

where $\gamma = \gamma_1 - \gamma_2$ is the phase difference between the two superconductors and J_0 for the maximal Josephson current, and the second Josephson equation which connects the phase changes with an externally applied voltage

$$\frac{\partial \gamma}{\partial t} = \frac{2eV}{\hbar}. \tag{1.10}$$

Assuming $V = 0$ V, the phase difference in (1.10) is constant (not necessarily zero), so that a finite current J_0 can flow through the barrier with zero voltage drop. This is the so–called "d.c. Josephson effect". From the analysis of the *SN* junctions in section 1.6 it is simple to have an alternative picture of such an effect. Since an incoming electron is reflected as a hole into the metal, and a Cooper pair is generated into the superconductor if its energy is less than Δ, the Josephson effect can be viewed as the result of multiple Andreev reflections of two *SN* interfaces joined together. On the other hand, if a constant voltage $V \neq 0$ is applied, an integration of Eq.(1.10) results in the phase γ varying in time as $\gamma = \gamma_0 + 2eVt/\hbar$. The first Josephson equation becomes:

$$J = J_0 sin(\gamma_0 + \omega t), \tag{1.11}$$

an alternating supercurrent flows through the Josephson junction with an angular frequency $\omega = 2eV/\hbar$. In other words, a photon of energy $\hbar\omega = 2eV$ is either emitted or absorbed when an electron pair crosses the barrier. This is called "a.c. Josephson effect".

1.4 RCSJ Model

The RCSJ model (Resistively and Capacitively Shunted Junction) [18] was proposed to characterize a weak link for finite voltages. The Josephson junction is described then by a circuit of an ideal Josephson junction, a resistance and capacitor in parallel (Fig. 1.2). If a d.c. current is applied across the system, the

total current from the three parallel channels is

$$I = I_c\, sin\gamma + V/R_n + CdV/dt, \tag{1.12}$$

using the second Josephson equation, a second order differential equation for γ is

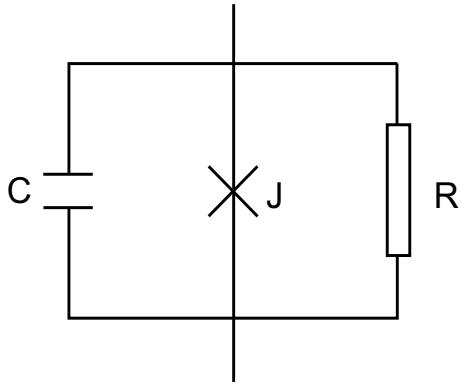

Figure 1.2: RCJS circuit for a Josephson junction.

obtained. For simplicity one can introduce the dimensionless parameters *plasma frequency* $\omega_P = (2eI_c/\hbar C)^{1/2}$ and the variable $\tau = \omega_P t$ resulting in

$$\frac{d^2\gamma}{d\tau^2} + \frac{1}{\sqrt{\beta_c}}\frac{d\gamma}{d\tau} + sin\gamma = \frac{I}{I_c}, \tag{1.13}$$

where $\beta_c = (2e/\hbar)I_c C R_n^2$ is the McCumber parameter. For the general case this equation cannot be solved analytically. However, two limiting cases can be discussed.

For $\beta_c \ll 1$ (overdamped case) i.e., the capacitance is small, the equation (1.13) is reduced to a first–order differential equation. One finds for the time averaged voltage across the junction:

$$V = \begin{cases} 0 & \text{for} \quad I < I_c \\ I_c R_n \sqrt{(I/I_c)^2 - 1} & \text{for} \quad I > I_c \end{cases} \tag{1.14}$$

for $I \gg I_c$, V tends to IR_n i.e., the Ohm's law (Fig. 1.3).

When C is large enough $\beta_c > 1$ (underdamped case) and for $I < I_c$ two solutions result i.e., the I–V curve becomes hysteretic. Increasing I from zero, flows a supercurrent without voltage drop until I_c, then V jumps discontinuously from zero up to a finite voltage $I_c R$ which correspond to the energy gap 2Δ. Decreasing the current from $I > I_c$ the junction remains in the resistive state even for $I < I_c$. When the return current is lower than I_r the zero–voltage state will be reached again.

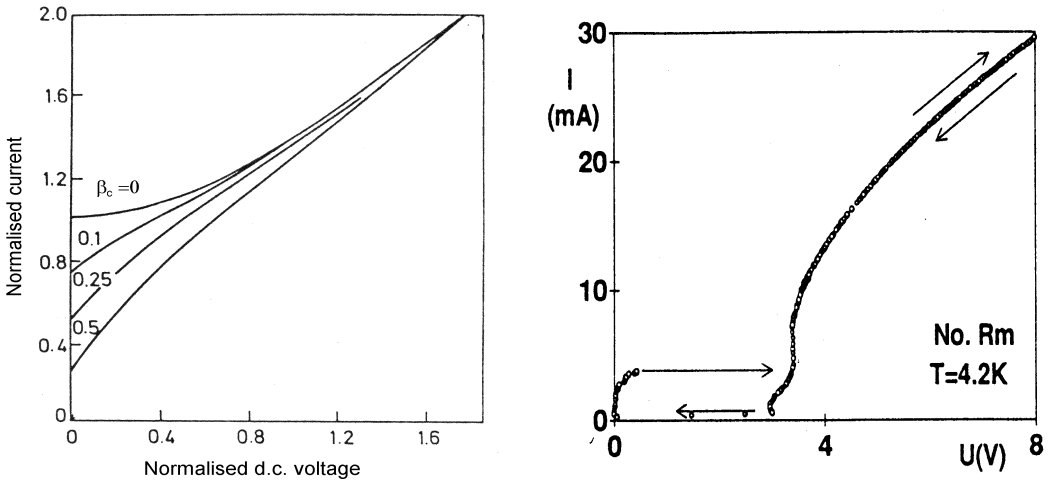

Figure 1.3: Typical d.c. current–voltage characteristic of a *SIS* junction for different β_c values (left). From Ref. [21]. If the capacitance is large ($\beta > 1$) the I–V characteristic becomes hysteretic (right). The I–V curve exhibits a tunneling curve with a gap value 3.4 V. This correspond to a $Bi_2Sr_2CaCu_2O_{10+y}$ single crystal which contains about 1000 Josephson junctions in series. From Ref. [10].

1.5 The Bogoluibov de Gennes equations

In order to get the BCS hamiltonian one starts with the hamiltonian [22]

$$\begin{aligned}\mathcal{H} &= \int d^3r\, \psi_\alpha^+(\vec{r}) \left[\frac{1}{2m}(\vec{p} - \frac{e}{c}\vec{A})^2 + U(\vec{r}) - \mu\right] \psi_\beta(\vec{r}) - \\ &\quad - \frac{\lambda}{2} \int d^3r\, \psi_\alpha^+(\vec{r})\psi_\beta^+(\vec{r})\psi_\beta(\vec{r})\psi_\alpha(\vec{r}),\end{aligned} \tag{1.15}$$

where ψ_σ is a field operator of electrons with spin σ, U the periodic potential, μ the chemical potential, $\vec{A}$ is the vector potential and λ is a coupling constant of electron–electron attraction. The first term describes free electrons and the second one, the attractive electron–phonon interaction between electrons with both opposite spin and impulse. Since this interaction is due to phonons only electrons with energy $|\varepsilon_{\vec{k}}| < \hbar\omega_D$ are allowed. Here ω_D is the Debye frequency. If the second term is replaced by an average potential (mean field approximation), the effective hamiltonian has the following form

$$\begin{aligned}\mathcal{H}_{eff} &= \sum_\sigma \int d^3r\, \psi_\sigma^+(\vec{r})\, \mathcal{H}_e\, \psi_\sigma(\vec{r}) - \\ &\quad - \int d^3r[\Delta(\vec{r})\psi_\alpha^+(\vec{r})\psi_\beta^+(\vec{r}) + \Delta^*\psi_\beta(\vec{r})\psi_\alpha(\vec{r})] + \int d^3r\, |\Delta(\vec{r})|^2\,,\end{aligned} \tag{1.16}$$

where

$$\mathcal{H}_e = \frac{1}{2m}\left(\frac{\hbar}{i}\vec{\nabla} - \frac{e}{c}\vec{A}(\vec{r})\right)^2 + U(\vec{r}) - \mu. \tag{1.17}$$

The simplest case is one where μ is constant and $U(\vec{r}) = 0$, $\vec{A} = 0$, which results

$$\mathcal{H}_e = \frac{\hbar^2 k^2}{2m} - \mu. \tag{1.18}$$

$\Delta(\vec{r})$ is defined as the superconducting order parameter and should satisfy the self–consistency condition

$$\Delta(\vec{r}) = \lambda \left\langle \psi_\alpha(\vec{r})\psi_\beta(\vec{r})\right\rangle, \tag{1.19}$$

the quantity in brackets represents the thermal average. The hamiltonian (1.16) can be diagonalized using a unitary transformation, the so–called Bogoliubov transformation, which expresses the field operators $\psi_\alpha(\vec{r})$, $\psi_\beta(\vec{r})$ in terms of new creation and annihilation Fermi operators

$$\begin{aligned}\psi_\alpha(\vec{r}) &= \sum_n [\gamma_{n\alpha} u_n(\vec{r}) - \gamma^+_{n\beta} v^*_n(\vec{r})] \\ \psi_\beta(\vec{r}) &= \sum_n [\gamma_{n\beta} u_n(\vec{r}) + \gamma^+_{n\alpha} v^*_n(\vec{r})],\end{aligned} \tag{1.20}$$

these operators are related to the destruction and creation operator for quasiparticles as

$$\gamma^+_{\vec{k}\alpha} = u_{\vec{k}} c^+_{\vec{k}\alpha} - v_{\vec{k}} c_{-\vec{k}\beta}, \quad \gamma^+_{\vec{k}\beta} = u_{\vec{k}} c^+_{\vec{k}\beta} + v_{\vec{k}} c_{-\vec{k}\alpha}. \tag{1.21}$$

The new operators obey the following commutation relations

$$\left\{\gamma^+_{n\alpha}, \gamma_{m\beta}\right\} = \delta_{mn}\delta_{\alpha\beta}, \quad \{\gamma_{n\alpha}, \gamma_{m\beta}\} = 0, \tag{1.22}$$

and the functions $u(\vec{r})$, $v(\vec{r})$ are associated to electrons and holes respectively.

The diagonalization requires that u and v satisfy the Bogoliubov–de Gennes equations (BdG)

$$\begin{aligned}\mathcal{H}_e\, u_n(\vec{r}) + \Delta(\vec{r}) v_n(\vec{r}) &= E_n u_n(\vec{r}) \\ -\mathcal{H}^*_e\, v_n(\vec{r}) + \Delta^*(\vec{r}) u_n(\vec{r}) &= E_n v_n(\vec{r}),\end{aligned}$$

we can write these equations in a matrix form,

$$\begin{pmatrix} \mathcal{H}_e & \Delta(\vec{r}) \\ \Delta^*(\vec{r}) & -\mathcal{H}^*_e \end{pmatrix} \begin{pmatrix} u_n(\vec{r}) \\ v_n(\vec{r}) \end{pmatrix} = E \begin{pmatrix} u_n(\vec{r}) \\ v_n(\vec{r}) \end{pmatrix}. \tag{1.23}$$

The Bogoliubov–de Gennes equations are Schrödinger–like equations for electrons and holes coupled by the superconducting pair potential[1] $\Delta(\vec{r})$. The applicability of the Bogoliubov–de Gennes equations can be found in non–homogeneous superconductors where the pair potential spatially changes. For example in the mixed state of the type II superconductors, in mesoscopic systems where the mean free path of the BCS-like quasiparticles excesses the extension of regions, where the superconducting order parameter deviates significantly from its maximum value Δ etc. The equations (1.23) are also the starting point to describe Andreev reflections on superconductor–normal (SN) interfaces, zero–bias anomalies and are considered in the study of SN microconstriction contacts in the Bonder–Tinkham–Klapwijk theory.
According to Ref. [23] two kinds of continuity equation for probability and charge are introduced which are satisfied by the solutions of the Bogoliubov–de Gennes equations. The first one is the probability density for finding either an electron or a hole at a particular time and place $P(\vec{r},t) = |u|^2 + |v|^2$. Using the equations (1.23) to evaluate $\partial P/\partial t$, one obtains

$$\frac{\partial P}{\partial t} + \vec{\nabla} \cdot \vec{J}_P = 0, \tag{1.24}$$

where

$$\vec{J}_P = \frac{\hbar}{m} Im \left[u^*(\vec{r}) \vec{\nabla} u(\vec{r}) - v^*(\vec{r}) \vec{\nabla} v(\vec{r}) \right], \tag{1.25}$$

the hole current in this equation has an opposite sign to that of electron part.

The second equation is related to the conservation of the electric charge. Assigning a unit charge $-e$ to the electron and $+e$ to the hole, the net charge density is $Q = -e(|u|^2 - |v|^2)$. Using the Eqs. (1.23) again result

$$\frac{\partial Q}{\partial t} + \vec{\nabla} \cdot \vec{J}_Q = -\frac{4e\Delta(\vec{r})}{\hbar} Im \left[u^*(\vec{r}) v(\vec{r}) \right], \tag{1.26}$$

where

$$\vec{J}_Q = -\frac{e\hbar}{m} Im \left[u^*(\vec{r}) \vec{\nabla} u(\vec{r}) + v^*(\vec{r}) \vec{\nabla} v(\vec{r}) \right]. \tag{1.27}$$

The term on the right in Eq. (1.26) is a source (drain) term connecting the quasiparticles with the condensate. An interchange of currents occurs in a normal–superconductor interface as will be shown in the next section.

[1] In a normal metal $\Delta(\vec{r}) = 0$.

1.6 Andreev reflections

This section is intented to consider an application of the Bogoliubov–de Gennes equations to the case of a superconductor and a normal metal (SN) interface. This should be considered like a quantum point contact between a superconductor ($x > 0$) and a normal metal ($x < 0$) [23]. For this case the order parameter is given

$$\Delta(x) = \begin{cases} 0 & x < 0 \\ \Delta_0 & x > 0. \end{cases} \tag{1.28}$$

The equations (1.23) have four kinds of plane–waves solutions in the normal region ($x < 0$) corresponding to incoming (from left to right) and outgoing (from right to left) electrons and holes to the interface

$$\begin{pmatrix} u(x) \\ v(x) \end{pmatrix} = \begin{pmatrix} 1 \\ 0 \end{pmatrix} e^{\pm i q_e x} \text{ and } \begin{pmatrix} 0 \\ 1 \end{pmatrix} e^{\pm i q_h x}, \tag{1.29}$$

where the wavenumber q_e and q_h for electrons and holes are given by

$$\hbar q_e = \sqrt{2m(\mu + E)} \quad \text{and} \quad \hbar q_h = \sqrt{2m(\mu - E)}, \tag{1.30}$$

here μ is the chemical potential. On the other hand, in the superconducting region ($x > 0$) there are also four kinds of plane–wave solutions for $E > \Delta_0$ given by

$$\begin{pmatrix} u(x) \\ v(x) \end{pmatrix} = \begin{pmatrix} u_0 \\ u_0 \end{pmatrix} e^{\pm i k_e x} \quad \text{and} \quad \begin{pmatrix} v_0 \\ u_0 \end{pmatrix} e^{\pm i k_h x} \tag{1.31}$$

here the wavenumber k_e and k_h are defined as

$$\hbar k_e = \sqrt{2m(\mu + \Omega)}, \quad \hbar k_h = \sqrt{2m(\mu - \Omega)} \tag{1.32}$$

with $\Omega = \sqrt{E^2 - \Delta_o^2}$ and

$$u_o = \sqrt{\frac{1}{2}(1 + \frac{\Omega}{E})}, \quad v_o = \sqrt{\frac{1}{2}(1 - \frac{\Omega}{E})}. \tag{1.33}$$

The wave function describing the scattering of an electron coming from the normal side should consist of an incoming plane wave and four outgoing plane waves

$$\psi(x) = \begin{pmatrix} u(x) \\ v(x) \end{pmatrix} = \begin{cases} \binom{1}{0} e^{i q_e x} + a \binom{0}{1} e^{i q_h x} + b \binom{1}{0} e^{-i q_e x} & x < 0 \\ \\ c \binom{u_0}{v_0} e^{i k_e x} + d \binom{v_0}{u_0} e^{-i k_h x} & x > 0. \end{cases} \tag{1.34}$$

Substituting these $u(x)$ and $v(x)$ functions into (1.25) yields

$$J_P = \begin{cases} \frac{\hbar q_e}{m}(1-|b|^2) - \frac{\hbar q_h}{m}|a|^2 & x<0 \\ \\ \Theta(E-\Delta_0)\left(\frac{\hbar k_e}{m}|c|^2 + \frac{\hbar k_h}{m}|d|^2\right) & x>0, \end{cases} \tag{1.35}$$

where $\Theta(x)$ is the Step function. From the equation (1.35) one can see clearly the meaning of each term of the wave function (1.34). An incoming electron wave $e^{iq_e x}$ is reflected at the barrier as a hole $a\,e^{iq_h x}$ and an electron $b\,e^{-iq_e x}$ with the probability $|a|^2$ and $|b|^2$ respectively. The reflection of an electron into a hole is called Andreev Reflection. The probability that an Andreev Reflection takes place is given by $q_h/q_e\,|a|^2$. For $E < \Delta_0$ the quasiparticle current in the superconductor is zero i.e., there is no quasiparticle excitation in gap.

The coefficients a, b, c and d are determined from the boundary conditions at $x = 0$ i.e., the continuity of the function ψ and its derivate $d\psi/dx$. In the case where $E \ll \mu$ and $\Delta_0 \ll \mu$, the values of q_e, q_h of (1.30) and k_e, k_h of (1.32) are comparable, one may set $q_e \approx q_h \approx k_e \approx k_h \approx k_F$, where k_F is the wave number of an electron at the Fermi surface. One obtains

$$a = \frac{v_0}{u_0}, \quad b = 0, \quad c = \frac{1}{u_0}, \quad d = 0, \tag{1.36}$$

with these values the electrical current (Eq. 1.27) becomes

$$J_Q = \begin{cases} 0 & E < \Delta_0 \\ -2ev_F\frac{E}{\Omega+E} & E > \Delta_0, \end{cases} \tag{1.37}$$

where v_F is the Fermi velocity. For $E \gg \Delta_0$ and for $x > 0$ the electric current J_Q becomes $-ev_F$, implying that an incoming electron can transmit into the superconductor without reflection as an electron–like particle. But on the other hand, for $E < \Delta_0$, J_Q becomes

$$J_Q = \begin{cases} -2ev_F & x<0 \\ -2ev_F exp(-2x\sqrt{\Delta_0^2 - E^2}/\hbar v_F) & x>0. \end{cases} \tag{1.38}$$

The electrical current in the normal region is twice the value as in the normal state $-ev_F$ but in the superconductor region J_Q decays exponentially with x, however the supercurrent (from Eq.1.26) carried by the condensate is

$$J_S = 2ev_F(1 - e^{-2\sqrt{\Delta^2 - E^2}x/\hbar v_F}). \tag{1.39}$$

In other words, when an electron with energy $E < \Delta_0$ transmits into the superconductor, it necessary condenses into a Cooper pair with another electron which leaves a hole running back to the normal metal (Fig. 1.4). Thus, the net current in the metal is $(-e)v_F - (+e)v_F = -2ev_F$ but the current carried by a Cooper pair in the superconductor region is $2ev_F$.

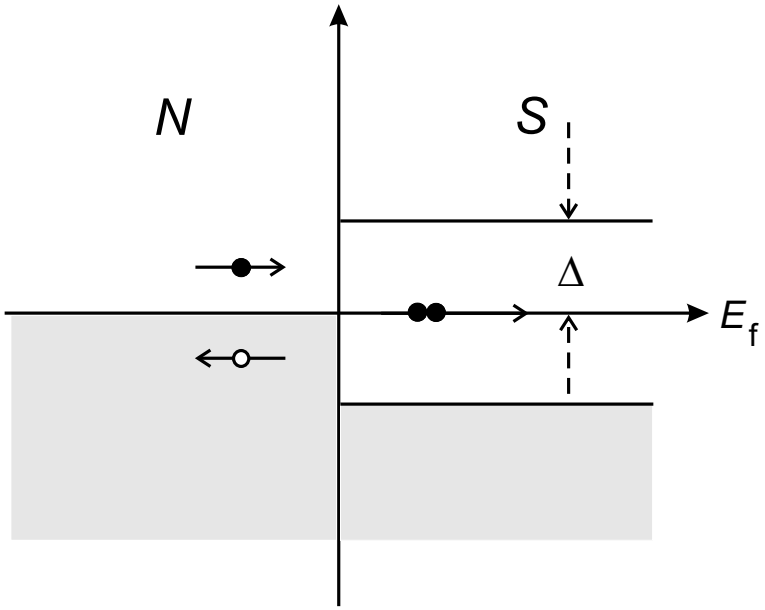

Figure 1.4: Schematic representation of the Andreev reflection. If the energy of the incident electron E referred to the Fermi energy E_F is smaller than the energy gap Δ, the electron is reflected as a hole in the normal (N) region and a Cooper pair is transmitted into the superconducting (S) region.

1.7 Inhomogeneous superconductors

An example for an inhomogeneous superconductor is a mixed state of a type II superconductor, where the normal region correspond to the inner part of a vortex. The first attempt to study the excitation spectrum of such a system was considered by A. P. van Gelder [24] and Kümmel [25], who used a Kronig–Penney model for the pair potential. Basically they calculated the eigenvalues of the Bogoliubov–de Gennes equations, in particular they considered

$$\Delta(\vec{r}) = \begin{cases} 0 & \text{if} \quad -a < z < 0 \\ \Delta_0 & \text{if} \quad 0 < z < b \end{cases} , \tag{1.40}$$

a and b represent the normal and superconducting regions respectively. Furthermore, $\Delta(\vec{r})$ must be periodic with $d = a + b$ and, for the one dimensional case is invariant with x and y. In order to solve the equations (1.23) $u(\vec{r})$ and $v(\vec{r})$ can be expressed as

$$\begin{pmatrix} u(\vec{r}) \\ v(\vec{r}) \end{pmatrix} = e^{i\vec{k}_\rho \cdot \vec{\rho}} \begin{pmatrix} u(z) \\ v(z) \end{pmatrix}, \tag{1.41}$$

$\vec{k}_\rho = k_x\hat{\imath} + k_y\hat{\jmath}$ is the wave vector of propagation parallel to the SN interface and $\vec{\rho} = x\hat{\imath} + y\hat{\jmath}$. Moreover, the equations for holes and electrons have to satisfy the periodicity condition

$$\begin{pmatrix} u(z+d) \\ v(z+d) \end{pmatrix} = e^{i\kappa d} \begin{pmatrix} u(z) \\ v(z) \end{pmatrix}, \tag{1.42}$$

where κ is the Bloch wave number. After taking into account the boundary condition of continuity of $u(z)$, $v(z)$ and their derivatives at the NS interface at $z = 0$ and $z = -a$ one obtains

$$cos[(\kappa - k_F)d/w] = F(\varepsilon, w), \tag{1.43}$$

this condition implies the appearance of bands of energy, separated by forbidden regions (if $|F(\varepsilon, w)| > 1$). The function $F(\varepsilon, w)$ is defined by

$$F(\varepsilon, w) = cos(A\varepsilon w)cos(Bsw) - \frac{\varepsilon}{s} sin(A\varepsilon w)sin(Bsw)$$

for $\varepsilon > 1$ and

$$F(\varepsilon, w) = cos(A\varepsilon w)cosh(Bsw) - \frac{\varepsilon}{s} sin(A\varepsilon w)sinh(Bsw) \tag{1.44}$$

for $0 < \varepsilon < 1$,
where $E = \Delta_0\varepsilon$ is the energy, $s = \sqrt{\varepsilon^2 - 1}$ or $\sqrt{1 - \varepsilon^2}$ for $\varepsilon > 1$ and $\varepsilon < 1$ respectively, $A = a/\pi\xi_0$, $B = b/\pi\xi_0$ (coherence length $\xi_0 = \hbar v_F/\pi\Delta_0$) and w is given[2] by $w^{-1} = cos\theta = [1 - k_\rho^2/k_F^2]^{1/2}$. In figure 1.5 appears $d\,arcos[F(\varepsilon, w)]/d\varepsilon$ for $A = B = 3$ and $w = 1$. This quantity is proportional to the density of states. The density of states spectrum exhibits energy bands separated by forbidden regions, the number of bands and their separation depend on A and B values. It is important to remark the appearance of a band below Δ. A refinement of this model was done by A. Hahn [26], he considered all components of the momentum parallel to the SN interface doing an integration over w, that means over θ

$$n(\varepsilon) = \frac{1}{A + B} \int_1^\infty \frac{\partial \mathrm{arccos} F(\varepsilon, w)}{\partial \varepsilon} \frac{dw}{w^3}. \tag{1.45}$$

[2] In the simplest Gelder's model $w = 1$.

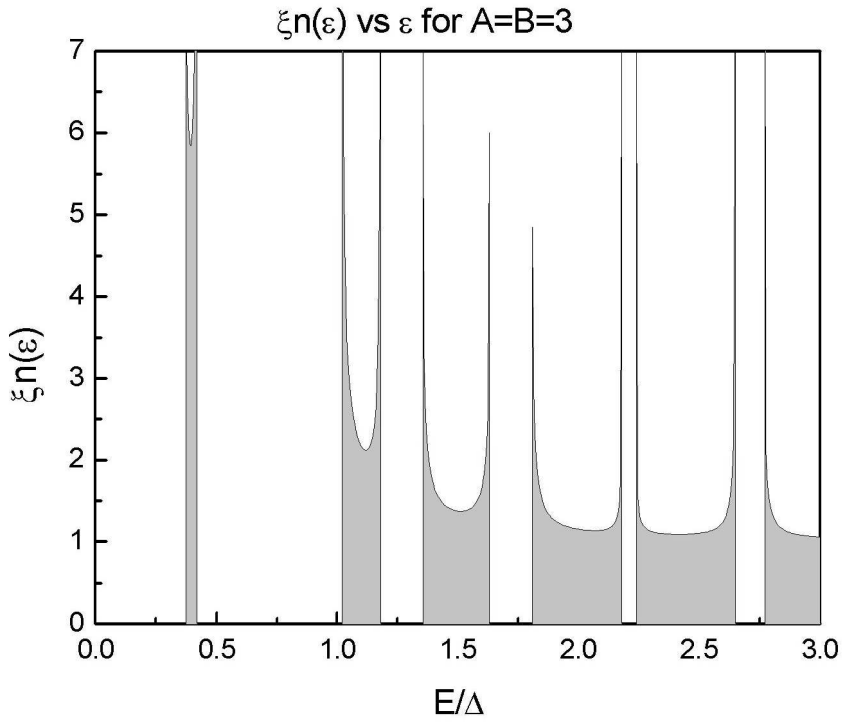

Figure 1.5: Calculated density of states spectrum for a 1–D superlattice using Eq.(1.43) for the parameters $A = B = 3$ and $w = 1$. Due to the periodicity energy band structures appear which are separated by forbidden regions.

This expression corresponds to a 3–D density of states for a one–dimensional superlattice. The energy bands overlap with each other so that the forbidden regions disappear and the band singularities are nearly periodic with A and B. Improvements of the one dimensional model were done by many authors, for instance Kümmel *et al.* [27, 28] used a self consistent pair potential in their calculation. However, the results concerning the density of states are similar to the square-well representation (Fig. 1.6). Other authors e.g. Shafranjuk *et al.* [29] went beyond the quasiclassical approximation i.e., they considered a superconducting coherence length comparable to the unit cell $\xi_\perp \approx c_\perp$ which is close to the actual situation in HTSC's. Furthermore, they considered a harmonic geometry for the superconducting order parameter and solved it self–consistently

$$\Delta(\theta, \phi, z) = \sum_{m=0}^{M} \Delta_m(\theta, \phi)\, cos(2Gmz) \tag{1.46}$$

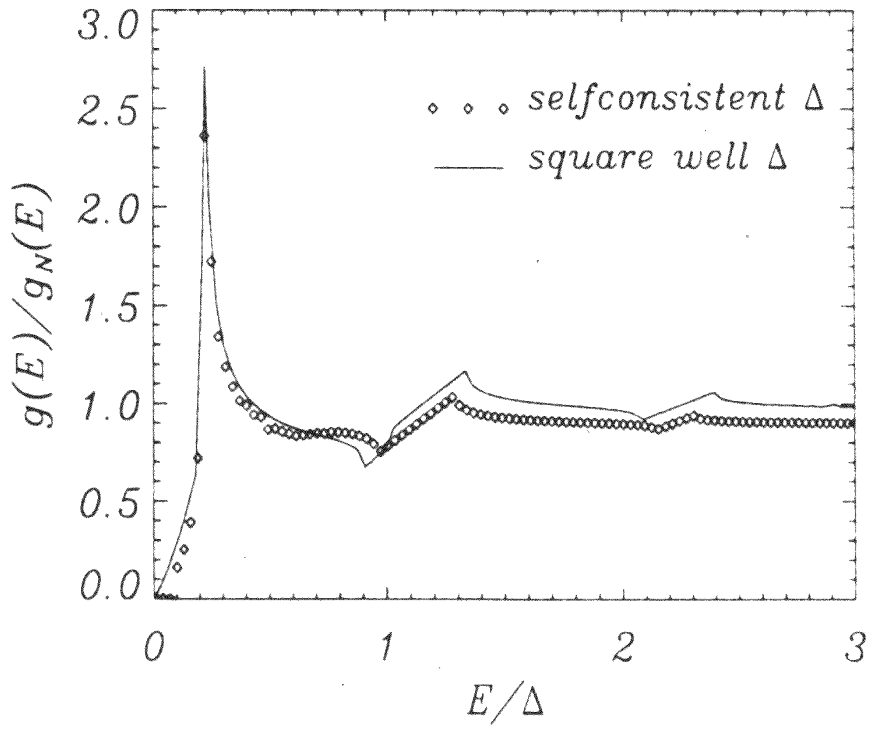

Figure 1.6: Calculation of the density of states using a self consistened pair potential. The result is compared with the 3–D density of states of the square well Δ. Taken from Ref. [28].

here M is a finite number, θ and ϕ are the angle of the electron momentum and $G = \pi/d$ is the reciprocal sublattice vector of the gap potential.

1.8 Comparison between pair potential models and experiments

The simplest examination for inhomogeneous superconductors is formed by normal and superconducting regions corresponding to a one dimensional Kronig–Penney model for the order parameter. A realistic approach was done by several authors by the assumption of other forms of the pair potential as illustrated previously. The first application of such a model considered basically the intermediate state of type–II superconductors were the vortexes constitute the normal regions embedded in a superconducting medium. With the discovery of

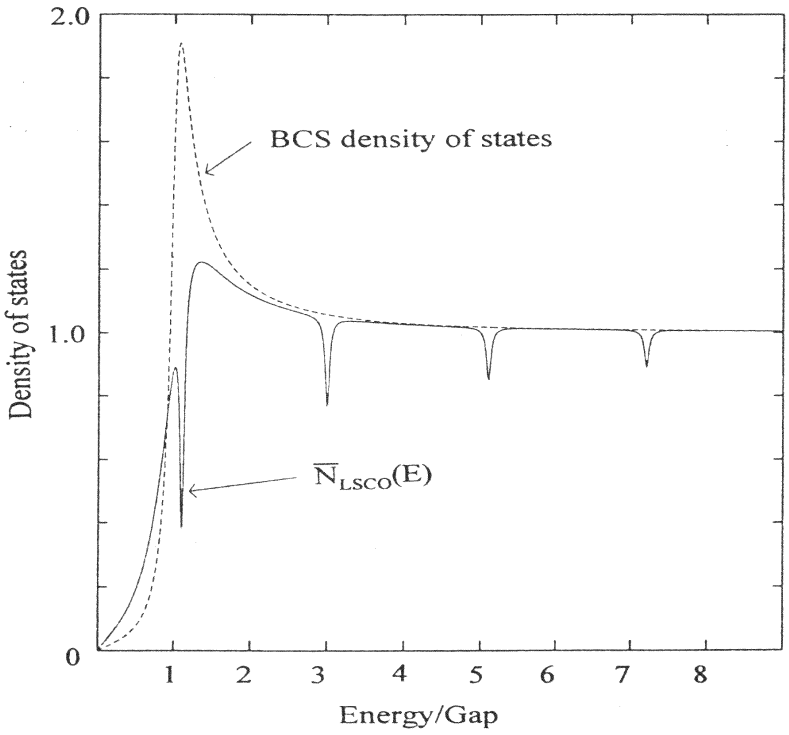

Figure 1.7: BCS density of states and the density of states in the c–direction of $La_{1-x}Sr_xCO_4$ calculated with an oscillating gap potential (Eq. 1.46). From Ref. [29].

the HTSCs, superlattices fabricated from different cuprates have received great attention because they constitute an appropriate scenario to understand their layered structure. The above mentioned theoretical models have been applied not only to low– but also to high temperature superconductor heterostructures. Anomalies in the tunneling spectra were observed in the gap structures of Pb–I–$La_{1-x}Sr_xCuO_4$ (where LSCO is a single crystal) junctions [30]. The calculation of the electron density of states with the superconducting order parameter (1.46) was used to explain the subgap structure of the tunneling spectrum (see Fig. 1.7). Other experiments on mesoscopics systems showed similar features, for instance Baturina *et al.* [31] fabricated chains of *SNS* junctions of superconducting polycrystalline PtSi films, where the N part was made as constriction of the same S material. Dips in the differential resistance were observed not only for $eV > \Delta$ but also in the subgap region at the voltage $V_n = 2\Delta/ne\,(n = 1, 2, \cdots)$. The appearance of the subharmonic gap structures was attributed to multiple Andreev reflections [32, 33].

Features in the c–axis tunneling differential conductance of $YBa_2Cu_3O_{7-x}$ / $PrBa_2Cu_3O_{7-y}$ superlattices at high voltage were also observed by Schattke [11, 34]. This features were explained very well with the Kronig–Penney model of the order parameter and were related with the superlattice modulation. At low voltage, a well–defined gap was detected that corresponded to the addition of the individual gap of each junction.

Chapter 2

Preparation and characterization

The relevant aspects of the preparation and the structural characterization of high temperature superconducting $YBa_2Cu_3O_{7-x}/PrBa_2Cu_3O_{7-y}$ ($PrBa_2Cu_{2.9}Ga_{0.1}O_{7-y}$) superlattices and trilayers will be described in this chapter. Since the patterning process into mesa structures is an essential part of the sample preparation, it will be presented in detail. This chapter ends with a description of the method for measuring the differential conductance.

2.1 Preparation of HTSC superlattices

Thin films based on high temperature superconductors have been produced by many methods of thin film technology. These methods may be classified into two big groups, the chemical vapor deposition (CVD) and the physical vapor deposition (PVD). The first group collects an amount of techniques in which basically the deposited phase is produced *in situ* via chemical reaction from gaseous precursors. Variants of this group are plasma assisted chemical vapor deposition (PACVD), metalorganic chemical vapor deposition (MOCVD) etc. [35]. To the second group belong all techniques which are characterized by the atom by atom transfer from the solid phase to the vapor phase and back to the solid phase, where a gradually building of a thin film on a surface to be coated takes place [36]. The latter group comprises from the vacuum evaporations methods like: thermal evaporation, molecular beam epitaxy (MBE), electron beam evaporation etc. to sputtering technologies and physical laser evaporations (laser ablation). In the following, a description of the sputtering technique used in this work is given.

Sputtering

This method is perhaps the best known and most widely used for preparing HTSC thin films. The main aspect of this technique is the plasma discharge of an inert gas between a grounded anode (where the substrate is placed) and a cathode with a negative potential (target), that is biased under a d.c. voltage between 0.2 kV and 2.0 kV. The physical principle is as follows: the ions and the electrons created at the breakdown upon voltage application produce more ions by collision with the gas atoms. Once the ions reach the edge of the cathode dark space, they are rapidly accelerated toward the target producing the sputtered species as well as secondary electrons, which are essential for sustaining the glow. As result of their impinging, target atoms are ejected out in random directions, some of them can reach the substrate where they diffuse and depending on growth rate and sputtering time one can grow a film with a desired thickness [37].

The quality of the HTSC films is very sensitive to the plasma conditions during deposition, when energetic particles of the plasma reach the substrate, they can deteriorate the growing film, therefore variants of the method have been employed to avoid this problem like "off–axis" sputtering, R. F. sputtering (radio frequency), with or without magnetic field etc. [35, 36]. Because the superconducting properties of the HTSC like critical temperature, critical current density etc. are very sensitive to the oxygen content, it is common to use as gas atmosphere of argon mixed with oxygen as a reactive component [38]. In this work, epitaxial high quality HTSC superlattices were prepared in a multicathode sputtering chamber constructed by G. Jakob [39]. The chamber offers the possibility to use up to four different targets. The substrate holder was controlled by a step motor and computer. For the purpose of this work, gold, $YBa_2Cu_3O_{7-x}$, $PrBa_2Cu_3O_{7-y}$and $PrBa_2Cu_{2.9}Ga_{0.1}O_{7-y}$targets were used. The *RE*–$Ba_2Cu_3O_{7-x}$ (RE=rare earth) targets were sintered according to the standard solid state reaction procedure [40, 41].

Pressure

During the film deposition, the chamber was operated in a sputtering atmosphere of a mixture of argon and oxygen. The presence of oxygen in the plasma can increase the O_2 content in the growing film, however, it can also influence the film morphology. A systematic study of the dependence of the surface morphology on the oxygen partial pressure was done by A. Schattke [11]. He showed that the

higher the oxygen content the more "holes" in the surface appear. The homogeneity of the surface is very important for the fabrication of c–axis superlattices because pinholes, impurities etc. can alter considerably the perpendicular transport in the devices creating shortcuts or shunt resistances. The optimal results obtained by Schattke were in a mixture of argon and oxygen in relation 2:1 at 3 mbar[1], this relation and pressure were used for the fabrication of multilayers in this work.

Substrates

The substrates used in this work were $SrTiO_3$ (001)–oriented single crystals. Before the deposition of the thin films was started, the substrates were subjected *in situ* to a thermal treatment at 900°C in a flow of oxygen. At such conditions the surface atoms rearrange in order to reduce the surface free energy [42]. In other words, a regrowth of the substrate surface should take place resulting in flat terraces (Fig. 2.1). Despite the high surface quality of the substrates, there is always some misorientation angle or miscut less than a few tenths of degree so that the cross–section of the substrate looks like a staircase. Because the substrate step height is about a third of the $YBa_2Cu_3O_{7-x}$ c–axis, anti–phase boundaries will form as the film grows [43]. Other problem that contributes to the formation of defects is related to the $YBa_2Cu_3O_{7-x}$ growth mechanism. The surface morphology of both laser–ablated and sputtered $YBa_2Cu_3O_{7-x}$ films reveals pronounced spiral-shaped terraces, which can indicate screw dislocations with a density up to approx. 10^9 cm^{-2} [44]. The origin of such a growth spiral has been attributed for example to defects in substrate, incoherent coalescence of two or more growth islands etc. [45, 46]. In order to reduce substrate induced strain on the film, an initial layer of 50 nm $YBa_2Cu_3O_{7-x}$ was grown. The substrate temperature during the deposition was chosen between 760°C and 840°C, this ensured that the growth was c–axis oriented[2]. Afterward, $YBa_2Cu_3O_{7-x}$ and $PrBa_2Cu_3O_{7-y}$ layers were alternately deposited up to a total superlattice thickness of about 300 nm. Thereafter, a post–annealing step was carried out at 550°C in an oxygen pres-

[1] A problem during the sputtering process in the planar configuration is that the ionization of O_2^{-1} and O^{-1} causes back–sputtering of the film from the substrate. A possibility to avoid this problem is using higher pressures so that the mean free path of the negative ions is reduced considerably.

[2] If the substrate temperature is lower than approx. 670°C, a–axis is the preferred growth orientation [47].

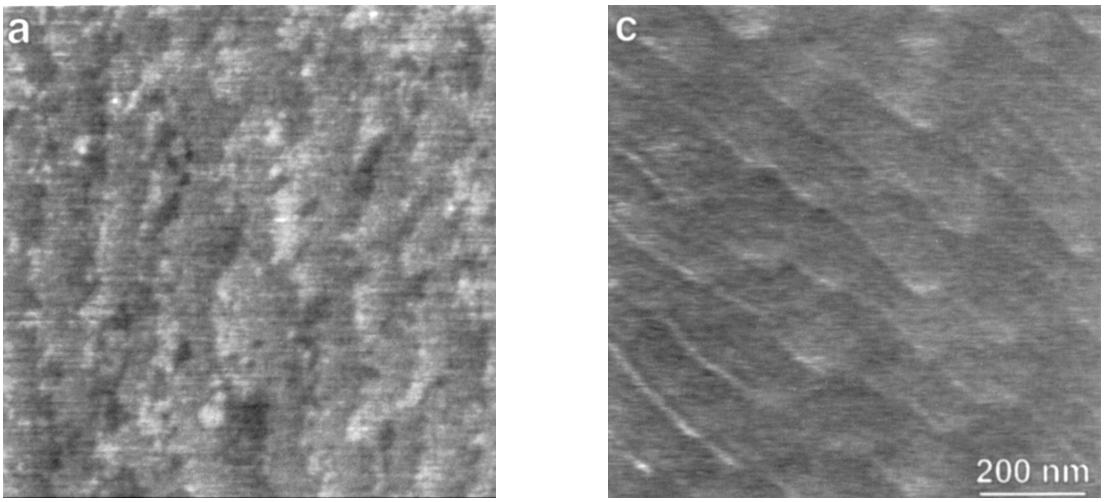

Figure 2.1: AFM picture of a $SrTiO_3$ substrate without (left) and with thermal treatment for 30 min in oxygen (right) at 900°C. A re–growth on the surface took place. Taken from Ref. [42].

sure of 0.9 bar to adjust the optimal oxygen content. The layer thicknesses were controlled by the sputtering time and checked later with X–ray diffraction at low angles. More details will be described in a later section.

Counter electrode

After the preparation of the superlattices and without opening the chamber, the oxygen atmosphere was pumped out, thereafter, the chamber was filled with argon up to the pressure of 0.30 mbar and a gold layer of approx. 100 nm was deposited *in situ* at room temperature using d.c. magnetron sputtering. This layer serves not only to avoid degradation of the surface but also as upper electric contact with low resistivity [48].

2.2 Characterization

2.2.1 Magnetic susceptibility

A method used for rapid characterization of the critical temperature and superconducting volume fraction constitutes the AC magnetic susceptibility. The real part of the susceptibility χ' shows for a $YBa_2Cu_3O_{7-x}$ sample a transition temperature of around 90 K with a transition width of approx. 0.5 K. The imaginary

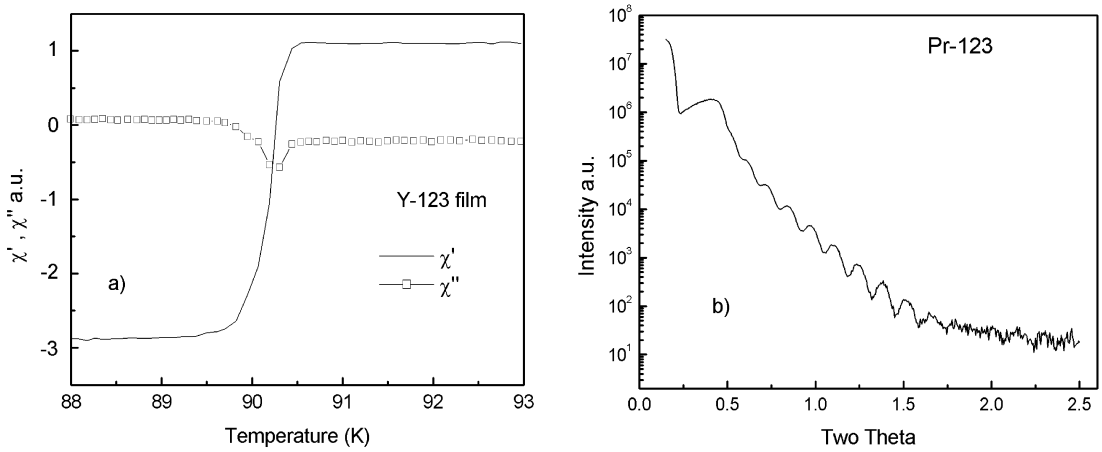

Figure 2.2: Real and imaginary parts of the magnetic susceptibility of a $YBa_2Cu_3O_{7-x}$ sample (a). Low angle X–ray diffractogram of a $PrBa_2Cu_3O_{7-y}$ film. From the distance between two consecutive maxima, the film thickness was calculated (b).

part χ'' is related to losses (Fig. 2.2a).

2.2.2 X–ray diffraction

The orientation of the thin films was analyzed by means of X–ray diffractometry (XRD) in Bragg–Brentano geometry [49]. $PrBa_2Cu_3O_{7-y}$ and $YBa_2Cu_3O_{7-x}$ samples showed c–axis orientation i.e., the (00ℓ) peaks were dominant, additionally the Full Width at Half Maximum (FWHM) of the rocking curve of the (005) peak was $\Delta\omega \leq 0.4°$ indicating a good epitaxy.

The combination of m ($YBa_2Cu_3O_{7-x}$) and n ($PrBa_2Cu_3O_{7-y}$) unit cells defines a new "supercell" with a large "c" axis[3] and consequently a small reciprocal lattice vector [39, 51]. For this reason, the diffractograms of superlattices exhibit additional reflections (satellites lines) compared to the pure RE–$Ba_2Cu_3O_{7-x}$ thin film. The value of the rocking curve of the (005) peak of the superlattices was about $\Delta\omega \approx 0.5°$, which is slightly larger than in the single films because of the lattice parameter difference of both material[4].

[3]Where "c" $= n_Y c_Y + m_{Pr} c_{Pr}$. n_Y, m_{Pr} are the number of unit cells in the individual $YBa_2Cu_3O_{7-x}$ and $PrBa_2Cu_3O_{7-y}$ layers respectively and c_Y, c_{Pr} the corresponding c–axis lattice parameters.

[4]The lattice parameter for $PrBa_2Cu_3O_{7-y}$ are $a = b = 3.905$ Å, $c = 11.660$ Å while for $YBa_2Cu_3O_{7-x}$ are $a = 3.827$ Å, $b = 3.877$ Å and $c = 11.708$ Å i.e., a maximal difference of 2% [50].

The intensity and sharpness of these satellites peaks indicates the crystalline quality of the superlattices. Additionally, from their position it is possible to calculate the thicknesses of an individual bilayer. With the angular position of two consecutive satellites Θ_i, Θ_{i+1}, the X–ray wavelength λ and using the equation $\Lambda = \lambda/(2(sin\Theta_i - sin\Theta_{i+1}))$, the modulation length was determined ($\Lambda = (n+m)\bar{c}$ where $\bar{c}$ is the average). Moreover, the modulation length is given by $\Lambda = r_Y t_Y + r_{Pr} t_{Pr}$ where r and t are the deposition rate and deposition time of $YBa_2Cu_3O_{7-x}$ and $PrBa_2Cu_3O_{7-y}$ respectively, therefore one can determine and optimize the exact deposition time for growing a single cell of each material.

Additionally, the diffractograms were analyzed and simulated employing the SUPREX program, this program was developed by E. E. Fullerton *et al.* [52] to model the X–ray diffraction profiles from superlattices. The structural refine-

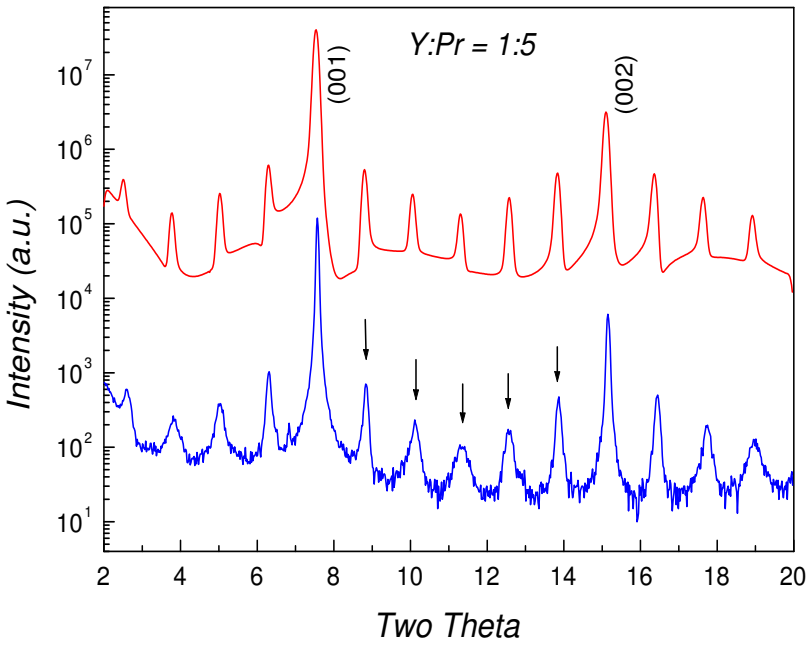

Figure 2.3: X–ray diffraction of the sample $[(YBa_2Cu_3O_{7-x})_1/(PrBa_2Cu_3O_{7-y})_5]_{\times 30}$ together with its simulation. The arrows denote the appearance of satellites as a result of the additional periodicity. The agreement between the simulation and the experimental spectrum denotes the quality of the sample. (The simulated curve is shifted up for clarity.)

ment includes several parameters related to layer thickness fluctuations, interface disorder, interdiffusion etc. that are present in actual superlattices. In Fig. 2.3 an X–ray diffractogram of a $(YBa_2Cu_3O_{7-x})_1/(PrBa_2Cu_3O_{7-y})_5$ superlattice is shown together with its simulation. The arrows indicate the appearance of five satellites additional to the main peaks (001) and (002) of a $YBa_2Cu_3O_{7-x}$ thin film. The good agreement between the measured spectrum and the simulation reveals a high crystalline quality of the sample. The simulation parameter used to obtain the upper diffractogram were: an average interface roughnesses of about 0.2 Å, an interdiffusion of about 5% and a step disorder between 5% and 10%. These values denote a high interface quality.

2.3 Junction patterning

One of the purposes of the thin film preparation based on HTSC materials is not only the study of their physical properties but also the fabrication of electronic devices based on thin films. Of great importance is the goal of making the devices as small as possible, especially if one deals with microelectronic applications. In order to achieve patterning dimensions in the range between submillimeter to a few micrometers, photolithographic procedures have been employed.

The main stages [53] are: firstly the film to be patterned is covered with a layer of radiation–sensitive photoresist, typically with a thicknesses of about 1 μm [5]. Once the resist is baked, an exposition to UV light through a mask is performed using a mercury discharge lamp. By using positive or negative resist, either the regions exposed to the light or those not exposed will be washed out with a suitable developer. After the development, some areas on the film are not longer covered with resist. At this point one can perform either chemical or ion beam etching to remove the unprotected areas. Finally the residual photoresist is removed by a proper solvent remaining only the desired structure.

Another procedure which leads to similar structures without etching directly the material in matter is the so–called Lift–off technique. The substrate is coated with the photoresist. Using the same procedure as mentioned previously, the resist is shaped into the desired structure but negative. The material is then deposited. Finally, the developer removes the resist under the film together with the film so that the desired patterned film in contact with the substrate remains.

[5] The thickness of the resist depends on the viscosity, angular velocity and time of spinning.

Since the interest of this work is the study of the perpendicular transport properties of $(YBa_2Cu_3O_{7-x})_n/(PrBa_2Cu_3O_{7-y})_m$ heterostructures, it is necessary to pattern the samples into a special shape, the so–called mesa structures so that the current is constrained to flow perpendicular to the surface and through the interface of the superlattice. Usually mesas are located on a substrate of the same material, a possibility for their fabrication is the combination of the standard patterning method and ion milling technique. The procedure used in the present work is based on the one utilized previously by A. Schattke [11] and M. Engelmann [54]. Details will be outlined in the following.

2.3.1 Mesa structures

The mesa structures used in this work were fabricated using a combination of wet and dry etching techniques in several steps. Firstly, a ground electrode of 10 mm×1 mm was patterned[6] as described in the last paragraph, thereafter eight squares of sizes between 16×16 $(\mu m)^2$ and 50×50 $(\mu m)^2$ were patterned by photolithography close to the longitudinal edges of the ground electrode. The eight photoresist squares will protect small areas where the mesas will be fabricated. Subsequently, the sample was subjected to ion beam etching where the unprotected part was removed by ion milling until a depth of about 150 nm was reached (see Figs. 2.4, 2.5)[7], subsequently the photoresist was removed with acetone and plasma etching that can guarantee a clean surface on the top of the mesa. The patterned sample was coated again with a negative photoresist ma–N 415 which will be also used as an insulator around each mesa. A small window has to be opened on the top of each mesa. In order to avoid short circuit due to mismatch of the alignment, the window areas should be smaller than the mesa area. A mask with four 10×10 $(\mu m)^2$ and four 16×16 $(\mu m)^2$ squares was used for this purpose, additionally a mask aligner that allows to position the mask onto the mesas with an accuracy of about 2 μm was built.

In order to wire the mesa, a window on the top of each mesa was opened by photolithography. This process was very delicate because inside the window must be free of photoresist residues (Fig. 2.6). The photoresist outside the

[6]All steps described hereafter were done in a class 100 clean room.

[7]A test sample of 150 nm thick (plus a gold layer) were placed besides the main sample, when the test sample is completely removed the process is stopped. In order to avoid oxygen loss due to the extreme conditions of low pressure and local overheating during the etch process, the sample holder was put in thermal contact with a liquid nitrogen flow.

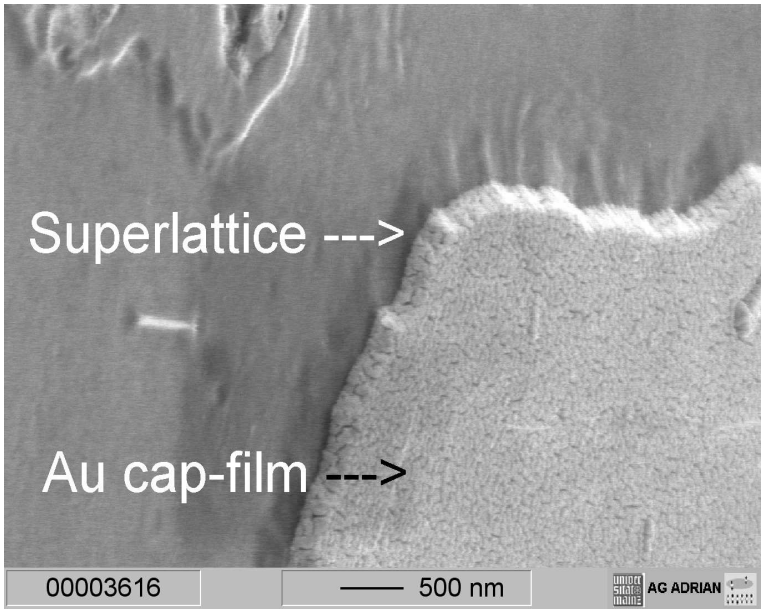

Figure 2.4: SEM picture of a mesa from the side. During the ion milling process a lateral damage on the mesa takes place.

window served as insulating layer, because it can be handled like a polyimide [53] a postexposure for an hour under UV radiation followed by a hard–bake at 180°C was performed. After that, the resist became mechanically more stable and acetone resistant, additionally the hard–baking improves its adhesion to the film and causes some resist flow, which can fill up pinholes reducing the probability of short circuits.

2.3.2 Wiring the junction

Finally, a second gold layer of about 900 nm thickness was sputtered in order to wire the mesa. This gold layer was patterned via standard lithography into contact leads, the areas that were not covered with photoresist were removed with an aqueous solution of potassium iodide (KI) and iodide (I) (Fig. 2.7). An advantage of this wet chemical etching is its compatibility with the HTSC $YBa_2Cu_3O_{7-x}$ because neither the $YBa_2Cu_3O_{7-x}$ film nor the $SrTiO_3$ substrate are attacked [48].

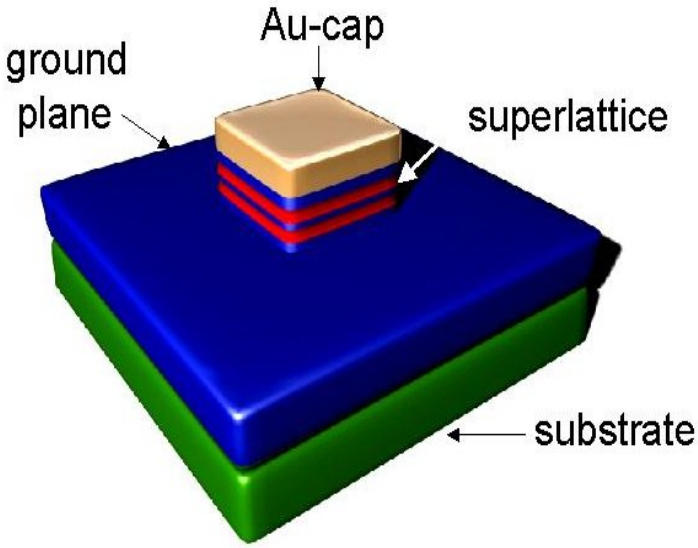

Figure 2.5: Using ion milling mesas between 16 μm and 50 μm lateral size were prepared. The sketch represents a 150 nm ground electrode, a mesa with 150 nm height and a gold contact on the top.

2.3.3 Process outline

The mesa fabrication process is summarized in Fig. 2.8. A positive photoresist will protect small areas between $(16\,\mu\text{m})^2$ and $(50\,\mu\text{m})^2$ (Fig. 2.8a). Using argon ion milling, the unprotected areas are etched until a depth of about 150 nm (Fig. 2.8b), thereafter, the whole surface is coated with a negative photoresist, in which the mesas are embedded in this photoresist. (Fig. 2.8c). Using photolithograpic patterning again a window with an area smaller than the mesas's area is opened (Fig. 2.8d). This step is very delicate because first: a mismatch in the alignment between window and mesa can lead to short circuits between the base electrode and the contact leads and second the mesa must be free of photoresist rest. Afterwards the photoresist is hardened in U.V. light and at 180°C and becomes mechanically stable. Subsequently the sample is transfered carefully from the clean room in an exsiccator to minimize the contact with air and dust particles and put into a sputtering chamber where a 900 nm thick gold layer is deposited (Fig. 2.8e). Finally the gold layer is patterned photolithographically into contact lead and the device is contacted with Au bonding pads (Fig. 2.8f).

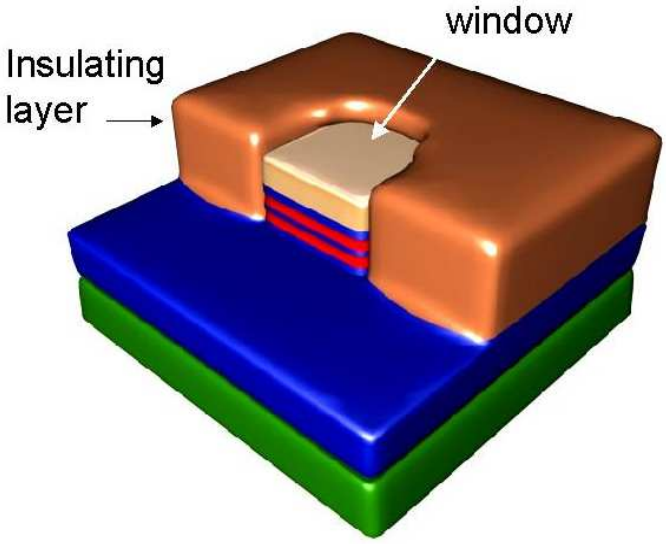

Figure 2.6: A photolithographic process allows to open a window on the top of the mesa, so that it later can be wired. The negative photoresist was used as an insulator.

2.4 Device design

The whole device consist of three different parts: a $YBa_2Cu_3O_{7-x}$ base electrode followed by a small size heterostructure mesa (superlattice or trilayer) embedded in an insulator (hardened photoresist) and gold leads on the top. Figure 2.9 shows the chip layout, where the base electrode is represented by a shadowed rectangle, eight mesas are located over the electrode together with a pair of pads on the ends of the base electrode, just above each mesa there is a gold strip. The out–of–plane transport properties are measured as sketched in Fig. 2.9. Unfortunately a true four point measurement was not possible because due to the small window size the current and voltage pads on the mesa could not be separated. A splitting into two pads is very difficult due to the resolution limitations of the photolithographic patterning (down to approx. 5 μm). All measurements were carried out in this geometry where the contact resistance on the top of the mesa is included. In our samples this resistance has values between $0.5\times 10^{-4}\,\Omega\,\mathrm{cm}^2$ and $2\times 10^{-4}\,\Omega\,\mathrm{cm}^2$. The in–plane transport properties of the ground layers were measured using the four pads at the ends of the base electrode.

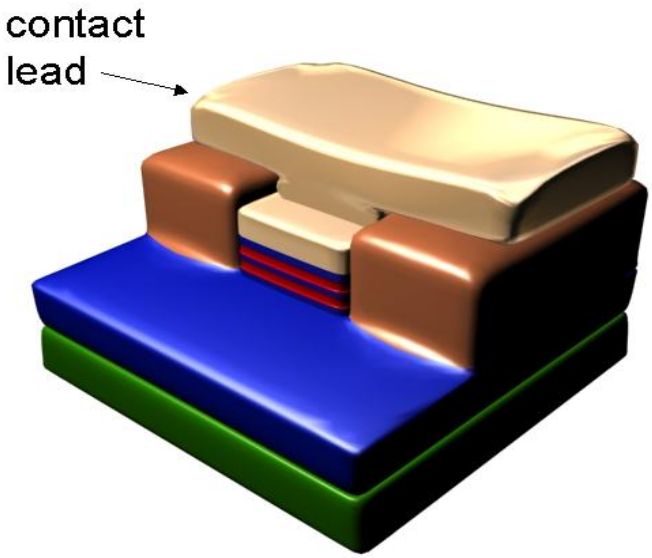

Figure 2.7: A gold layer of about 900 nm thickness was sputtered to wire the mesa and thereafter patterned via photolithography into contact leads.

2.5 Differential conductance measurements

The method used in this work to measure the differential conductivity is based on the conventional lock–in technique proposed by Adler and Jackson [55]. This was previously used in tunneling spectroscopy of HTSC and Heavy Fermion systems by e.g. Becherer [56] and Jourdan [57] respectively.

In the voltage driven setup a superposition of a small modulation voltage ($V_{ac} \approx 100\mu$V that is smaller than Δ_c/e) and a bias voltage is applied to the junction. The current through the junction can be expanded in a Taylor series

$$I(V_0 + \delta V\, cos(\omega t)) = I(V_0) + \left.\frac{dI}{dV}\right|_{V_0} \delta V(\omega)\, cos(\omega t) + \cdots, \tag{2.1}$$

where $I(V_0)$ is proportional to the direct current through the junction and $G(V_0) = dI/dV$ is the differential conductance. If the applied current is modulated (so–called current driven setup), the terms of the Taylor series correspond to the dropped voltage on the junction ($V(I_0)$) and the differential resistance (dV/dI). The expression for the voltage is given by

$$V(I_0 + \delta I\, cos(\omega t)) = V(I_0) + \left.\frac{dV}{dI}\right|_{I_0} \delta I(\omega)\, cos(\omega t) + \cdots. \tag{2.2}$$

In the present work, both setups were used.

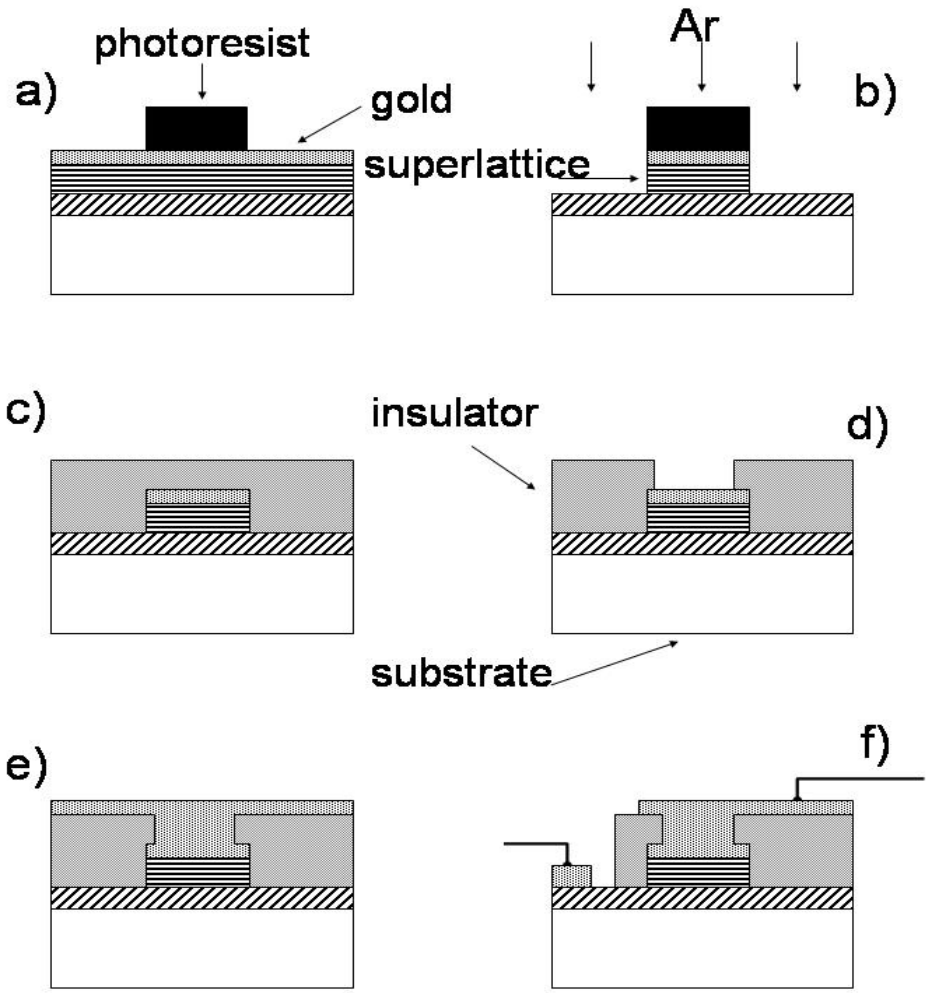

Figure 2.8: Fabrication process of mesa structures using photolithography and argon ion milling.

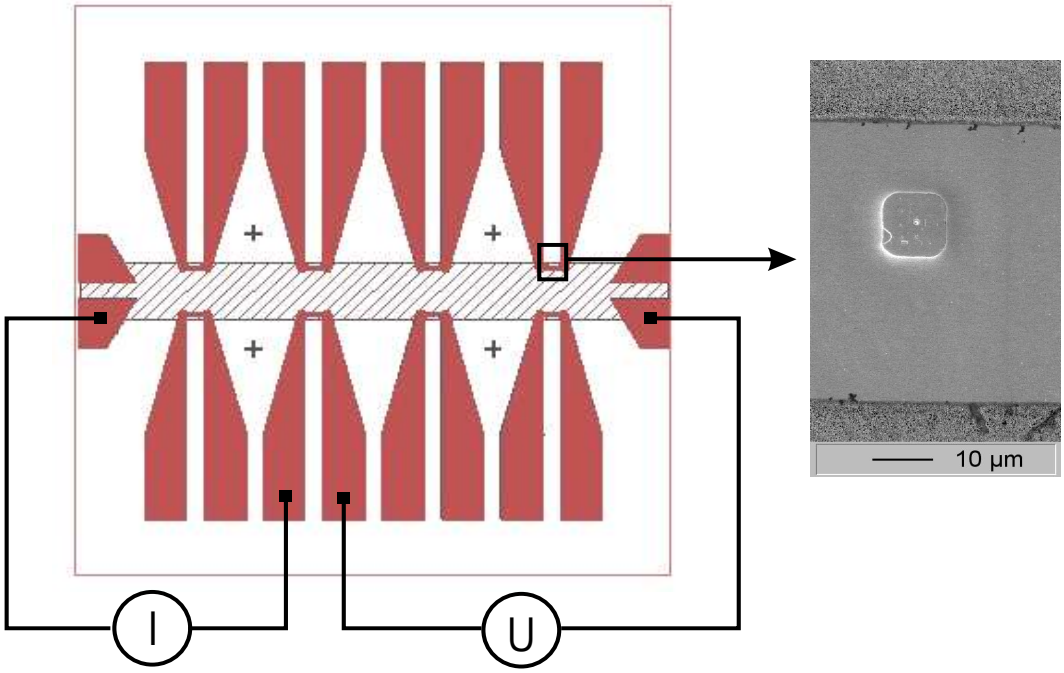

Figure 2.9: Top view of the chip. The striped rectangle represents the ground electrode, each mesa was contacted with a gold strip. The out–of–plane electrical measurement was performed between the pads (on the base) and the gold strip, whereas the in–plane transport properties was measured in the four terminal at the farther place of the basis electrode (left). The detail shows a SEM picture of a mesa structure contacted with gold strip (right).

Chapter 3

Trilayers

This chapter is intented to study the transport properties perpendicular to the plane of $YBa_2Cu_3O_{7-x}/PrBa_2Cu_{2.9}Ga_{0.1}O_{7-y}/YBa_2Cu_3O_{7-x}$trilayer heterostructures which were prepared at different substrate temperature. This system was chosen in order to understand the transport properties in more complex system like superlattices. The differential conductance–voltage characteristics were analyzed with in the BTK theory of superconductor–normal metal interfaces and the Anderson–Appelbaum model. Additionally a discussion of the proximity effect of superconductor–normal metal *S/N* interfaces is presented for a better understanding of the transport phenomena in our HTSC's heterostructures.

3.1 Bonder–Tinkham–Klapwijk model

The problem of the *NS* interface was mentioned in chapter one. It was seen that, if a good contact between the metal and the superconductor exists, two situations can occur. If the energy of the incident normal electrons is larger than the gap energy, they pass through the interface as normal quasiparticles, but on the contrary, if their energy is less than the energy gap, the following situation will happen. Once the incoming electrons reach the interface they cannot enter as a quasiparticle because there are no available states in the gap. As a result, electrons are retro–reflected into the normal metal as holes and twice the charge is transferred into the superconductor by the formation of a Cooper pair. This situation is valid only if there is no barrier at the interface. Blonder, Tinkham and Klapwijk [23] developed a theory (BTK), which is a generalization of the Andreev reflection process. This theory includes a diversity of possibilities between

no–barrier to a strong tunnel barrier. They consider a scattering potential at the interface of the form $U(x) = H\delta(x)$. The barrier is characterized with the dimensionless parameter $Z = H/\hbar v_F$ that denotes the strength of the barrier. $Z = 0$ corresponds to an ideal point contact whereas $Z \to \infty$ indicates an ideal tunnel contact. Moreover the parameter Z is related to the transmission coefficient T_0 in the form $T_0 = 1/(1 + Z^2)$ and to the reflection coefficient $R = Z^2/(1 + Z^2)$. The normal state conductance is given by

$$G_N = \frac{2e^2}{h}\frac{1}{1+Z^2}. \tag{3.1}$$

Figure 3.1 shows how the differential conductance vs. voltage characteristic de-

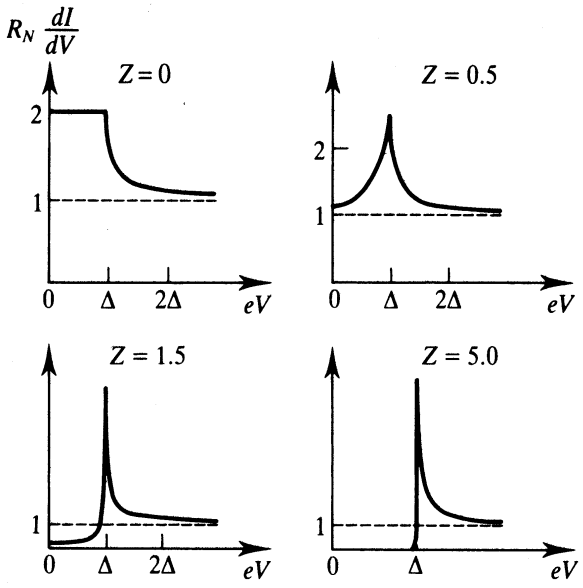

Figure 3.1: Differential conductance vs. voltage after the BTK model [23] for various barrier strengths Z at T = 0 K.

pends on the barrier strength, starting from the pure Andreev case, where the conductance at low voltage is twice the normal conductance ($Z = 0$), to the classic tunnel characteristic of a *SIN* junction (high Z). At high voltages the differential resistance (dV/dI) drops off for all cases to the normal resistance R_N.

3.2 Properties of the barrier

Since the first report on the possibility to fabricate heterostructures based on $YBa_2Cu_3O_{7-x}$ and $PrBa_2Cu_3O_{7-y}$ materials [58] not only insulating but also metallic barriers, such a $La_{1.4}Sr_{0.6}CuO_4$, Ruthanates etc. were used [59–62]. All these materials are promising candidates because their lattice constants and thermal expansion coefficients are similar to those of $YBa_2Cu_3O_{7-x}$. However, $PrBa_2Cu_3O_{7-y}$ is a special material, it is the only one of the *RE*–$Ba_2Cu_3O_7$ (RE=rare earth) family which does not exhibit superconductivity. $PrBa_2Cu_3O_{7-y}$ has a very low carrier density concentration and its temperature dependence of the electrical resistance shows a doped semiconductor behavior[1]. The linear variation of $\ln(\rho)$ vs. $T^{1/4}$ for $PrBa_2Cu_3O_{7-y}$ between 60 K and 200 K suggests a similar transport mechanism as observed in Mott insulators which obey the variable range hopping law (VRH)

$$\rho = \rho_0 exp(T_0/T)^{\alpha} \quad \text{where} \quad \alpha = \frac{1}{d+1}, \tag{3.2}$$

with $T_0 \sim 1/N(0)d^3$, where $N(0)$ is the density of states near the Fermi level and d the localization length.

Xu *et al.* [63] reported transport measurements of $PrBa_2Cu_{3-x}Ga_xO_{7-y}$ with x between 0 and 0.6. The partial substitution of Cu^{2+} by Ga^{3+} increases the resistivity by several orders of magnitude (Fig. 3.2). This fact offers the possibility to fabricate actual *SIS* junctions. Other substitutions of Cu by atoms of higher valence state, such a Zn and Co, proposed by Tipparach *et al.* [64] have a similar effect on the resistivity. The reason for the increase of the resistivity was attributed to localization of holes.

3.3 Results of trilayers prepared at $T_s = 840°C$

The first tunneling transport measurements performed on (Y/Pr)$Ba_2Cu_3O_7$ superlattices showed complex features that deviate from the expected superconductor–insulator–$\cdots$ ($S-I-S\cdots$) system. To illustrate this situation, Fig. 3.3 shows the differential conductance dependence on the bias voltage of a $50\,\mu m \times 50\,\mu m$ mesa of a $(YBa_2Cu_3O_{7-x})_2/(PrBa_2Cu_3O_{7-y})_{10}$ superlattice (sample $YBCO_2/PBCO_{10}$) at 54 K. The differential conductance shows a strong dependence on the bias volt-

[1]The electrical resistivity of $PrBa_2Cu_3O_{7-y}$ is about 10 Ω cm at T = 4 K.

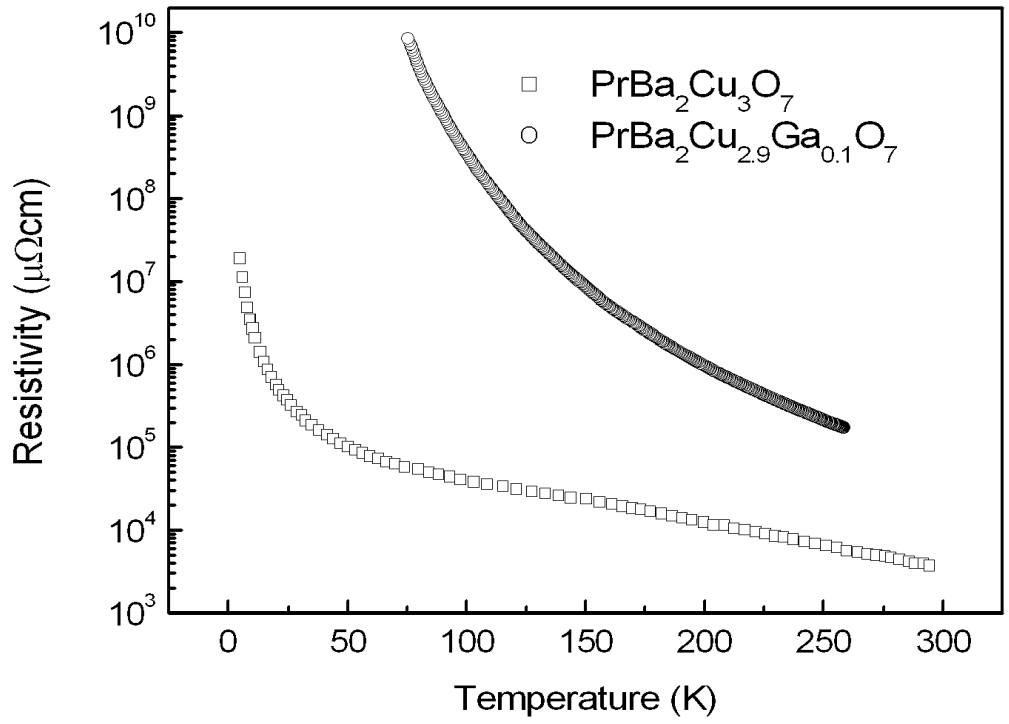

Figure 3.2: Temperature dependence of the resistivity of $PrBa_2Cu_3O_{7-y}$ (□) and $PrBa_2Cu_{2.9}Ga_{0.1}O_{7-y}$ (○) bulk samples.

age; at low bias the conductance is larger than the conductance in the normal state (this is typical for metallic junctions), whereas at high bias the differential conductance takes on negative values. The later phenomenon is due to overheating effects because of the large size of the mesa. This topic will be discussed in more detail in chapter four.

In order to understand the transport properties of a multi–junction system like a superlattice it is important to study first a more simple heterostructure like a trilayer. For this reason the rest of this chapter concentrates on the transport measurements on a single superconductor–insulator–superconductor system. In order to suppress the order parameter inside the barrier, $PrBa_2Cu_{2.9}Ga_{0.1}O_{7-y}$was employed instead of $PrBa_2Cu_3O_{7-y}$ as insulating barrier because of its excellent insulating characteristic. Additionally in order to reduce the overheating effects, the size of the mesas was reduced by a factor of six.

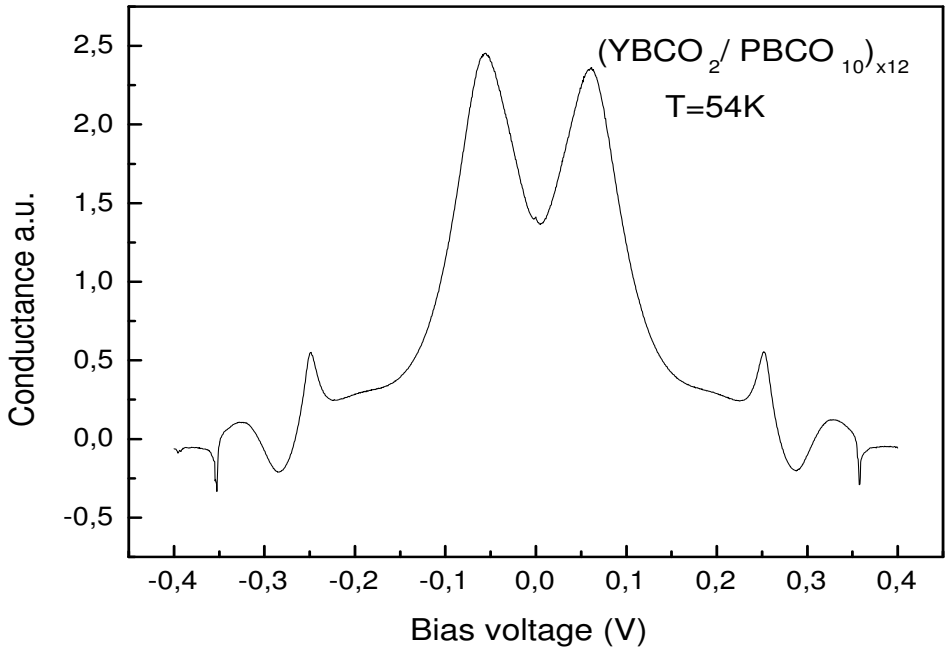

Figure 3.3: Differential conductance vs. voltage of a superlattice $[(YBa_2Cu_3O_{7-x})_2/(PrBa_2Cu_3O_{7-y})_{10}]_{12}$. The value of the conductivity in the subgap region is larger than the conductivity at the normal state. The shape of the *G(V)* dependence reveals a metallic junction behavior.

Differential conductance measurements

The present section presents results of tunnel differential conductance measurements of $YBa_2Cu_3O_{7-x}$ /$PrBa_2Cu_{2.9}Ga_{0.1}O_{7-y}$ /$YBa_2Cu_3O_{7-x}$ trilayers prepared as described in chapter two for a substrate temperature of 840°C. The thickness of the barrier was chosen between 20 nm and 25 nm (∼roughly 20 unit cells), while the thickness of the base electrode and the counterelectrode was 200 nm and 100 nm respectively.

Figure 3.4 shows the (dI/dV)–V dependence for different temperatures of a 20×20 μm^2 mesa of a trilayer with 20 nm barrier thickness (hereafter denoted as sample YBCO/PBCGO (20nm)/YBCO–HT). Two maxima at $|V| \approx 2$ mV are observed at T = 5 K. They represent the increase of the quasiparticle density of states at the $YBa_2Cu_3O_{7-x}$ gap. However, for $|V| < 2$ mV the differential conductance G has finite value which is larger than the conductance in the normal

state ($eV \gg \Delta$), suggesting the existence of states inside the gap region. As the temperature increases, the intensity of the maxima as well as their distance decreases while $G(0)$ remains almost unchanged. Above Δ, the $G(V)$ dependence is practically constant and does not depend on temperature.

The shape of the (dI/dV)–V curve of the sample $YBCO_2/PBCO_{10}$ in comparison with the curve of the sample YBCO/PBCGO (20nm)/YBCO–HT shows some similarities: the excess of differential conductance at zero bias and a nearly constant conductance background. The $G(V)$ curve of sample $YBCO_2/PBCO_{10}$ closely resembles the $G(V)$ curve of the sample YBCO/PBCGO (20nm)/YBCO–HT, but the former has more structure because it has multiple contacts in series (approx. 15 junctions). Despite the fact that a more insulating barrier was used, the $G(V)$ dependence of the sample YBCO/PBCGO (20nm)/YBCO–HT disagrees with a tunnel conductance curve of a superconductor–insulator– superconductor junction. Both $PrBa_2Cu_3O_{7-y}$ and $PrBa_2Cu_{2.9}Ga_{0.1}O_{7-y}$ barriers have

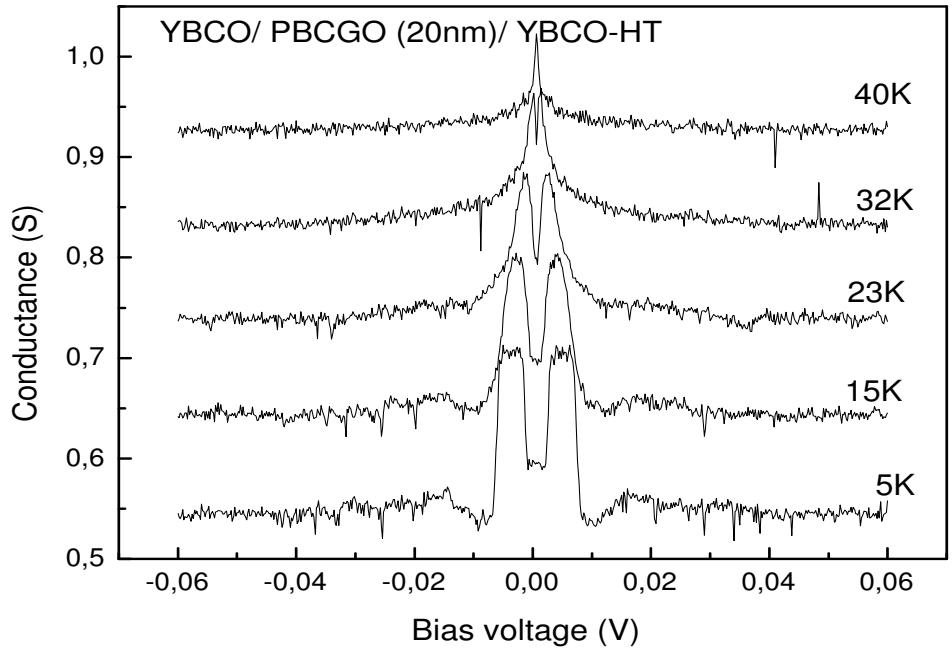

Figure 3.4: Differential conductance vs. voltage of a trilayer with 20 nm $PrBa_2Cu_{2.9}Ga_{0.1}O_{7-y}$ barrier for different temperatures. The curves are 0.1 S vertically shifted.

low carrier densities, in consequence the order parameter should be considerably diminished inside the barrier. One should expect that no–states should be available for quasiparticles in the subgap region, and the differential conductance should be substantially reduced.

The voltage–current characteristic of sample YBCO/PBCGO (20nm)/YBCO–HT at 3 K shows a slope change just at $eV = \Delta$. The shape of this V–I curve indicates a RCSJ–like behavior. However, a residual resistance remains because of the contact resistance. Since the measurements were performed in three–point geometry the contact resistance is part of the total resistance R. Figure 3.5 shows both, $V = IR$ (solid line) and $V = (R–R_c)I$ curves. For the latter one the contact resistance was subtracted. The calculated junction resistance for the sample YBCO/PBCGO (20nm)/YBCO–HT is $R_c = 0.8\,\Omega$ which results in $R_cA = 3.2 \times 10^{-6}\,\Omega\text{cm}^2$. The arrow on the figure indicates a change in the slope that corresponds to a critical current density of $J_c = 6.2 \times 10^2\text{A/cm}^2$ at 3 K. This value is consistent with previous result of $YBa_2Cu_3O_{7-x}$trilayers junctions [65,66]. However the magnetic field dependence of the critical current at 3 K did not show the behavior expected for a Josephson–like junction type.

Despite the nominally insulating barrier of the trilayer YBCO/PBCGO(20nm)/ YBCO–HT, the shape of the G–V suggests a *SNS* junction behavior. For some reason the barrier acquires a metallic character creating some conduction channels for $eV < \Delta$, this causes an increase of the differential conductance. Another aspect is the quality of the interface between $YBa_2Cu_3O_{7-x}$ and $PrBa_2Cu_{2.9}Ga_{0.1}O_{7-y}$. If some degradation takes place, an intermediate region can form that can be favorable to the penetration of the order parameter into the barrier. The barrier acquires a metallic behavior via proximity effect. A detailed discussion of the proximity effect will be presented in the next section.

Assuming that the sample YBCO/PBCGO (20nm)/YBCO–HT has a metallic barrier one can compare the experimental $G(V)$ curve with the BTK theory. Figure 3.6 shows the (dI/dV)–V curve at 3.5 K together with a simulation assuming the following fit parameters: a gap energy of 1.5 meV and a barrier strength of $Z = 0.45$. The deduced Δ is relatively small in comparison with the c–axis gap of $YBa_2Cu_3O_{7-x}$ [11, 61, 67], additionally the value of the Z parameter indicates a high barrier transparency T_0.

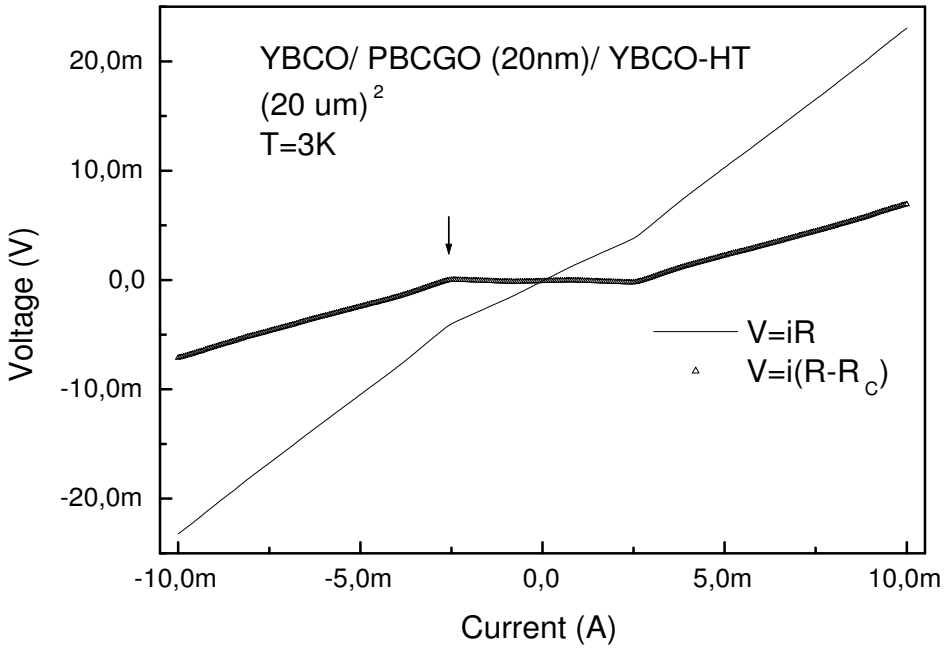

Figure 3.5: Voltage vs. current characteristic for a junction with 20 nm thick barrier. The arrow indicates the critical current for this junction. The solid line represents the measured V–I curve, and the triangles the V–I characteristic after subtracting the contact resistance.

3.4 Proximity effect

3.4.1 Conventional proximity effect

The proximity effect in SN junctions was first studied by de Gennes [68]. He stated that a normal metal in contact with a superconductor results in the reduction of the superconducting character of the S electrode close to the interface because of the presence of a normal conductor (N). The superconductivity on the other hand extends over the interface into the normal metal for a short distance i.e., the order parameter decays exponentially in the metal over a distance called decay length (Fig. 3.7)

$$\xi_n = \left(\frac{\hbar}{2\pi k_B T}\right) v_n, \tag{3.3}$$

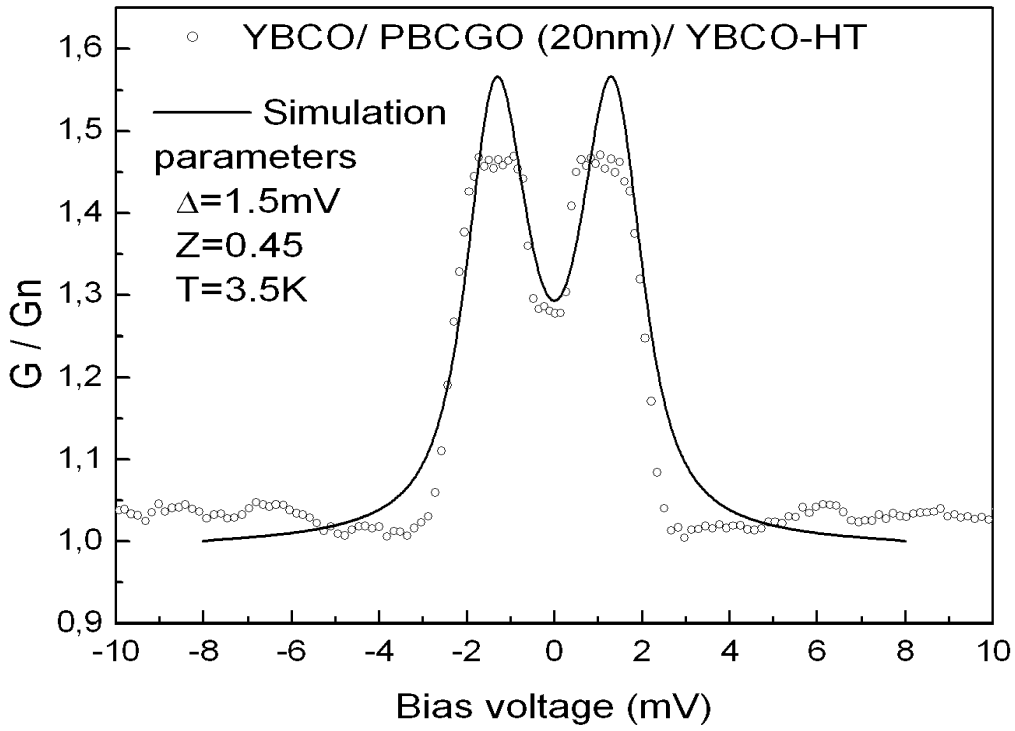

Figure 3.6: Differential conductance vs. voltage of a trilayer with 20 nm barrier together with the BTK simulation (solid line). The parameters used for the simulation are: Δ =1.5 meV, T = 3.5 K and $Z = 0.45$.

where v_n is the Fermi velocity in the normal metal.
De Gennes developed his theory for the so–called "dirty limit" i.e., $\ell \ll \xi_n$, where ℓ is the elastic mean free path. This assumption leads to some advantages. For example, some details of the *SN* interface become less important, so that the motion of Cooper pairs across the interface can be described by diffusion processes. The coherence length in the dirty limit is given by

$$\xi_{nd} = \sqrt{\xi_n \, \ell/3} \equiv \left(\frac{\hbar D}{2\pi k_B T} \right)^{1/2} \tag{3.4}$$

where $D = v_n \ell_n / 3$ is the diffusion coefficient.
The dirty limit holds for all low T_c devices. For example, in a normal metal–low T_c superconductor junction [70], the coherence length can be larger than 600 nm at 4.2 K while the mean free path is approx. 100 nm.

The critical current of a *SNS* contact is influenced by the degree of overlap of the wave function of the superconducting electrodes i.e., the value of the pair

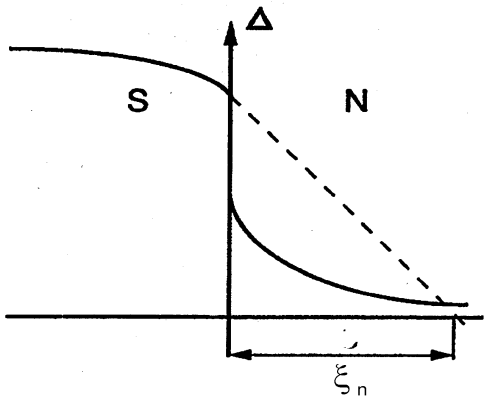

Figure 3.7: Profile of the superconducting order parameter across the *SN*–interface. ξ_n denotes the decay length in the normal metal. Taken from Ref. [69].

potential at the *SN* interface. The expression for the superconducting current is $I_s = I_c sin\phi$ where

$$I_c = \frac{\pi}{2eR_N}\sqrt{\Delta_1\Delta_2}. \tag{3.5}$$

This expression also characterizes the quality of the junction by means of the value of the product I_cR_N.
For high temperature superconductors the ratio ℓ/ξ_n is associated with a crossover temperature $T_o = 3\hbar v_f/2\pi k\ell$, well above holds the clean limit and well below holds the dirty limit. In the next section the proximity effect in HTSCs is discussed.

3.4.2 Proximity effect in HTSC's

A detailed study of the proximity effect in the dirty limit with different boundary conditions was made by Kupriyanov *et al.* [71]. They characterized the interface introducing two dimensionless parameters

$$\gamma = \rho_s\xi_s/\rho_n\xi_n, \quad \gamma_B = R_B/\rho_n\xi_n \tag{3.6}$$

where $\rho_{s,n}$ and $\xi_{s,n}$ are the resistivity and coherence length of the superconducting electrode (S) and normal conducting barrier (N) respectively, R_B is the specific resistance of the interface. The value of the γ parameter reflects the degree of the order parameter suppression in the S region. $\gamma \gg 1$ denotes that the

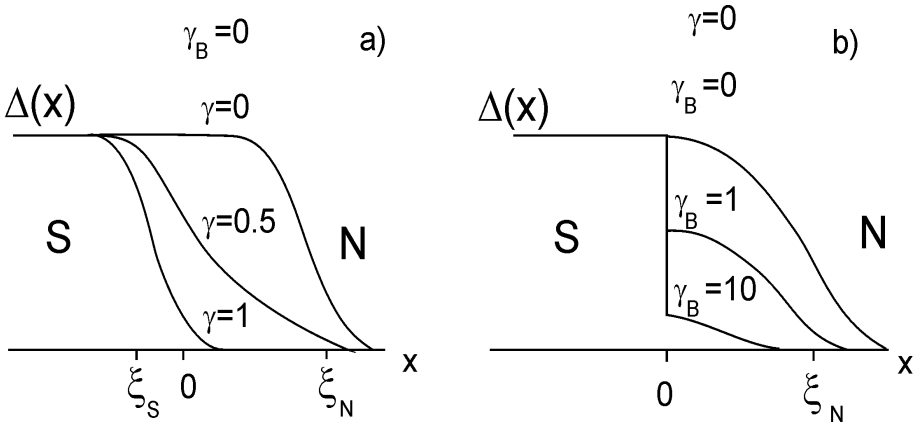

Figure 3.8: Behavior of the order parameter at the *SN* interface depending on the parameters γ and γ_B. From Ref. [71].

superconducting order parameter in the S part is strongly depressed over a length scale ξ_s due to the diffusion of the quasiparticles from N to S (assuming that a good contact between N and S and no barrier exists). In the opposite limit, if $\gamma \ll 1$ the order parameter is almost constant up to the interface. In this way $\gamma \gg 1$ and $\gamma \ll 1$ defines a "soft" and "rigid" *SNS* junction, respectively (see Fig. 3.8). On the other hand, the parameter γ_B describes the jump of the order parameter at the interface i.e., the existence of a potential at the interface.

Kupriyanov *et al.* estimated the value of both parameters in contacts between $YBa_2Cu_3O_{7-x}$ and noble metals, such as Au and Ag, in two possible configurations: perpendicular and parallel to the c–axis. The thus derived values of γ indicate a strong depression of the order parameter due to the metal. They are summarized in table 3.1. For the $YBa_2Cu_3O_{7-x}$ /$PrBa_2Cu_3O_{7-y}$ structures, the situation was quite different than in the *SN* structure with low N resistiv-

	γ	γ_B	R_B
$c_\perp$	$\sim 10^2$	$\sim 10^4$	$10^{-7}\,\Omega\,\mathrm{cm}^2$
$c_\parallel$	~ 5	~ 20	$10^{-11}\,\Omega\,\mathrm{cm}^2$

Table 3.1:
Estimated γ and γ_B parameters for the *SN* junction between the YBCO material and noble metals. After Ref. [71].

ity [72]. Using experimental data for $PrBa_2Cu_3O_{7-y}$, ρ_n between 0.3 Ω cm and 3 Ω cm, $\xi_n \sim 6 \times 10^{-7}$ cm and $R_B < 10^{-8}\,\Omega\,cm^2$ Boguslavskij *et al.* [73] obtained $\gamma \sim 10^{-4}$ and γ_B between 0.05 and 0.1. This means that the depression of the superconducting order parameter of $YBa_2Cu_3O_{7-x}$ due to the contact with $PrBa_2Cu_3O_{7-y}$ is negligible from the view of the proximity effect parameters, especially in the direction perpendicular to the planes.

3.5 Results for trilayer grown at T_s = 760°C

Until now the *(dI/dV)–V* measurements in superlattices and trilayers with different barriers showed similar behavior. Despite the nominal insulating character of the barrier its transparency seems to be larger than zero. Apparently the exchange of $PrBa_2Cu_3O_{7-y}$ for Ga–doped $PrBa_2Cu_3O_{7-y}$ did not affect the tunneling conductance characteristic. As mentioned in the previous section, the values of γ and γ_B for $YBa_2Cu_3O_{7-x}$ /$PrBa_2Cu_3O_{7-y}$ contacts are very small. This indicates that the depression of Δ in $YBa_2Cu_3O_{7-x}$ is almost negligible. The reason why in the present case the insulating layer barrier behaves differently may be attributed to the preparation conditions. In this section, differential conductance measurements of samples prepared at substrate temperature of 760°C are presented. A lowering of T_s should diminish possible interdiffussion process between both materials, and thus leads to sharper interfaces.

Differential conductance measurements

The differential conductance measurements on $YBa_2Cu_3O_{7-x}$/$PrBa_2Cu_{2.9}Ga_{0.1}O_{7-y}$/ $YBa_2Cu_3O_{7-x}$ trilayers prepared at T_s = 760°C exhibit different features than the samples presented in the previous section. Figure 3.9 shows the $G(V)$ dependence of a trilayer with a 20 nm thick $PrBa_2Cu_{2.9}Ga_{0.1}O_{7-y}$ insulating layer barrier (sample YBCO/PBCGO (20nm)/YBCO–LT) at different temperatures. Two different voltage regimes can be distinguished. For $V > 20$ mV the differential conductance is almost independent of temperature, while $G(V)$ increases with increasing temperature for the region between 7 mV and 20 mV. The background conductance increases with increasing bias voltage, whereas at zero bias a conductance peak appears. This peak decreases with increase T and disappears at T ≈ 50 K. The appearance of a zero bias conductance peak (ZBCP) could suggest Andreev reflection at the interface, however the nature of the barrier in

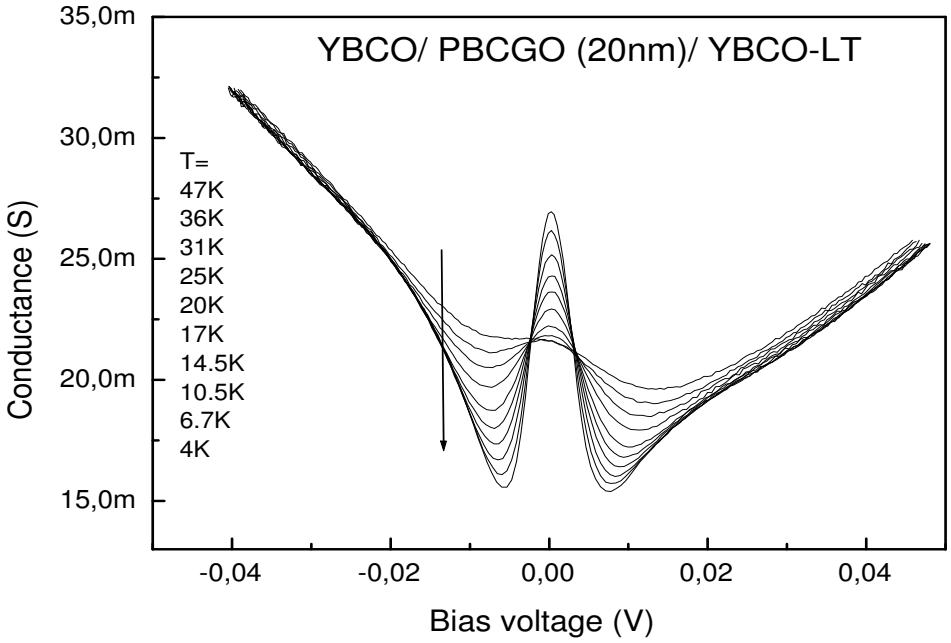

Figure 3.9: Dependence of the differential conductance on the bias voltage at different temperatures for a sample with a 20 nm thick barrier.

these trilayers is insulating. This fact indicates that the occurrence of this peak has a different origin.

A change in the ZBCP as a function of the junction resistance was observed in Au–$YBa_2Cu_3O_{7-x}$ single crystal junctions by Srikanth *et al.* [74]. By adjusting the contact pressure in a point–contact junction a continuous transition from tunnel (*N–I–S*) to metallic (barrierless *N–S*) behavior was observed. This experiment reveals the possibility to tune the character of the interface, namely the scattering potential H (see Sec. 3.1). The change in the shape of the background conductance and the appearance of the ZBCP in our trilayers by lowering the substrate temperature indicates that the interface is very sensitive to the preparation conditions, in particular the substrate temperature.

Figure 3.9 shows an additional feature: the background conductance curve is asymmetric. In order to obtain more information about the barrier, the differential conductance- voltage characteristic was studied applying conventional tunneling theory. After Brinkman *et al.* [75] and Simmons [76] the electron tunneling through a thin insulating layer between two metal electrodes causes roughly

a parabolic shape in the $G(V)$ dependence, if the applied voltage is much less than the barrier height. The shift of the conductance minimum to a non–zero voltage is attributed to the asymmetry in the potential barrier shape i.e., the different work functions of the electrodes.

The (dI/dV)–V of the sample YBCO/PBCGO (20nm)/YBCO–LT at 4 K was fitted using the expression

$$\frac{G(V)}{G(0)} = 1 - \left(\frac{A_o \Delta\varphi}{16\bar{\varphi}^{3/2}}\right) eV + \left(\frac{9}{128}\frac{A_o^2}{\bar{\varphi}}\right)(eV)^2, \tag{3.7}$$

where $G(0) = (3.16\times10^{10}\sqrt{\bar{\varphi}}/d)exp(-1.025\, d\sqrt{\bar{\varphi}})$, $\Delta\varphi = \varphi_2 - \varphi_1$, $A_o = 4\sqrt{2m}\, d/3\hbar$ and d is the thickness in Å. The following parameters were obtained: $d = 200$ Å, the average barrier height $\bar{\varphi} = 6.16$ V and the barrier asymmetry $\Delta\varphi = 0.8$ V. The corresponding fit appears in Fig. 3.10. The value $\bar{\varphi} = 6.16$ V obtained here for a 200 Å barrier is relatively large in comparison with the energy gaps of a

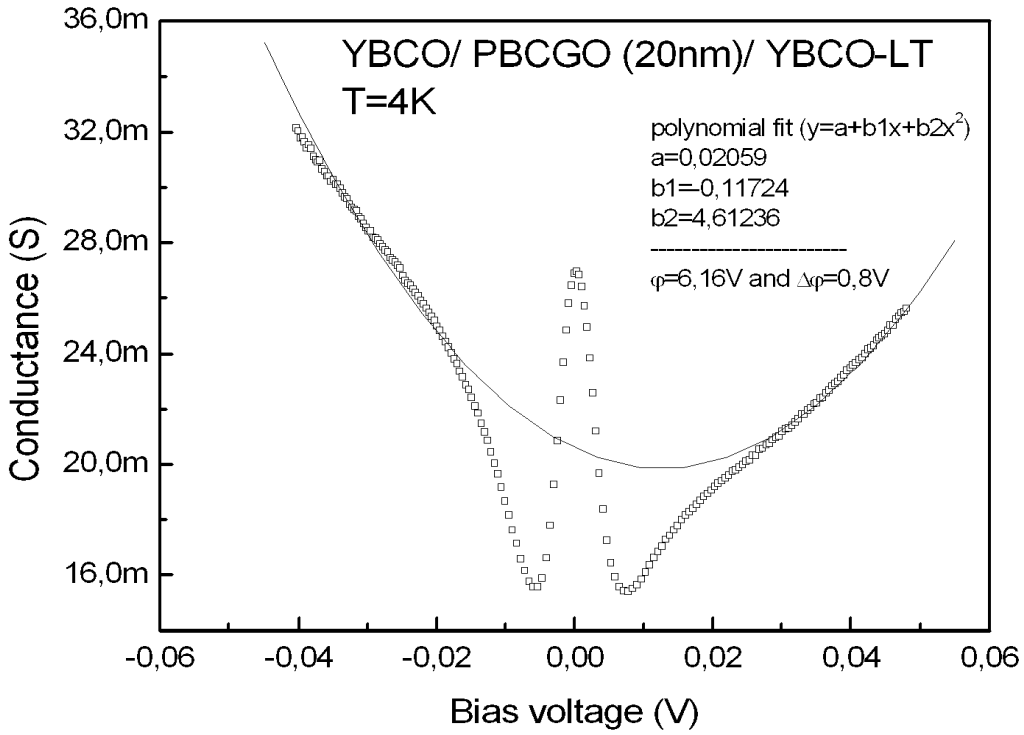

Figure 3.10: *G(V)* dependence of the sample YBCO/PBCGO (20nm)/YBCO–LT at T = 4 K together with the polynomial fit according to Eq. (3.7). The parameters are $d = 200$ Å, $\bar{\varphi} = 6.16$ V and $\Delta\varphi = 0.8$ V.

semiconductor. However, this value seems to be plausible because of the insulating character of the $PrBa_2Cu_{2.9}Ga_{0.1}O_{7-y}$. The Simmons analysis was applied previously by Cucolo *et al.* [77] to their conductance data using natural tunnel barriers. For layer thicknesses between 18 Å and 22 Å, they found an average height of $\bar{\varphi} = 1.6$ V. For Pb/Y124 junctions with $d = 15$ Å, the average height was $\bar{\varphi} = 1.9$ V.

3.6 Zero bias conductance peak

There are several models to explain the appearance of a zero bias conductance peak. The simplest reason for the appearance of a ZBCP may be the presence of a supercurrent through the junction. A possible Josephson current can be detected by either measuring the current dependence of the voltage across the junction using a high resolution current source and voltmeter (as suggested by Becherer [56]), or by measuring the magnetic field dependence of the critical current.

Earlier experiments on $YBa_2Cu_3O_{7-x}$ /*N* tunnel junctions showed the presence of a ZBCP. This feature was originally attributed to spin–flip scattering between tunneling quasiparticles and magnetic impurities inside the barrier. Later it was found that the order parameter symmetry of the HTSC's is dominated by a *d*–wave component [78]. Tunneling spectroscopy experiments using *ab*–oriented HTSC's in grain boundary and *N/I/S* junctions displayed ZBCP. It was shown that the ZBCP is a direct consequence of the $d_{x^2-y^2}$ symmetry of the pair potential. Its presence is a manifestation of the formation of Andreev bound states at the Fermi energy (zero energy) near a reflecting interface, when the angle between the lobe direction of the $d_{x^2-y^2}$ wave pair potential and the normal to the interface is nonzero [79–81]. Since Andreev bound states can carry current, they produce a pronounced zero bias conductance peak. In contradistinction to the pure *ab* tunneling conductance experiments, Lesueur *et al.* [82] measured the tunneling conductance of $YBa_2Cu_3O_{7-x}$ /Pb junctions as a function of crystallographic orientation. Their results for tunneling perpendicular to the CuO_2 planes did not reveal a ZBCP.

As already mentioned, another possible origin of the manifestation of a ZBCP is the presence of paramagnetic atoms in the barrier which can interact with tunneling quasiparticles. This phenomenon is explained in the following section.

3.7 The Anderson–Appelbaum model

The Anderson–Appelbaum model describes a situation, where the barrier of a tunnel junction contains paramagnetic moments that are localized in the interface between the electrode and the insulator. The differential conductance becomes temperature and magnetic field dependent near zero bias voltage; this is also called zero bias anomaly (ZBA). The conductance peak is the result of the spin–flip interaction between quasiparticles and magnetic impurities in analogy to the resistance minimum in magnetic alloys at low temperature (Kondo effect) [83].

In the Anderson–Appelbaum theory [84, 85] it was shown that a localized magnetic state in the barrier couples the tunneling conduction electrons or holes of both electrodes leading to an exchange scattering. The total conductance can be regarded as a sum of three conducting channels in parallel

$$G = G_1 + G_2 + G_3. \tag{3.8}$$

The first contribution corresponds to the scattering of electrons without any spin interaction (normal tunneling process), the second is the spin exchange processes contribution that depends on the applied magnetic field, and the third describes a Kondo–type contribution where an electron is scattered under spin–flip by the magnetic interaction, G_3 depends on bias voltage and temperature.

The first two terms contribute to the background conductance. Consequently, the excess conductance stems from the last term, and G_3 is written as [86]

$$\Delta G(V,T) \approx -\ln\left(\frac{e|V| + nkT}{E_o}\right), \tag{3.9}$$

where the constant n has the value 1.35 and E_o defines a cutoff energy[2]. The conductance peak has a logarithmic voltage dependence and the zero bias conductance increases logarithmically with decreasing temperature.

3.8 Comparison with experimental results

In the present section the tunneling conductance measurements of trilayers prepared at $T_s = 760°C$ are analyzed with regard to the Anderson–Appelbaum theory. In order to facilitate the comparison of experimental data and theory, an

[2]The value of E_o must be such that $kT \ll e|V| \ll E_o$ for all V and T.

even conductance $G_E(V)$ was defined [87]

$$G_E(V) = [G(+V) + G(-V)]/2. \tag{3.10}$$

Because of the appearance of superconductivity in the high–T_c electrode, the conductance for voltage bias near zero is depressed by a certain unknown quantity. For that reason it is convenient to determine the quantity ΔG as the difference between the maximum and minimum value of the even conductance at zero voltage. $G_{min}(0)$ corresponds to the extrapolated value of the conductance at $V = 0$ mV in the depressed regime if the ZBCP were zero (see Fig. 3.11). Using the expression (3.9), the temperature dependence of the zero–bias even conductance of a trilayer with 20 nm thick $PrBa_2Cu_{2.9}Ga_{0.1}O_{7-y}$ barrier was derived and is shown in Fig. 3.12 in a semilogarithmic plot. It can be noted that almost all

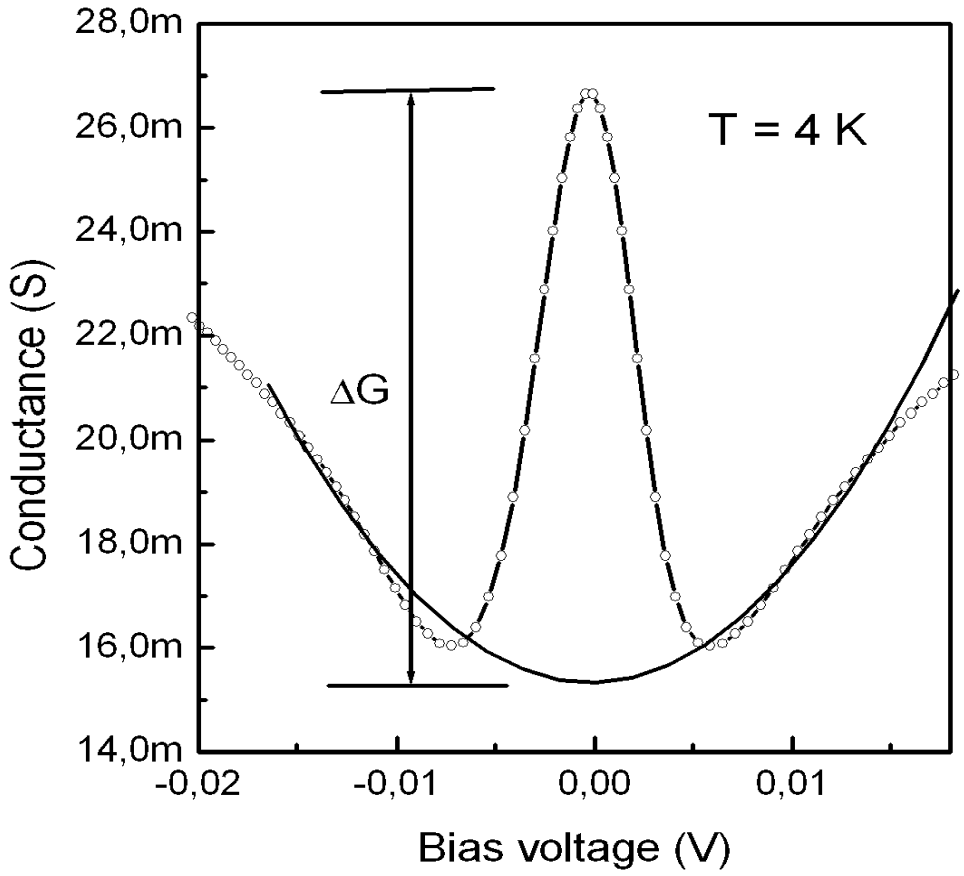

Figure 3.11: The quantity ΔG was calculated as the difference of the maximal value of the conductance and the minimal extrapolated value at $V = 0V$.

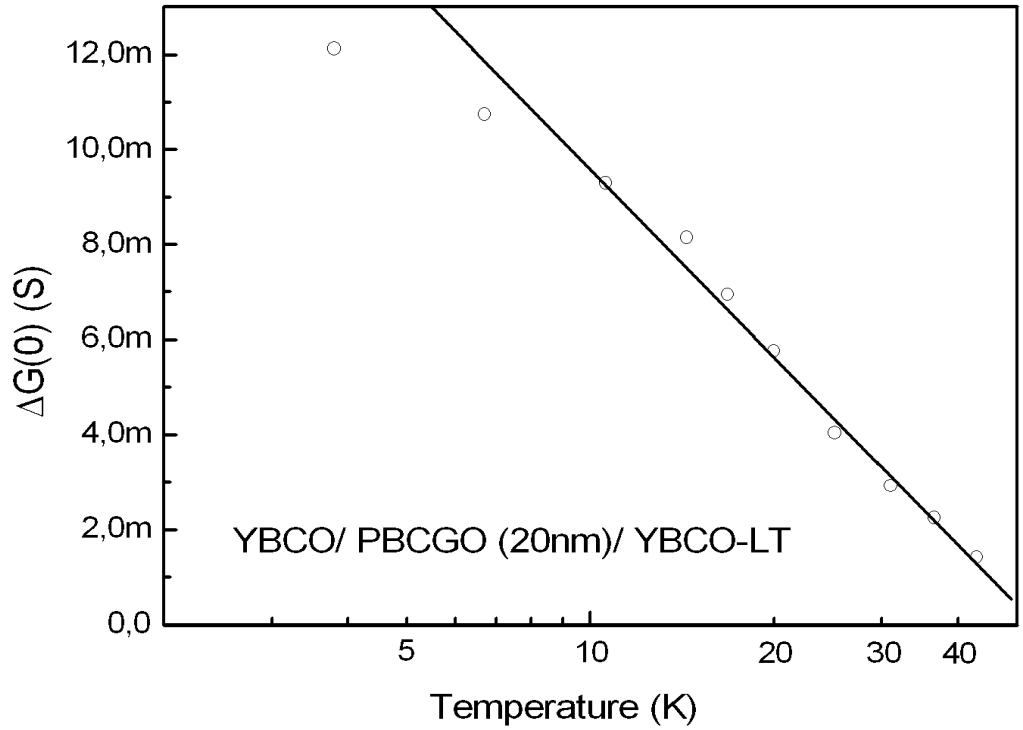

Figure 3.12: Temperature dependence of the zero–bias even conductance of a YBCO trilayer with 20 nm thick PBCGO barrier. (The straight line is a visual aid.)

points lie on a straight line; a deviation from this tendency occurs for the points at lower temperatures.

The $G_E(V)$ relationship at T = 4 K, 6.7 K and 10.6 K is shown in Fig. 3.13. These temperatures were chosen so that the condition $k\mathrm{T} \ll e\mathrm{V}$ was fulfilled. A linear dependence is observed over a narrow voltage range between 2 mV and 5 mV. For lower voltages, the differential conductance increases slower than $\ln V$, because kT becomes comparable with eV. A deviation above 6 mV appears because both the quadratic term of the background conductance becomes important and the suppression of the differential conductance due to the superconductivity is not occurring in this regime.

A discrepancy between the experimental results and the Anderson–Appelbaum model prediction occurs as the temperature rises. According to the expression (3.9), as the temperature increases the conductance falls at all voltages. However in the experiment, there is a region in bias voltage above 2 mV, where $G(V)$ at one particular temperature is larger than the conductivity at lower temperature

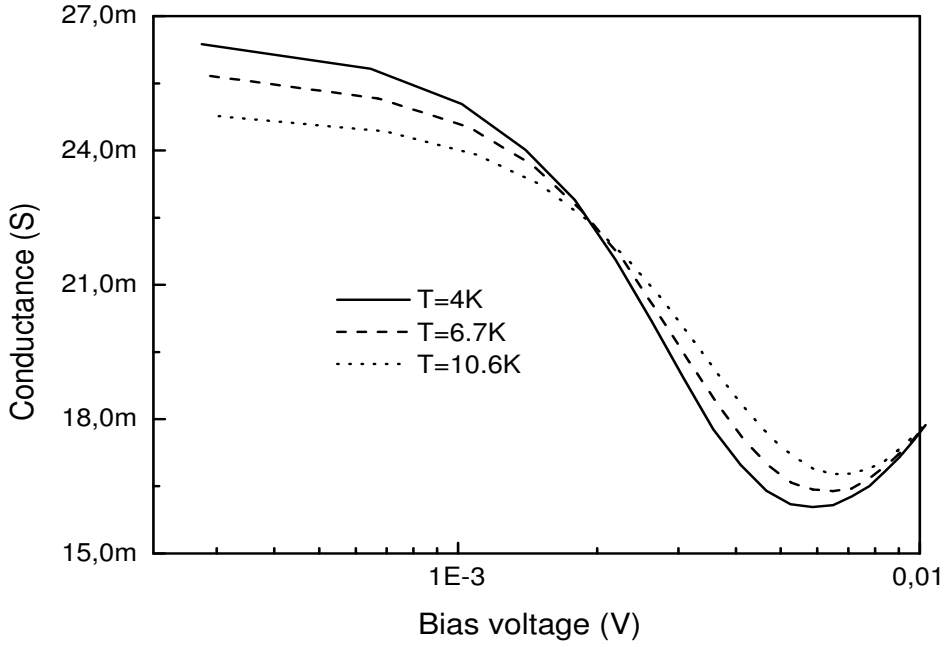

Figure 3.13: Differential conductance vs the logarithm of the bias voltage at three temperatures.

(Fig. 3.13). For a better illustration, Fig. 3.14 shows the numerical calculation of the function $\Delta G(V,T)$ for four temperatures. The cut–off energy [3] was chosen as 100 mV and the maximal value for V was 20 mV. The differential conductance curves do not cross each other until the bias value of $eV = E_o$.

In the Anderson–Appelbaum theory, the magnetic field dependence of the total conductance produces: a formation of a well in the spin exchange term G_2 of width $2g\mu_B H$ because the field splits the Zeeman levels of the impurity by $g\mu_B H$ and a splitting of the logarithmic peak in the G_3 term into two peaks. For $g\mu_B H/kT \gg 1$ where g is a measure of the impurity concentration and μ_B is the Bohr magneton and k is the Boltzmann constant, the G_3 term should be nearly quenched out at zero bias [88]. However, for a temperature of 4 K this condition is full filled for magnetics fields higher than 20 T. For the case of the sample YBCO/PBCGO (20nm)/YBCO–LT, the magnetic field dependence of

[3]The value of E_o cannot be less than 8 mV because the minimum of the conductance does not occur below this value.

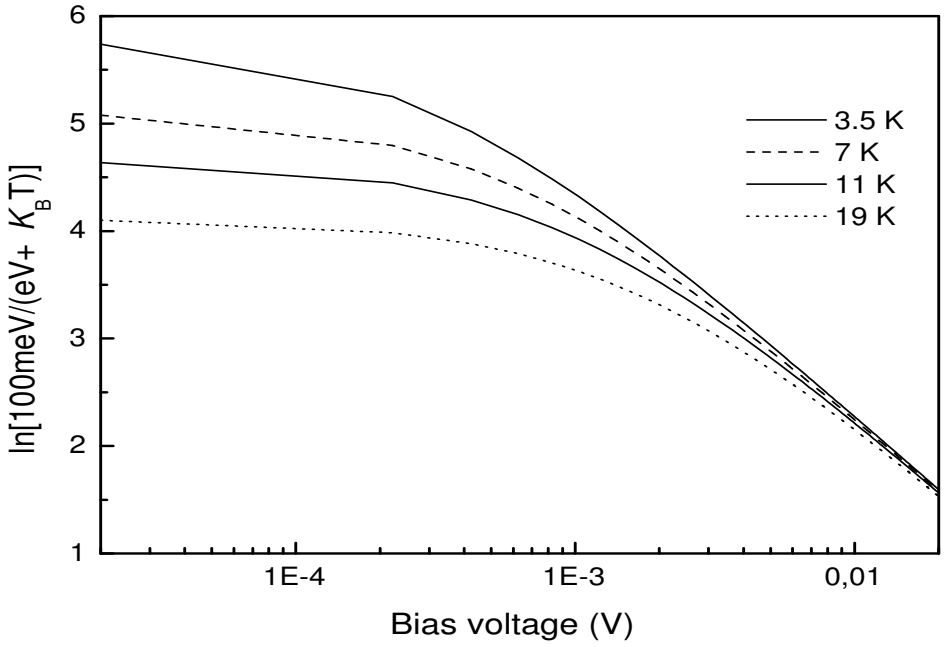

Figure 3.14: $G(V)$ in semilogarithmic representation calculated according to Eq. (3.9) at various temperatures.

the conductance peak was measured at 4 K, as the magnetic field increases, the peak becomes slightly broad and is depressed. This observation is plausible with the Anderson–Appelbaum theory (Fig. 3.15).

3.9 Discussion

The analysis of the ZBCP of the sample YBCO/PBCGO (20nm)/YBCO–LT agrees reasonably well with the Anderson–Appelbaum description. From the above results it is very likely that the occurrence of the ZBCP in the trilayer has a magnetic origin. Cucolo *et al.* [87] observed ZBCP in Fe–doped $YBa_2Cu_3O_{7-x}$/Pb junction, in which it is evident that the magnetic moments of the Fe atoms are responsible for such a peak. Other authors have ascribed it to the spin fluctuations in the cuprates. The magnetic behavior of the $RE Ba_2Cu_3O_7$ systems is determined by both, the rare–earth ion and Cu, which both have magnetic moments. Neutron diffraction experiment on powdered $PrBa_2Cu_3O_{7-y}$ revealed antiferro-

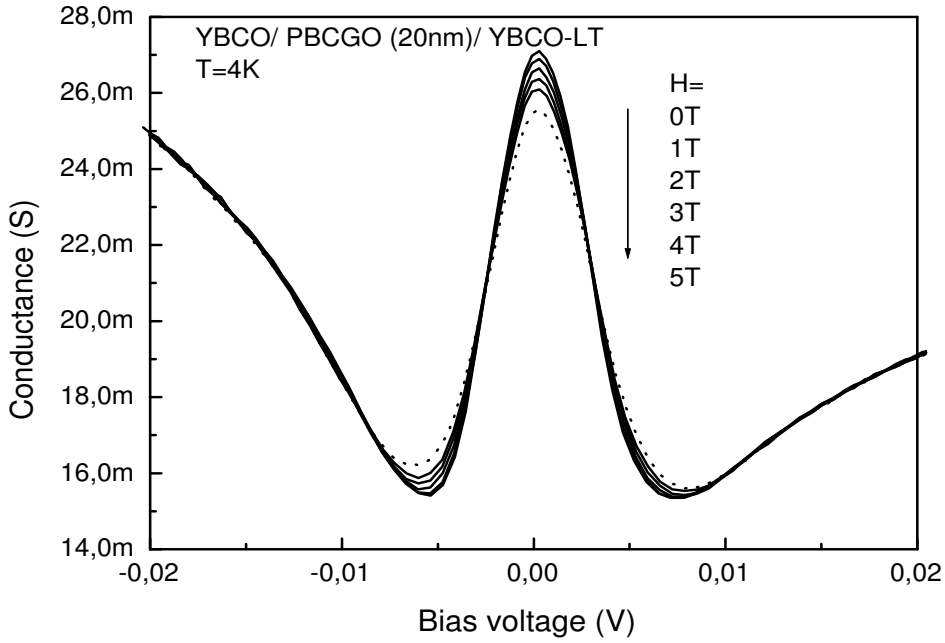

Figure 3.15: $G(V)$ dependence for different applied magnetic fields at T = 4 K. The increase of H suppress slightly the height of the ZBCP.

magnetic ordering of the Pr ions, with a moment $0.74\mu_B$ and a Néel temperature of 17 K [89]. On the other hand, one can distinguish between three sets of Cu layers. The first two sets have an oxygen between each Cu ions (CuO_2 planes) and the third one has oxygen ions only along the b axis (Cu–O chains)[4]. The Cu atoms in the plane exhibit an antiferromagnetic ordering with Néel temperatures about 525 K.

In the present work, there are two possible explanations where magnetic moments may come from. Firstly, one can suggest that the doping with Gallium may give rise to some disturbance in the antiferromagnetic ordering of $PrBa_2Cu_3O_{7-y}$, either in Pr positions or in the Cu–O planes or both, leading to a nonzero magnetic moment. Secondly, the formation of magnetic moments could take place at the interface. During the growth of a heterostructure, the substrate holder must change the position from target to target. During the $YBa_2Cu_3O_{7-x}$ layer

[4]The content of this oxygen is decisive for the electric behavior from an AFM insulator to a superconducting state. (See Chapter 5.)

growth a sudden interruption occurs and thereafter the layer is completed with $PrBa_2Cu_3O_{7-y}$, or vice versa. The repetitive process can lead to the formation of $Y_{1-x}Pr_xBa_2Cu_3O_{7-x}$ (where x is unknow) at each interface. Such a disorder in the interface could create paramagnetic defects.

Chapter 4

Superlattices

4.1 In–plane and out–of–plane resistivity in superlattices

The transport properties of $YBa_2Cu_3O_{7-x}/PrBa_2Cu_3O_{7-y}$superlattices were widely studied [9, 90–96] in order to investigate the degree of the interlayer coupling of $YBa_2Cu_3O_{7-x}$ layers separated by $PrBa_2Cu_3O_{7-y}$ "spacers". The main finding of earlier works was that the critical temperature of $YBa_2Cu_3O_{7-x}$ layers with few unit cells decreases approximately linearly with an increase of the thickness of the insulating barriers, this indicates that some interlayer interaction is necessary for the HTSC phenomenon. The critical temperature of superlattices having one unit cell $YBa_2Cu_3O_{7-x}$ saturates at $T_c \approx 30$ K by increasing the thickness of $PrBa_2Cu_3O_{7-y}$ spacer to about 20 nm. Such results led to the conclusion that superconductivity can occur in one single $YBa_2Cu_3O_{7-x}$ unit cell. However, the critical temperature is significantly reduced. Later experiments by Norton *et al.* [97] showed that using more conductive barriers, for example $Pr_{0.5}Ca_{0.5}Ba_2O_7$ and $Pr_{0.7}Y_{0.3}Ba_2Cu_3O_7$, the reduction of T_c was less remarkable than for superlattices with $PrBa_2Cu_3O_{7-y}$barriers. Norton concluded that the values of T_c and the transition width for these superlattices are not intrinsic to $YBa_2Cu_3O_{7-x}$ layers of a given thickness, but are strongly dependent on the boundary conditions and the barrier layer material.

The in–plane resistivity of $YBa_2Cu_3O_{7-x}$ /$PrBa_2Cu_3O_{7-y}$ superlattices can be regarded as the equivalent resistivity of independent $YBa_2Cu_3O_{7-x}$and $PrBa_2Cu_3O_{7-y}$ layers connected in parallel [98]. Using the formula $R = \rho(l/wd)$ where ρ is the resistivity, l is the length, w is the width and d is the thickness, the total resistivity

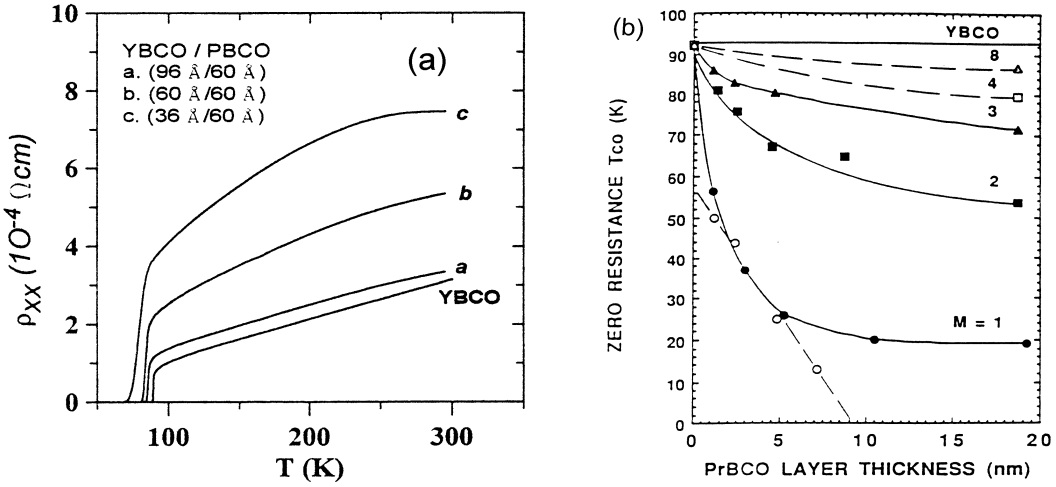

Figure 4.1: Resistance vs. temperature of $(YBa_2Cu_3O_{7-x})_n/(PrBa_2Cu_3O_{7-y})_m$ superlattices. (a) The normal resistance decreases as the $YBa_2Cu_3O_{7-x}$ slabs become thicker (From Ref. [98]). (b) Critical temperature vs. $PrBa_2Cu_3O_{7-y}$ layer thickness. Taken from Ref. [99].

of a superlattice can be expressed by

$$d/\rho_{SL}^{ab} = d_1/\rho_{Y-123}^{ab} + d_2/\rho_{Pr-123}^{ab}, \tag{4.1}$$

where ρ_{Y-123}^{ab}, ρ_{Pr-123}^{ab} and d_1, d_2 are the resistivity in the ab plane and total thickness of $YBa_2Cu_3O_{7-x}$ and $PrBa_2Cu_3O_{7-y}$ layers, respectively. Figure 4.1a shows the in–plane resistivity as a function of the temperature of $(YBa_2Cu_3O_{7-x})_n$ $/(PrBa_2Cu_3O_{7-y})_5$ superlattices with $n = 3$, 5 and 8 unit cells [98]. The total resistivity in the normal state decreases as the thickness of the $YBa_2Cu_3O_{7-x}$ layers increases. On the other hand, Fig. 4.1b shows how the critical temperature decreases systematically in superlattices when the thickness of the $YBa_2Cu_3O_{7-x}$slabs is fixed and the thickness of the $PrBa_2Cu_3O_{7-y}$ layers is increased [99].
The out–of–plane resistivity of $YBa_2Cu_3O_{7-x}/PrBa_2Cu_3O_{7-y}$superlattices corresponds to the equivalent resistivity of an array of $YBa_2Cu_3O_{7-x}$and $PrBa_2Cu_3O_{7-y}$ resistors in series. The total superlattice resistivity is given by

$$\rho_{SL}^{c} d = \rho_{Y-123}^{c} d_1 + \rho_{Pr-123}^{c} d_2 \tag{4.2}$$

where ρ_{Y-123}^{c}, ρ_{Pr-123}^{c} and d_1, d_2 are the c–axis resistivity and the thickness of $YBa_2Cu_3O_{7-x}$ and $PrBa_2Cu_3O_{7-y}$ respectively (according to the mentioned geometry).
In the present work the out–of–plane resistance of $(YBa_2Cu_3O_{7-x})_2/$ $(PrBa_2Cu_3O_{7-y})_m$

superlattices with $m = 3$, 5 and 9 unit cells (in the following denoted as $YBCO_2$ /$PBCO_3$, $YBCO_2$/$PBCO_5$ and $YBCO_2$/$PBCO_9$ respectively) was measured. Figure 4.2 shows the temperature dependence of the normalized out–of–plane resistance of a 50 μm×50 μm mesa of the $YBCO_2$/$PBCO_3$, $YBCO_2$/$PBCO_5$ and $YBCO_2$/$PBCO_9$ superlattices. The temperature dependence of the perpendic-

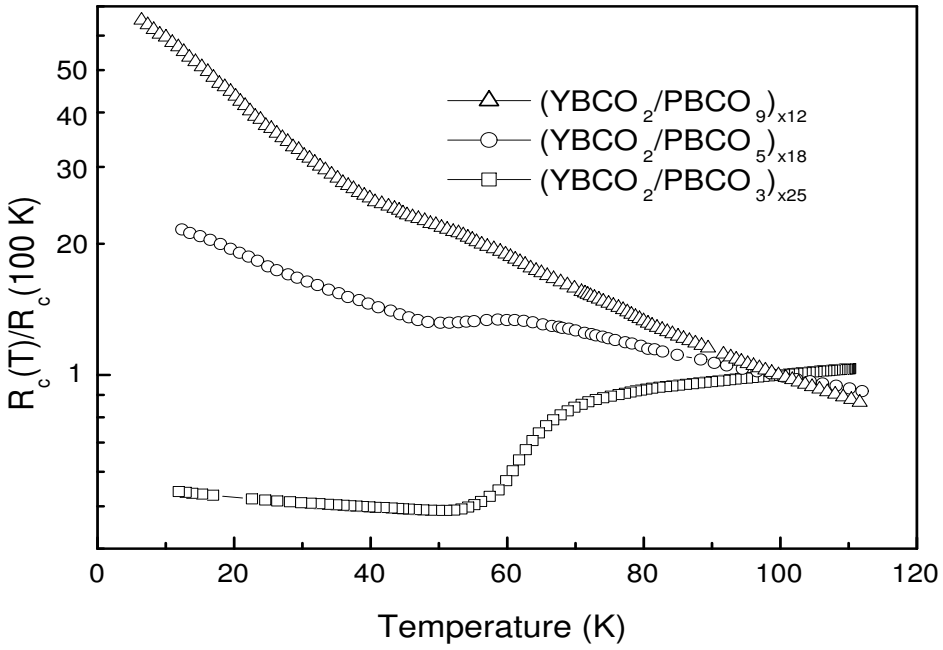

Figure 4.2: Temperature dependence of the normalized out–of–plane resistance of 50×50 $(\mu m)^2$ mesas of $(YBa_2Cu_3O_{7-x})_2/(PrBa_2Cu_3O_{7-y})_m$ superlattices with $m = 3$, 5 and 9 unit cells. As the thickness of the barrier increases the semiconducting behavior of $PrBa_2Cu_3O_{7-y}$ at low temperatures becomes dominant.

ular resistance of the sample $YBCO_2$/$PBCO_3$ above approx. 80 K exhibits an linear behavior. This is an indication that the normal state transport properties are determined by the in–plane resistance. The samples $YBCO_2$/$PBCO_5$ and $YBCO_2$/$PBCO_9$, on the contrary, show an increase in the resistance by decreasing the temperature well above T_c, this is due to the increase of the resistance of the $PrBa_2Cu_3O_{7-y}$ layers in series by lowering the temperature. The situation is more dramatic at low temperature. While the sample $YBCO_2$/$PBCO_3$ with thin barriers shows superconducting behavior, the resistance of the sam-

ples $YBCO_2/PBCO_5$ and $YBCO_2/PBCO_9$ increases strongly as the temperature decreases, where the c–axis properties of the barrier dominates. The resistance of the sample $YBCO_2/PBCO_3$ starts to drop around 70 K. Only a tiny change in the resistance can be observed at lower temperature for the samples $YBCO_2/PBCO_5$ and $YBCO_2/PBCO_9$. This change is related to the superconducting phase transition of the respective sample. Clearly, the T_c of two $YBa_2Cu_3O_{7-x}$ unit cells is lower than the critical temperature of the bulk. As the thickness of the barrier increases the critical temperature of the superlattices decreases and the transition (ΔT) broadens. This observation is in agreement with the literature [99]. If the thickness of the $YBa_2Cu_3O_{7-x}$ layer increases, the critical temperature of the superlattice should be closer to T_c of the bulk. Figure 4.3 shows the temperature dependence of the out–of–plane resistance of a 16 μm $\times$ 16 μm mesa of a $(YBa_2Cu_3O_{7-x})_4/(PrBa_2Cu_{2.9}Ga_{0.1}O_{7-y})_{12}$ superlattice (sample $YBCO_4/PBCGO_{12}$). The transition temperature of the superlattice with four $YBa_2Cu_3O_{7-x}$ unit cells almost reaches the T_c of the bulk, despite of the fact that the barrier is more insulating and thicker than in sample $YBCO_2/PBCO_9$.

4.2 Properties of the $PrBa_2Cu_{2.9}Ga_{0.1}O_{7-y}$ barrier

In chapter three it was mentioned, that the variable range hopping mechanism was suggested as possible conduction process for $PrBa_2Cu_3O_{7-y}$ barriers. However, a more general description which takes in consideration different conduction channels depending on barrier layer thickness and temperature regime was also proposed [100–102]. For extremely thin barriers (few Å) the elastic tunneling process dominates. As the barrier becomes thicker new conduction channels appear. According to Glazman's and Matveev's theory for amorphous semiconductors [100], the current involves a hopping conduction process via localized states. As the barrier layer thickness increases the number of localized states increases. A general expression for the dependence of the junction conductance on the temperature is given by [102]

$$G(T) = G_{dir} + G_{res} + \sum_{n\geq 2} G_n(T) + \sigma_0 d^{-1}\, exp(-(T_0/T)^{1/4}) \qquad (4.3)$$

where d is the insulator layer thickness and $T_o = 1/N(0)d^3$. The first two terms represent the elastic contribution of tunneling (direct and resonant), the third term is related to the hopping conduction through n localized states and the

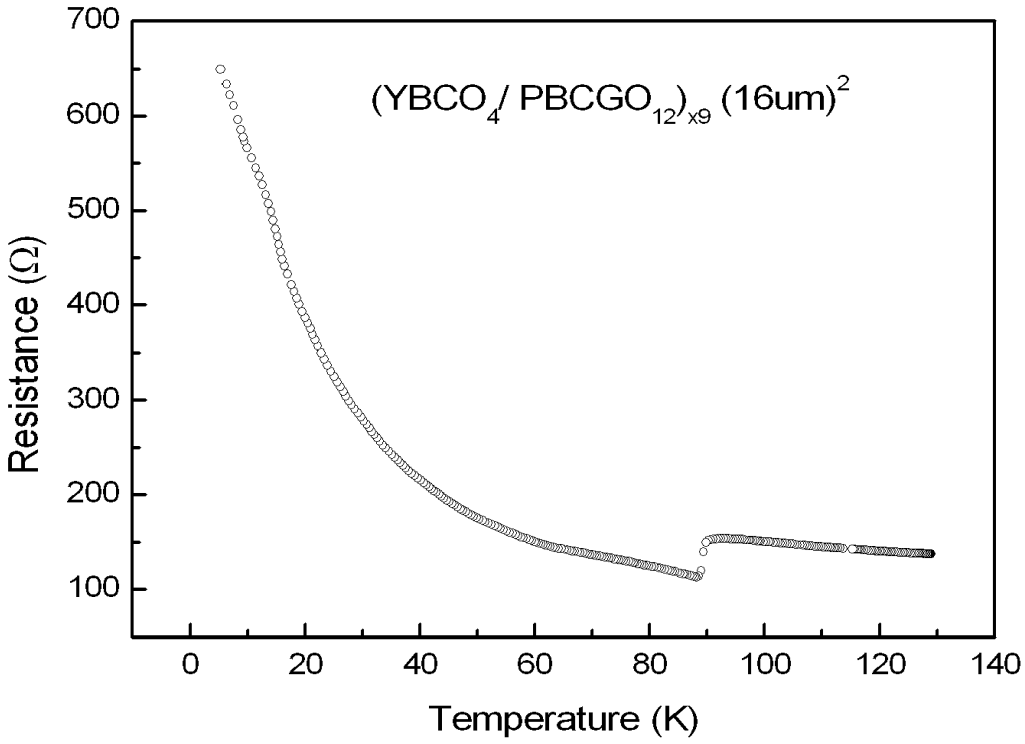

Figure 4.3: $R_c(T)$ dependence of the sample $YBCO_4/PBCGO_{12}$. For four YBCO layers the transition temperature is almost the T_c of the bulk.

last term denotes the variable range hopping conduction via a large number of localized states. A similar expression exists also for the voltage dependence of the conductance.

Experimental results show that for $PrBa_2Cu_3O_{7-y}$ barriers up to 20 nm in trilayers [103–105], the predominant transport mechanisms are resonant tunneling and hopping conduction via a small number of localized states. On the other hand, the behavior of $PrBa_2Cu_3O_{7-y}$ barrier layers in $(YBa_2Cu_3O_{7-x})_2$/ $(PrBa_2Cu_3O_{7-y})_7$ exhibit a VRH mechanism [11]. Within this framework, one can study the transport across $PrBa_2Cu_{2.9}Ga_{0.1}O_{7-y}$ barriers in $YBa_2Cu_3O_{7-x}$ / $PrBa_2Cu_{2.9}Ga_{0.1}O_{7-y}$ superlattices. As mentioned in the last section, the temperature dependence of the resistance of the sample $YBCO_4/PBCGO_{12}$ below T_c increases enormously by lowering T in the same fashion as semiconductors do. This sample contains eight junctions in series, in which each junction has an insulating barrier of approx. 14 nm thickness. The resistivity of such a barrier should follow the variable range hopping transport. Figure 4.4 shows the resistivity vs.

temperature dependence of a 16×16 μm^2 mesa of the sample $YBCO_4/PBCGO_{12}$ in a $ln\rho(T)$ *vs.* $T^{-1/4}$ plot. In the region between approx. 30 K and 66 K the relation is linear which agrees with previous results [11]. Above this region thermally activated processes take place. In order to have a better understanding of the actual mechanism, the *R(T)* dependence is also represented in a σ *vs.* $T^{4/3}$ plot (Fig. 4.5), a linear relation was observed between approx. 10 K and 45 K i.e., a transport process that involves two localized states in the barrier. At first sight one could assert that a crossover take place between transport via localized states and VRH as the temperature increases, however these two results reveal that the actual transport mechanism is more complex because it involves several processes.

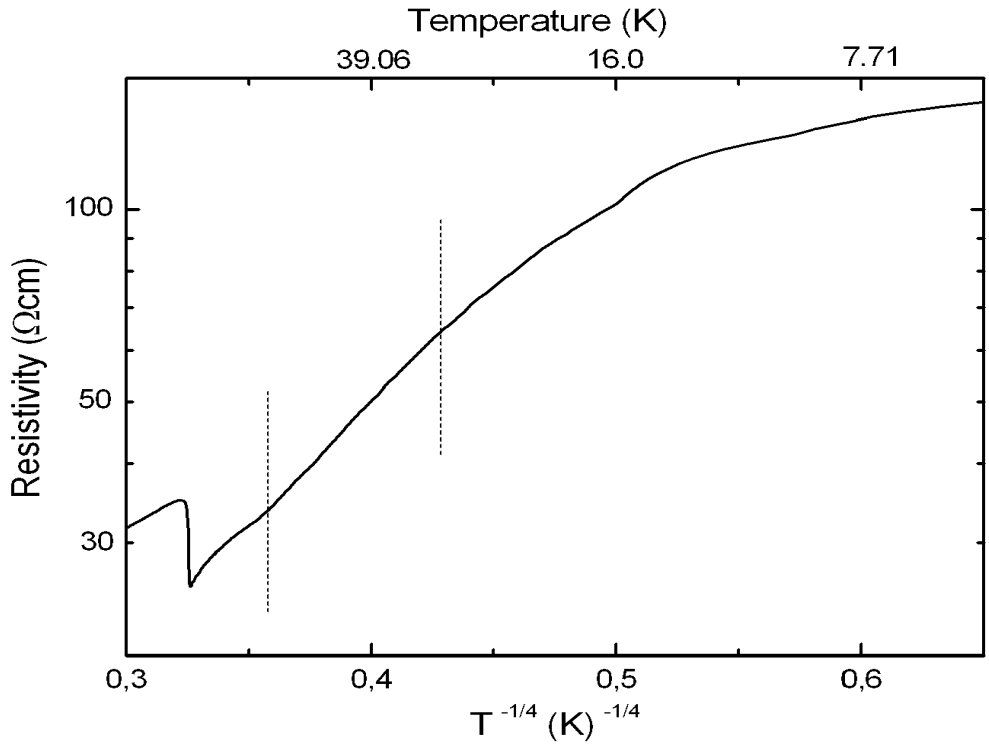

Figure 4.4: ln $\rho(T)$ *vs.* $T^{-1/4}$ plot of a $16 \times 16(\mu m)^2$ mesa of the $YBCO_4/PBCGO_{12}$ superlattice. A linear relationship is observed between 30 K and 66 K which indicates a variable range hopping process.

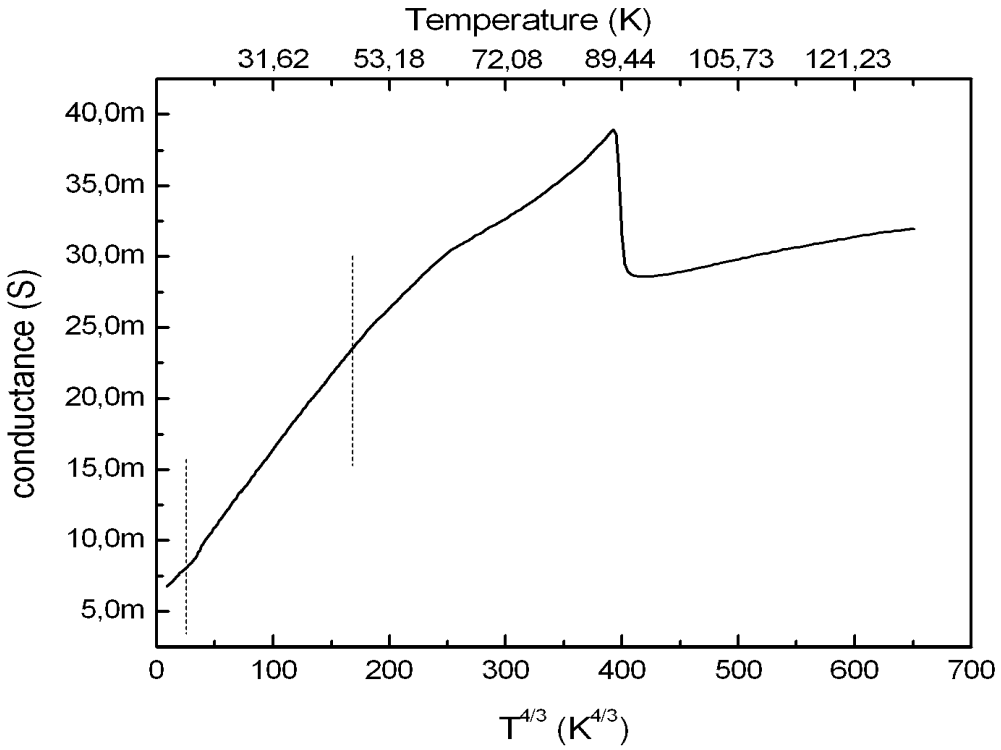

Figure 4.5: σ(T) *vs.* $T^{4/3}$ plot of a 16×16 $(\mu m)^2$ mesa of the $YBCO_4/PBCGO_{12}$ superlattice. A linear relationship is observed between 10 K and 45 K, which indicates a transport mechanism via two localized states.

4.3 Conductivity measurements of superlattices prepared at $T_s = 840°C$

In this section, tunnel conductivity measurements are presented. They were carried out on $YBa_2Cu_3O_{7-x}/PrBa_2Cu_3O_{7-y}$and $YBa_2Cu_3O_{7-x}/PrBa_2Cu_{2.9}Ga_{0.1}O_{7-y}$ superlattices prepared at a substrate temperature of 840°C. Figure 4.6 shows *G–V* curves for different temperatures of a 50×50 μm^2 mesa of a $(YBa_2Cu_3O_{7-x})_2$ $/(PrBa_2Cu_3O_{7-y})_{10}$ superlattice (sample $YBCO_2/PBCO_{10}$). This sample exhibits three features which are common in multilayers prepared at the substrate temperature of 840°C. First, the shape of these curves is symmetric with respect to zero bias, and they show strong bias voltage dependence. Second, the *G(V)* dependence shows an excess of differential conductance in the subgap region i.e., the value of the differential conductance at $V < m\,2\Delta/e$ (m is the number of bilayers) is larger than its value at high bias voltage. This feature resembles

metallic behavior. Third, the tunnel conductance curves show two maxima. The voltage values of the differential conductance maxima are related to the value of two times the gap times the number of junctions in series.

Another characteristic of these superlattices having large size mesas is the occurrence of a negative differential conductance at high bias voltages. This is the result of self heating effects at the junction interfaces. Large current density flows through the mesa leading to local overheating that can drive regions of the $YBa_2Cu_3O_{7-x}$ slabs close to the interface into the normal state. The resistance of the outermost regions adds in series to the barrier resistance so that the total conductance is reduced. Especially dramatic is the situation at low temperature, as the bias voltage is increased the local temperature grows so that a measurement in thermal equilibrium is not longer possible. The temperature sensor registered during the *G(V)* measurement an increase of temperature of a few degrees. The voltage–current characteristic of the sample $YBCO_2/PBCO_{10}$ shows clearly how at high bias voltage the current decreases (Fig. 4.7).

The overheating is a problem intrinsic to all small size microelectronic components. Small structures can carry transport currents that are large enough to result in large self–heating due to power dissipation in the reduced volume and due to poor thermal contact to the environment. A manifestation of such effects is a backbending of the current–voltage characteristic as is usually observed at large bias on small mesa structures of BSCCO [106–110]. This problem was studied by Krasnov *et al.* [111,112] in a mesa geometry on top of a substrate. For his model he assumed a disk–like mesa on a top of a bulk single crystal, after solving the stationary heat diffusion equation $\vec{q}_{th} = -\kappa \vec{\nabla} T$, where $\vec{q}_{th}$ is the dissipated power density and κ is the thermal conductivity. Using the appropriate boundary conditions he obtained[1]

$$\Delta T \approx \frac{\pi q_{th}\, a}{4\kappa_{ab}} \tag{4.4}$$

where ΔT denotes the temperature difference between the bottom of the mesa and the bottom of the crystal, a is the radius of the mesa and κ_{ab} is the thermal conductivity[2] in plane. This means that the self–heating increases linearly with the radius of the mesa. Usually the mesas have metallic contacts on the top. This, together with the base electrode, helps to cool the mesas.

[1]The exact solution is valid only for a semi–infinite bulk crystal. However, under some considerations this solution is applicable to a finite crystal.

[2]In the particular case of the HTSCs the thermal conductivity coefficient is anisotropic with $\kappa_{ab} > \kappa_c$.

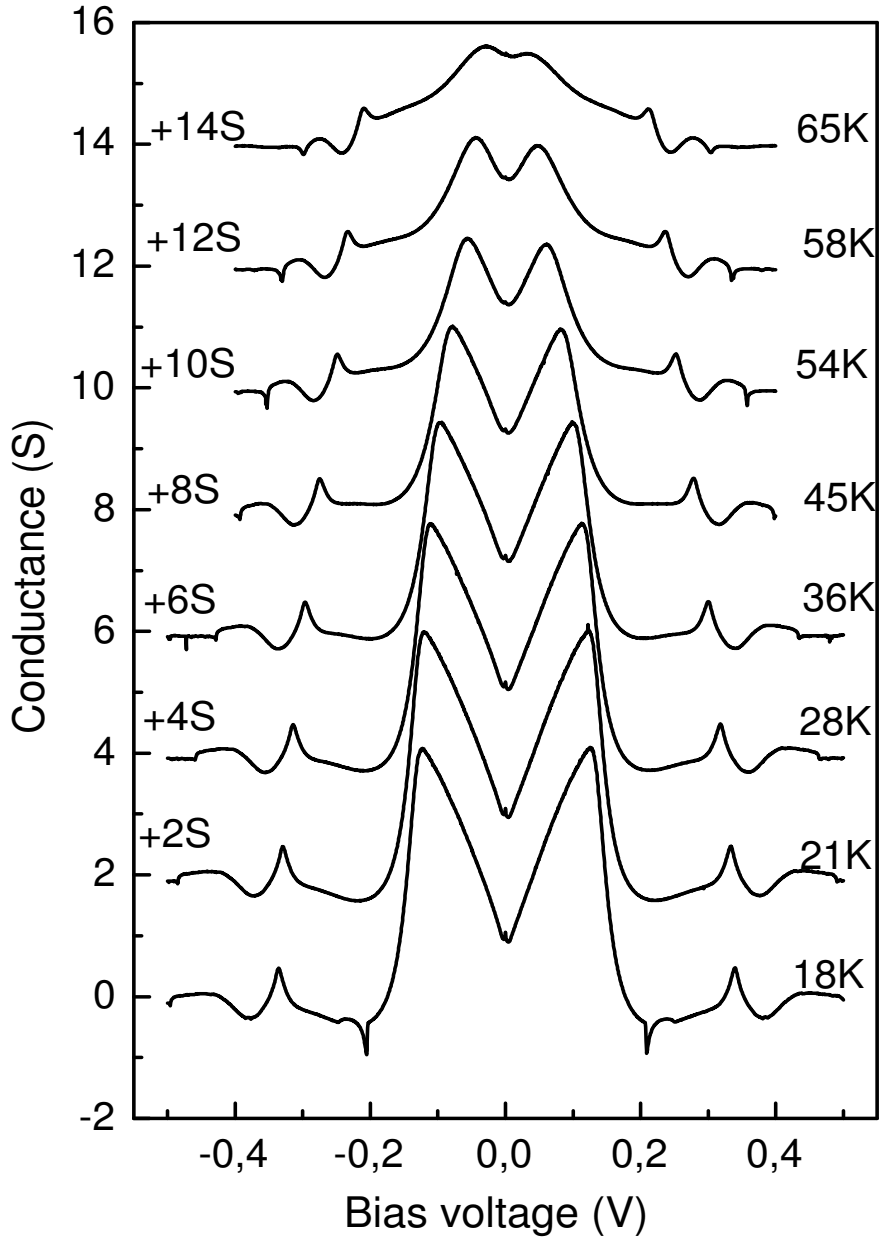

Figure 4.6: *G(V)* dependence of a 50×50 μm^2 mesa of the $YBCO_2/PBCO_{10}$ superlattice. For enhanced voltages the conductance becomes negative; this effect is due to overheating.

In order to minimize the self–heating effect, superlattices with mesas between 16×16 μm^2 and 20×20 μm^2 were prepared. Figure 4.8 shows the (dI/dV)–V curve of a 16×16 μm^2 mesa of a $(YBa_2Cu_3O_{7-x})_4/(PrBa_2Cu_{2.9}Ga_{0.1}O_{7-y})_{16}$ superlattice (sample $YBCO_4/PBCGO_{16}$). The differential conductance at large bias of this sample is positive, and the overheating is considerably reduced. This fact is confirmed by both, the stability of the sample temperature at large voltage and the shape of the current–voltage characteristic where I increases monotonic with V (Fig. 4.8 right scale). This sample, on the other hand, possesses a more insulating and thicker barrier than sample $YBCO_2/PBCO_{10}$. However, the central features of the (dI/dV)–V curve remain unchanged, showing a metallic junction behavior. The samples $YBCO_4/PBCGO_{16}$ and YBCO/PBCGO

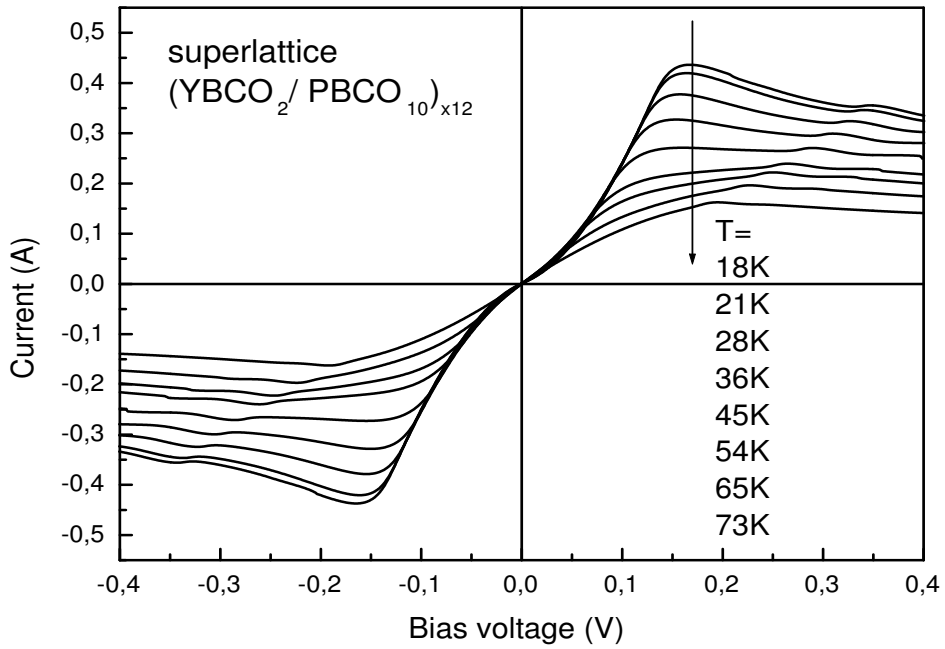

Figure 4.7: Current–voltage characteristic of a $50 \times 50\,\mu m^2$ mesa of the $YBCO_2/PBCO_{10}$ superlattice. As the voltage increases the current decreases due to self–heating.

(20nm)/YBCO–HT (trilayer with 20 nm barrier) of chapter 3 present common characteristics. The differential conductance in the subgap region is larger than the normal conductance and the conductance background is nearly a constant function of the bias voltage. One can assert that the shape of the *G(V)* de-

pendence of the $YBCO_4/PBCGO_{16}$ superlattice shares the main features of the YBCO/PBCGO (20nm)/YBCO–HT trilayer, but multiplied by a certain factor associated with the number of junctions in series; in particular concerning the width of the subgap region and the relative height of the maxima with respect to the background. The voltage value of the maximum in G of the trilayer YBCO/PBCGO (20nm)/YBCO–HT is approx. 2 mV for one contact, whereas for the sample $YBCO_4/PBCGO_{16}$ with 7 contacts in series it is about 45 mV i.e., the value per contact is about 6.4 mV. Moreover, the quotient between the maximum of the differential conductance and the normal conductance of sample YBCO/PBCGO (20nm)/YBCO–HT is about 1.4, whereas for sample $YBCO_4/PBCGO_{16}$ it is approx. 9 which gives a factor 1.3 per contact.

The current–voltage characteristic of sample $YBCO_4/PBCGO_{16}$ shows an excess current (dotted line in Fig. 4.8). This means that the linear part of the I–V curves at high voltages does not coincide with the I–V curve of the normal

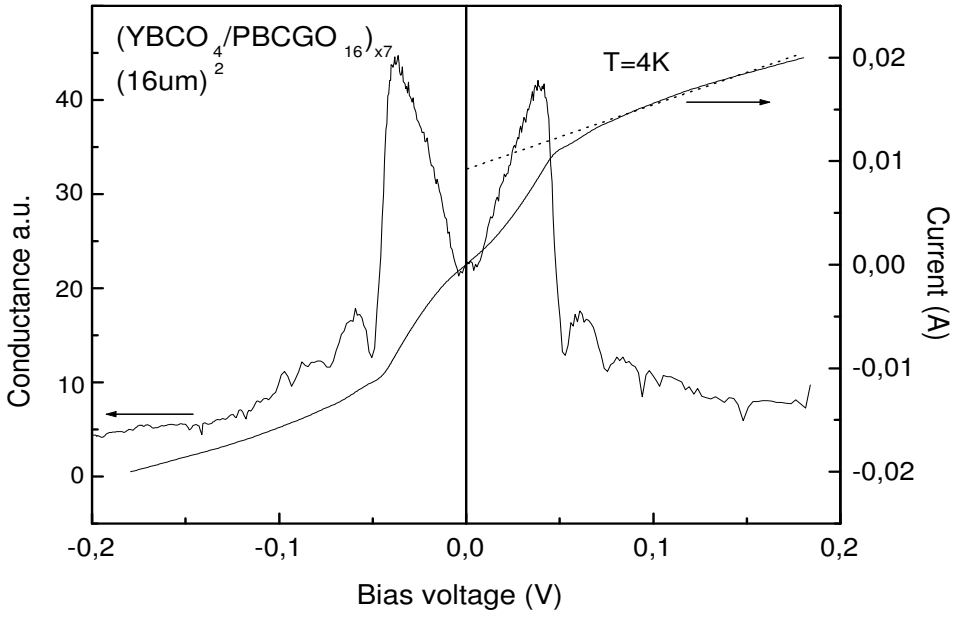

Figure 4.8: *G(V)* dependence of a $16 \times 16\,\mu m^2$ mesa of the $YBCO_4/PBCGO_{16}$ superlattice. The behavior of the differential conductance in the subgap region suggests a *SNS*–type contact. The background conductance is positive but G decreases as the bias increases.

state, but it is displaced vertically by a constant referred to as the excess current I_{exc}. This quantity is also defined as the extrapolation from the linear part of the current–voltage characteristic at large voltage on the current axis. After Bonder *et al.* [23] the excess current can be written as $I_{exc} = (I_{NS} - I_{NN})$ at $eV \gg \Delta$, where I_{NS} is the current between the superconductor and the normal metal and $I_{NN} = V/R_N$, here R_N is the resistance in the normal state. I_{NS} depends on the transmission coefficient $\Omega = 1 + A(eV, Z) - B(eV, Z)$, where $A(eV, Z)$ gives the probability of Andreev reflection and $B(eV, Z)$ of ordinary reflection. Both coefficients depend on the dimensionless barrier strength Z. Bonder *et al.* calculated the dependence of $I_{exc}R_N/\Delta$ upon the barrier strength Z. They found that this quantity falls rapidly with increasing Z. The I–V characteristic of a junction containing barriers with low Z shows an excess current; in other words, the quantity I_{exc} can indicate the type of junction. According to this criterion, the sample $YBCO_4/PBCGO_{16}$ behaves as a superlattice of *SNS* contacts in series.

4.4 Background conductance

The different multilayers prepared at $T_s = 840°C$ showed characteristics that pointed at a metallic junction behavior. The arguments are the appearance of an excess current and the fact that the differential conductance near to zero bias is larger than the conductance in the normal state. However, there exist another criterion which can provide important information about the character of the contacts. This is the shape of the background conductance.
The issue concerning the background conductance was extensively discussed by Th. Becherer [56] in his PhD. work on ramp-type junctions and break-junction of single crystals of $YBa_2Cu_3O_{7-x}$ and $Bi_2Sr_2CaCu_2O_{8+\delta}$. Some models ascribe the behavior of the background to intrinsic properties of the HTSC. Other models are based on the dynamics of the tunnel process. In this section, the most relevant aspects of the representative models relating to the background conductance are compiled. More details can be found in [56] and [113].

The resonanting–valence–bond (RVB) model [114] states that the fact that the conductance at high voltages rises is compatible with the two–dimensional spinon–holon picture in the normal state. Varma *et al.* [115] proposed a phenomenological description based on marginal Fermi–liquid theory, according to which the conductance drops when the bias voltage increases. Another intrinsic model [116] is related to localized states in the CuO_2 planes that result in ex-

tended states. At high energy, these extended states can lose energy due to the excitation of interplanar phonons, i.e. the coupling between two adjacent CuO_2 layers becomes weaker. The high energy regime is thus dominated by localized states and the conductance gets flatter.

Concerning the dynamics of the tunnel process, alternative explanations based upon a density of states effect were proposed [75, 113]. The dependence of the conductance on the bias voltage was suggested a barrier size effect (see chapter 3). As a result of the conventional tunneling theory of a normal *M–I–M* junction, a quadratic dependence of the conductance with voltage appears $G(V) \sim V^2$. The behavior of $G(V)$ dependence of the sample YBCO/PBCGO (20nm)/YBCO–LT is in agreement with this model. Kirtley *et al.* [117] suggested that the linear background is due to inelastic tunneling effects from a broad, flat continuum of states that involves inelastic antiferromagnetic spin–fluctuations scattering.

A transition from metallic to tunneling behavior in Au-$YBa_2Cu_3O_{7-x}$ single crystal point contact junctions as a function of junction resistance was reported by H. Srikanth *et al.* [74]. A change in the *G(V)* dependence was observed not only in the subgap region but also at large voltage. In the point contact regime a metallic tip comes in contact with the superconducting electrode through the barrier; the interface resistance is "low" so that it forms a *SN* junction. An excess of G was observed $(G(0)/G(V \gg \Delta)) > 1$ and the conductance decreased as V increased. As the tip was pulled back, the tunneling regime was reached increasing the interface resistance. Now electrons had to tunnel the barrier, the *G–V* curve raised and gaplike features appeared.

Later, Kirtley [118] explained the change in sign of the conductance background with the contact resistance as the dependence of the dynamics of the inelastic scattering on the interface transmittance. In the low–transmittance tunneling regime, the excitation of a particular inelastic mode of energy $\hbar\omega$ results in an up–step in conductance at a voltage $eV \sim \hbar\omega$. If there is a broad distribution of states, the individual steps add up to a linear conductance increase. In the high–transmittance point–contact regime a particular energy loss mode leads to a step down in conductance at $eV \sim \hbar\omega$, and therefore a broad distribution of states will lead to a linear conductance decrease. Figure 4.9 shows the evolution of the differential conductance with the parameter Z. In the tunnel regime, the background conductance increases linearly. As the junction resistance decreases $(R \sim Z^2)$, the gap broadens and the sign of the background conductance changes.

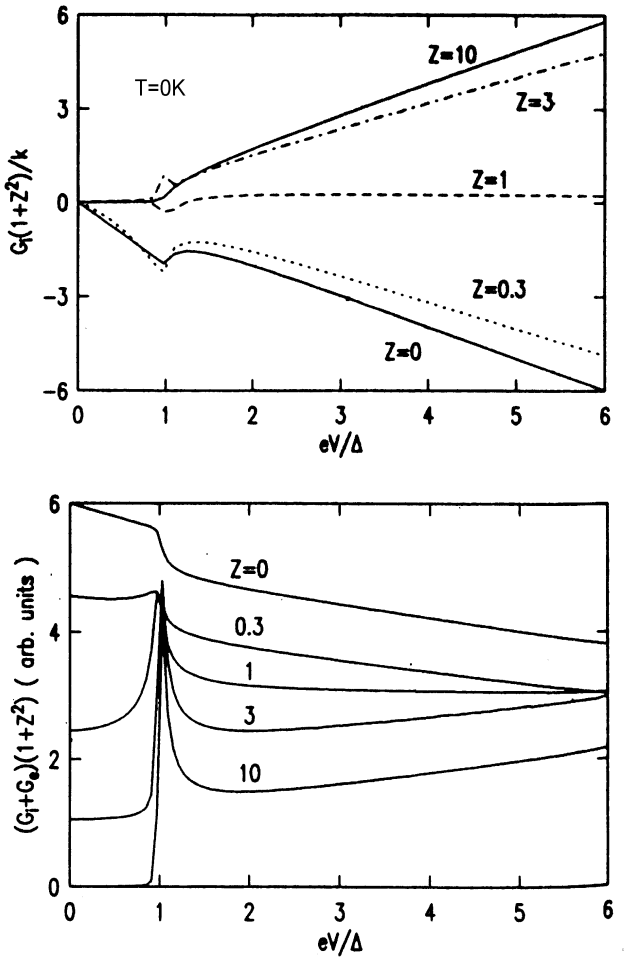

Figure 4.9: Differential conductivity vs. voltage for the elastic tunnel component (top) and the sum of the inelastic and elastic tunnel component (bottom) for different values of Z. Taken from Ref. [118].

4.5 Conductivity measurements of superlattices prepared at $T_s = 760°C$

Following the same scheme presented in chapter 3 for trilayers samples, two sorts of superlattices were prepared: heterostructures fabricated at "high" substrate temperature (section 4.3), and heterostructures fabricated at "low" substrate temperature (this section). In the present section the differential conductance measurements of $YBa_2Cu_3O_{7-x}$ /$PrBa_2Cu_{2.9}Ga_{0.1}O_{7-y}$ superlattices prepared at 760°C are presented. The (dI/dV)–V curves show a remarkable change with respect to the samples prepared at 840°C. This reveals that the behavior of the $YBa_2Cu_3O_{7-x}$ /$PrBa_2Cu_{2.9}Ga_{0.1}O_{7-y}$ contacts is very sensitive to the substrate temperature. Figure 4.10 shows the *G(V)* characteristic of the $(YBa_2Cu_3O_{7-x})_4$ /$(PrBa_2Cu_{2.9}Ga_{0.1}O_{7-y})_{12}$ superlattice for different temperatures. At high bias voltage the normal differential conductance $G_n(V)$ increases nearly linearly with V. In the low voltage regime, the differential conductance displays a rapid decrease as the bias voltage is reduced. On the other hand, the temperature dependence of the differential conductance near to zero bias changes considerably with respect to *G(V)* at large voltage. This suggests the formation of a gap feature close to zero–bias. The main result presented in this section was observed on a $(YBa_2Cu_3O_{7-x})_4$/$(PrBa_2Cu_{2.9}Ga_{0.1}O_{7-y})_5$ superlattice (denoted as sample $YBCO_4$/$PBCGO_5$). It is shown in Fig. 4.11. Two main characteristics are noteworthy

- a well–defined gap structure at low bias
- a nearly linear increase of the differential conductance with bias voltage.

In contrast to the superlattice $YBCO_4$/$PBCGO_{12}$, the *G(V)* dependence exhibits a well–defined gaplike structure at low temperature. The maxima of the differential conductance are localized at approx. 56 mV. This is the result of the summation of a stack of 14 bilayers. The total gap corresponds to the number of bilayers multiplied by twice the individual energy gap. The calculation of the energy gap for each junction results in $\Delta_c \approx 2.0$ meV. This value is smaller than the values reported in the literature. However, it agrees nearly with the gap value estimated for the trilayer YBCO/PBCGO (20nm)/YBCO–HT in chapter 3 (see table 4.1). The maxima in the differential conductance move to lower voltage as the temperature increases. At approx. 36 K the gap feature practically vanishes. The temperature dependence of the gaplike structure obtained from the

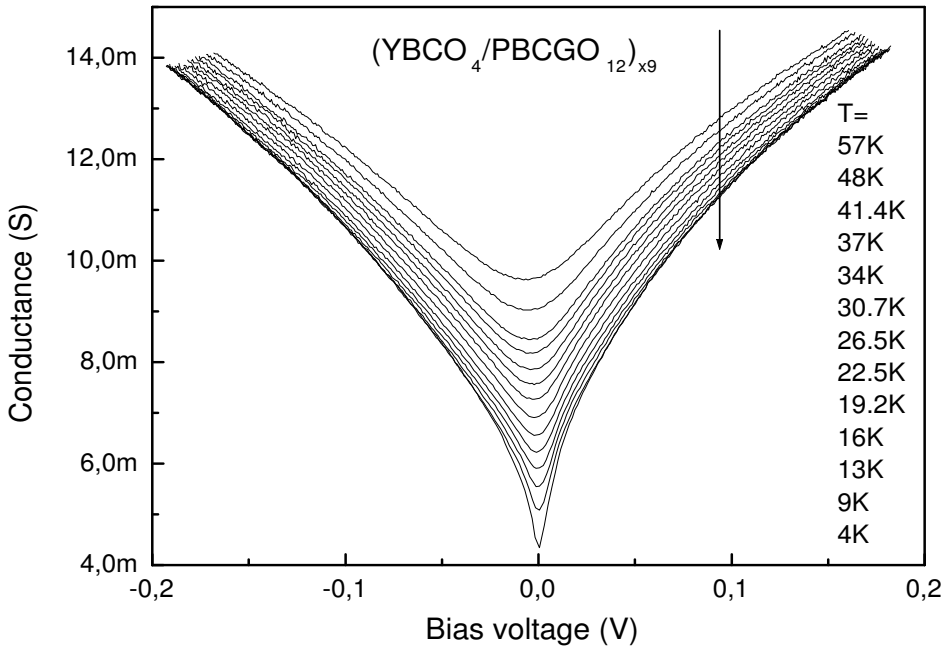

Figure 4.10: Tunneling conductance as a function of bias voltage of a $(YBa_2Cu_3O_{7-x})_4/(PrBa_2Cu_{2.9}Ga_{0.1}O_{7-y})_{12}$ superlattice. *G(V)* increases with *V*, and $G(0) < G_n(V)$.

conductance–voltage characteristic of the sample $YBCO_4/PBCGO_5$ (Fig. 4.11) is displayed in Fig. 4.12. The peak voltage position variation with respect to the temperature shows between 4 K and 20 K a reasonable good agreement with the BCS prediction for the gap versus temperature dependence. However, there is a deviation between 23 K and 36 K. At higher temperatures a zero bias conductance peak appears. The origin of such a peak is dubious. However, this phenomenon can be attributed to either some transition from tunneling to a metallic junction characteristic where either Andreev scattering dominates or magnetic scattering between quasiparticles and magnetic moments in the barrier (see section 3.9). At low temperatures a tiny feature is visible in the subgap region at approx. 25 mV (Fig. 4.13). As the temperature increases this feature disappears rapidly. The origin of such a feature will be discussed in the next section.

The sample $YBCO_4/PBCGO_5$ shows another interesting characteristic. The value of the normal conductance remains roughly unchanged with temperature

Junction	Δ(meV)	ref.
Y–123/$SrAlTaO_6$/Y-123	4.25	[61]
Y–123/CeO_2/Y–123	4 – 6	[119]
Y–123/Pr–123/Y–123	5.3	[103]
Y–123/Pr–123/Y–123	4.5	[11]

Table 4.1: Comparison of the c–axis energy gap values of $YBa_2Cu_3O_{7-x}$from literature.

and increases proportionally to the bias voltage i.e., the background differential conductance exhibits a "V" form. Nevertheless its shape is slightly asymmetric with respect to zero bias, which is likely due to barrier asymmetric effect.

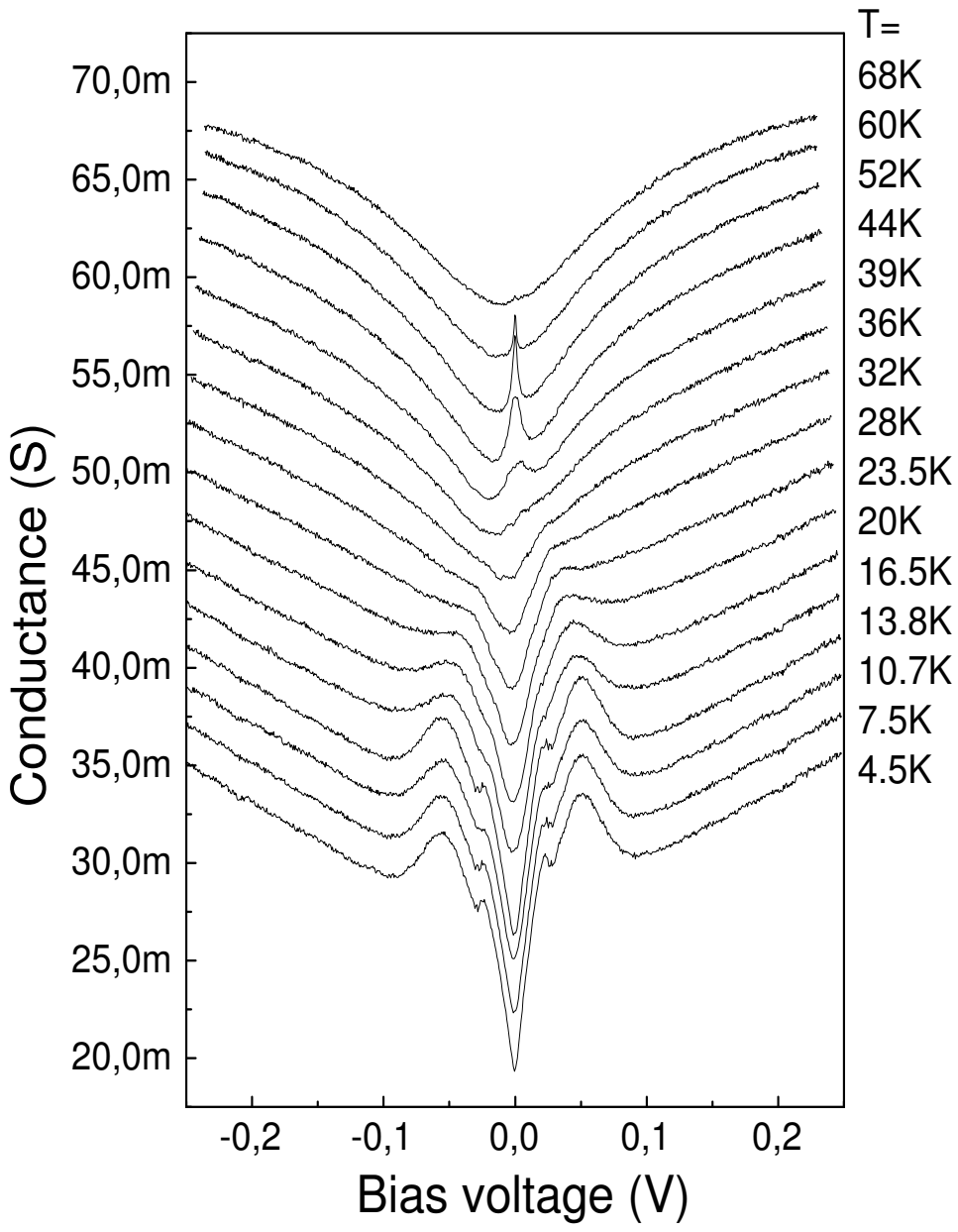

Figure 4.11: Tunneling conductance of the $(YBa_2Cu_3O_{7-x})_4/(PrBa_2Cu_{2.9}Ga_{0.1}O_{7-y})_5$ superlattice for various temperatures. The *G(V)* curve exhibits a gaplike structure at low voltage, at high voltage the differential conductance increases linearly with V. The different curves are vertically displaced by 2 mS for clarity purposes.

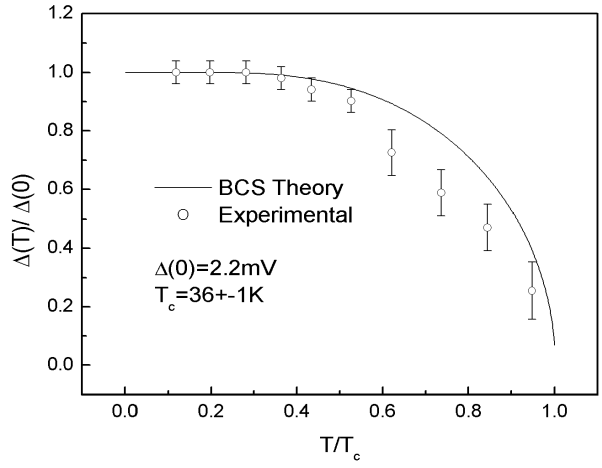

Figure 4.12: Temperature dependence of the peak voltage together with the BCS gap dependence.

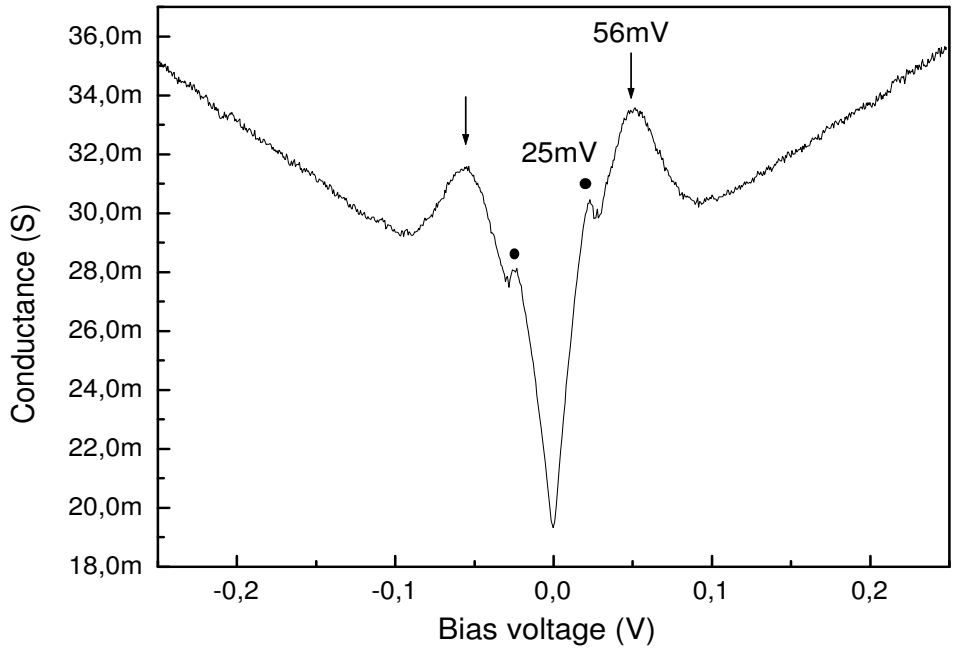

Figure 4.13: The peak–to–peak voltage between the maxima is approx. 120 mV which corresponds to about 2 mV per junction. The features at approx. 25 mV (•) suggests the existence of an additional gap.

4.6 Discussion

The tunneling conductance measurements of trilayers (chapter 3) and superlattices (chapter 4) show that the deposition temperature has a sensitive influence on the *c*–axis electrical properties of $YBa_2Cu_3O_{7-x}$ /$PrBa_2Cu_3O_{7-y}$ and $YBa_2Cu_3O_{7-x}$/$PrBa_2Cu_{2.9}Ga_{0.1}O_{7-y}$ heterostructures. A transition from metallic to tunnel junction behavior is observed when lowering the substrate temperature from 840°C to 760°C. High substrate temperatures favor the *c*–axis growth, morphology and homogeneity but they can also promote some reaction between the superconducting slabs and the insulating spacers in the interface of HTSCs multilayers. An interdiffusion between $YBa_2Cu_3O_{7-x}$ and $PrBa_2Cu_3O_{7-y}$ can lead to the formation of a third material at the boundary with intermediate electrical properties. The presence of such an intermediate layers will modify the spatial variation of the order parameter. If this region has a metallic character, the order parameter will decay over a certain distance in the "metallic" region due to the proximity effect (Fig. 4.14a). This hypothesis could explain the metallic junction behavior of the (dI/dV)–V characteristics and excess current of the multilayers prepared at 840°C. On the other hand, lower substrate temperatures should reduce the interdiffusion effect at the boundary. In consequence, the $YBa_2Cu_3O_{7-x}$ /$PrBa_2Cu_3O_{7-y}$ interfaces are sharp and the order parameter is discontinuous like in an actual *S/I* interface. It is to be expected that the junction resistance rises by lowering the substrate temperature from 840°C to 760°C.

The occurrence of a feature within the subgap region of the sample $YBCO_4$/ $PBCGO_5$ at approx. 25 mV suggests the existence of an additional gap, weak in intensity, that belongs to the outermost region of the superconducting slab. A simple picture of this situation is shown in Fig. 4.14b. Close to the boundary the superconducting character of the $YBa_2Cu_3O_{7-x}$ electrode deteriorates. This narrow region acts like a "weak" superconductor with an order parameter value $|\Delta_2|$ less than $|\Delta_1|$ in bulk and critical temperature lower than the bulk $YBa_2Cu_3O_{7-x}$ T_c. This situation would correspond to a *S/S'/I*–type interface. The validity of this hypothesis of the metallic and tunneling junction character depending on the substrate temperature becomes apparent by comparing the value of the differential conductance of different heterostructures in the normal state (see Table 4.2). In chapter 3, the *G(V)* dependences of two trilayers with the same barrier thickness of 20 nm but prepared at different substrate temperatures

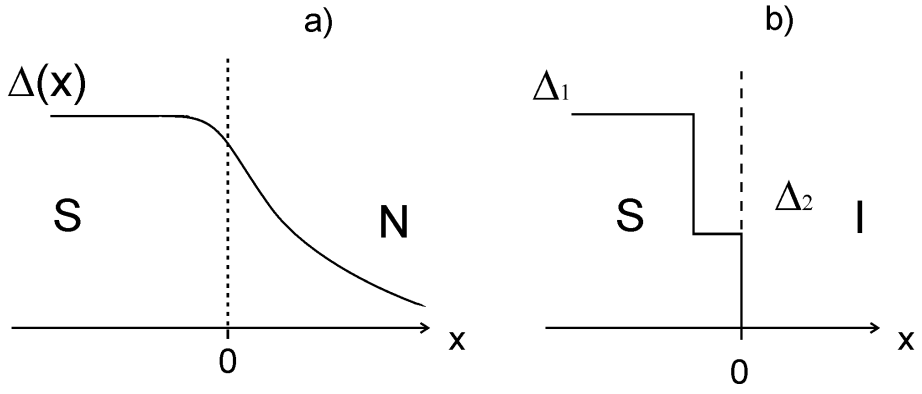

Figure 4.14: Order parameter profile at the interface of the a) low resistive case (T_s = 840°C) and b) high resistive case (T_s = 760°C). A superconducting region close to the interface behaves as a "weak" superconductor with Δ_2 smaller than $\Delta_1(bulk)$.

were presented. The value of the normal differential conductance of the sample

Heterostructure		T_s		*G(V)* at T = 4 K	
trilayer†	superlattice	840°C	760°C	G(40 mV)	G(200 mV)
–HT		√		550 mS	
–LT			√	30 mS	
	$YBCO_4/PBCGO_{16}$	√			100 mS
	$YBCO_4/PBCGO_{12}$		√		14 mS
	$YBCO_4/PBCGO_5$		√		33 mS

Table 4.2: Comparison of the normal conductance for different heterostructures. (†)Trilayer YBCO/ PBCGO (20 nm)/YBCO–

YBCO/PBCGO (20nm)/YBCO–HT (T_s = 840°C) at 40 mV bias is about twenty times as large as the conductance of the sample YBCO/PBCGO (20nm)/YBCO–LT (T_s = 760°C) at the same bias. A similar situation occurs for the superlattices $YBCO_4/PBCGO_{16}$ (T_s = 840°C) and $YBCO_4/PBCGO_{12}$ (T_s = 760°C). Despite of the fact that the thickness of the barrier (18.7 nm and 14 nm, respectively) and the number of contacts in series (7 and 8, respectively) is comparable, the normal conductance at 200 mV of sample $YBCO_4/PBCGO_{16}$ is approx. an order of magnitude larger than for $YBCO_4/PBCGO_{12}$. In other words, the higher the substrate temperature the lower the junction resistance. The value of the normal conductance at 200 mV bias for sample $YBCO_4/PBCGO_5$ (barrier thickness 6 nm

and 14 bilayers) is nearly twice the value of the sample $YBCO_4/PBCGO_{12}$ (barrier thickness 14 nm and 8 bilayers) at the same bias i.e., the normal conductance increases as the barrier thickness decreases. This result supports the normal conductance criterion to identify the nature of the junction. The fact that junctions with "low" resistance exhibit BTK–type *G(V)* dependences, whereas junctions with "high" resistance show tunneling conductance behavior agrees with previous results, for example in Au/ $YBa_2Cu_3O_{7-x}$ single crystal point contacts (Srikanth *et al.* [74]) where a continuous transition from microshorts *S-N* to tunneling *S-I-N* was observed by adjusting the contact pressure in the point contact junction. At the lowest junction resistance an excess conductance was detected. By increasing the junction resistance, the zero–bias conductance dropped and gaplike features appeared in the *G(V)* curve.

The tunneling conductance measurements presented in this work can be explained with the inelastic transport model proposed by Kirtley [118]. For low–resistance–contact samples (YBCO/PBCGO (20nm)/YBCO–HT trilayer and $YBCO_4/PBCGO_{16}$ superlattice), the gap feature is not completely developed and the conductance background acquires a "Λ" form. On the contrary, for the samples YBCO/PBCGO (20nm)/YBCO–LT, $YBCO_4/PBCGO_{12}$ and $YBCO_4/PBCGO_5$ with "high"– resistance –contacts a gap structure is apparent especially for sample $YBCO_4/PBCGO_5$. Additionally, the differential conductance at high bias increases with the applied voltage showing a "V"–shape background. The zero–bias conductance displays a finite value different from zero (with the exception of the sample YBCO/PBCGO (20nm)/YBCO–LT). This can be due to the presence of states at the Fermi level inducing spin-flip scattering that competes with the appearance of superconductivity (see section 3.9).

Chapter 5

Optical properties

5.1 Two–dimensional antiferromagnets

The parent compounds of the cuprates superconductors can be doped by either substituting different elements in the reservoir or varying the oxygen concentration. The effect of doping in these materials is the introduction of additional charge carriers into the CuO_2 planes, which alters profoundly their electronic properties. The phase diagram of the cuprate superconductors is represented in Fig. 5.1, here the temperature dependence on the hole concentration per CuO_2 plane is sketched. The undoped case (hole concentration = 0) correspond to the so–called half–filled Hubbard antiferromagnetic insulator of the charge–transfer type that has a fundamental optical energy gap Δ of a few eV between O $2p$ and Cu $3d$ bands [120]. Due to the large on–site Coulomb repulsion energy, the Cu $3d_{x^2-y^2}$ orbital is split into two Hubbard bands.

The antiferromagnetic state results from the fact that every spin at the Cu^{2+} site is anti–parallel aligned to each of its four closest Cu neighbors, therefore a CuO_2 plane forms a two–dimensional antiferromagnet (Fig. 5.2). Such a system is equivalent to the spin–$\frac{1}{2}$ antiferromagnetic Heisenberg model of a square lattice[1], which is described by a hamiltonian of the form

$$H_J = J \sum_{\langle i,j \rangle} \mathbf{S_i} \cdot \mathbf{S_j}. \tag{5.1}$$

Here $\mathbf{S_i}$ is the spin operator and $J = 4t^2/U$ is the antiferromagnetic exchange coupling constant, where U is the Coulomb on–site repulsion and t is the hopping

[1]The CuO_2 plane is nearly a square lattice, however, the cuprates La_2CO_4 and $YBa_2Cu_3O_6$ are tetragonal, whereas $YBa_2Cu_3O_{7-x}$ is orthorombic.

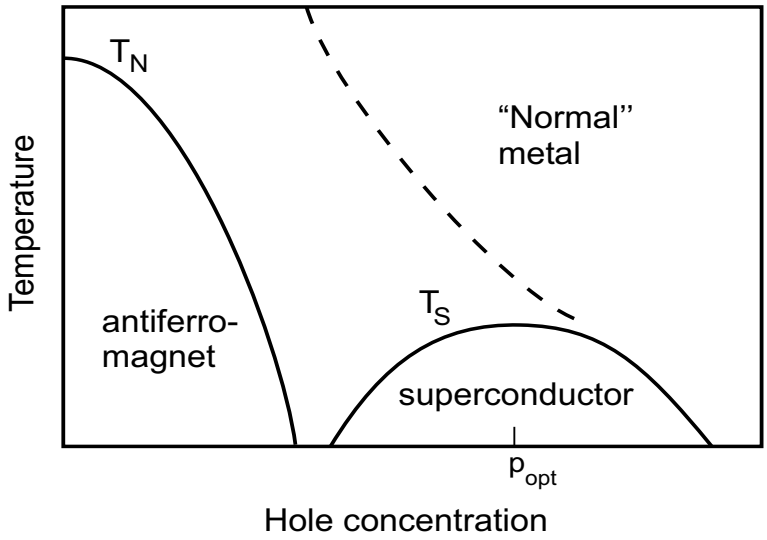

Figure 5.1: Phase diagram of p–type cuprate superconductors showing the antiferromagnetic, superconducting and "normal" metal region. From Ref. [121].

matrix element. The Heisenberg model (5.1) is assumed to describe antiferromagnetic undoped insulators like La_2CuO_4, the oxygen deficient $YBa_2Cu_3O_6$ and other undoped copper oxides.

By increasing the effective carrier concentration, the Néel temperature T_N decreases i.e., the increase of the number of holes in the CuO_2 plane of the p–type HTSC's starts to destroy the antiferromagnetic ordering and a metallic state appears. A further increase in the hole concentration causes the formation of the superconducting phase. One finds a maximal T_s at optimal hole concentration of about 20% per cuprate plane.

A doped antiferromagnet is a system of interacting spins and mobile holes, its description requires the Heisenberg model of antiferromagnetism and a kinematic part that allows hopping of holes in the CuO_2 planes, such a hamiltonian is the so–called t–J model [123]

$$H = -t \sum_{\langle i,j\rangle,\sigma} (c^{\dagger}_{i,\sigma} c_{j,\sigma} + H.c.) + J \sum_{\langle i,j\rangle} \mathbf{S_i} \cdot \mathbf{S_j}. \tag{5.2}$$

$c^{\dagger}_{i,\sigma}(c_{i,\sigma})$ creates (annihilates) a hole on the site i with spin σ, $\langle i,j\rangle$ identifies nearest–neighbor pairs, and t is the hopping matrix element.

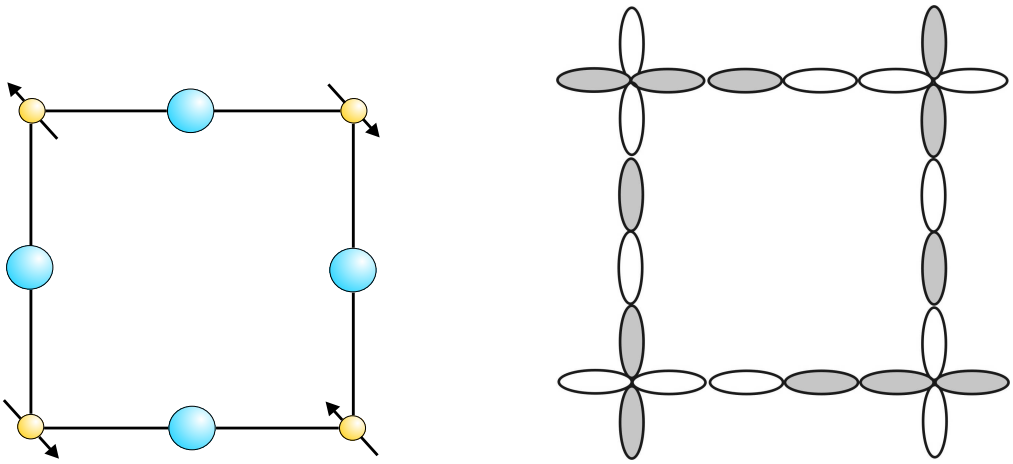

Figure 5.2: CuO_2 plane, copper atoms are situated at the corners and oxygen atoms in the middle of each side (left). Illustration of the $d_{x^2-y^2}$ and $2p$ orbitals of Cu and O respectively for nonbonding hybridized wave function (right). Taken from Ref. [122].

5.2 Two magnon interaction

The interaction between light and two dimensional antiferromagnetic systems can lead to the interaction between magnons. The basic idea is that two magnons are created simultaneously by inelastic light scattering without changing their components of the spin along the magnetization axis, since the magnons are close to each other in the real space they interact strongly and produce observable effects. A theory of magnon–magnon interaction was proposed by Elliott *et al.* [124], this theory was successfully applied to two dimensional antiferromagnetic systems like Rb_2MnF_4, where the predicted lineshape for two–magnon Raman scattering was observed [125].

Concerning the high temperature superconductors, light scattering studies have concentrated on phonons (low frequency Raman scattering with energies[2] $<$1000 cm^{-1}) [126,127] and magnetic fluctuations. Inelastic light scattering spectra due to spin–pair excitations in single crystal of $YBa_2Cu_3O_{6+x}$ for several values of x in the range from 0 to 0.9 were investigated by Lyons *et al.* [128].

[2]Conversion table for energy units.

$$\begin{aligned} 1eV &\equiv 2.41796 \times 10^{14}\,\mathrm{Hz} \\ &\equiv 8065.5\,\mathrm{cm}^{-1} \\ &\equiv 11604\,\mathrm{K}. \end{aligned}$$

They observed that the energies of these spin–pairs excitations, as well as the spectral line shape depend strongly on the oxygen content x. The insulating sample (x = 0) showed a well-developed peak at 2600 cm^{-1}, the superconducting sample ($x = 0.6$) with $T_c = 60$ K showed a peak at the same energy with small intensity but broadened whereas the sample with $x = 0.9$ and $T_c = 88$ K exhibited no peak. Inelastic light scattering studies on La_2CuO_4 showed a high frequency peak at 3100 cm^{-1} [130], the origin of such excitation was identified with the scattering of pairs of magnons with opposite momenta. An increase of the hole doping reduces the size of the antiferromagnetic domains on the crystal causing a damping of the two–magnon peak. Moreover, the superexchange in the cuprates has been identified as a three–step process involving an intermediate state. First, the oxygen O $2p$ orbital level over the charge–transfer gap Δ_{CT}. Second, a spin flips with the nearest neighbor occurs. Third, the electron with the flipped spin relaxes back to the initial site emitting a photon [129].

5.3 High frequency Raman scattering

The evolution of the two–magnon spectra in $Y_xPr_{1-x}Ba_3Cu_{2.92}Al_{0.08}O_7$ single crystals in dependence on x were measured by Rübhausen *et al.* [131]. This study shows a scan in the phase diagram (Fig. 5.1) from antiferromagnet to superconductor. The undoped case (x = 0) exhibits a strong two–magnon peak around 2300 cm^{-1}. The samples with a Y content of 0.3 and 0.7 ($T_c = 36$ K) show a decrease in the peak intensity but broadened and shift towards lower energies. Increasing the Y doping further up to x = 1, results in a continuous decrease of the scattering intensity and the peak shifted down to 1900 cm^{-1}. This set of measurement shows that the two–magnon excitation exist for all underdoped samples even for the sample with Y = 1 ($T_c = 86$ K). From the phase diagram (inset in Fig. 5.3) one can suggest a competition with doping of two order parameters, one belonging to the antiferromagnetic ordering and the another to the superconducting state.
An interesting scenario to study the interaction of these order parameters constitutes for example a superlattice system of antiferromagnetic and superconducting blocks. Such a system offers the possibility to tune the strength of each order parameter only by changing the thickness of the corresponding layer.

The results of Raman scattering presented here were obtained by D. Budelmann in the Institut für Angewandte Physik at the University of Hamburg

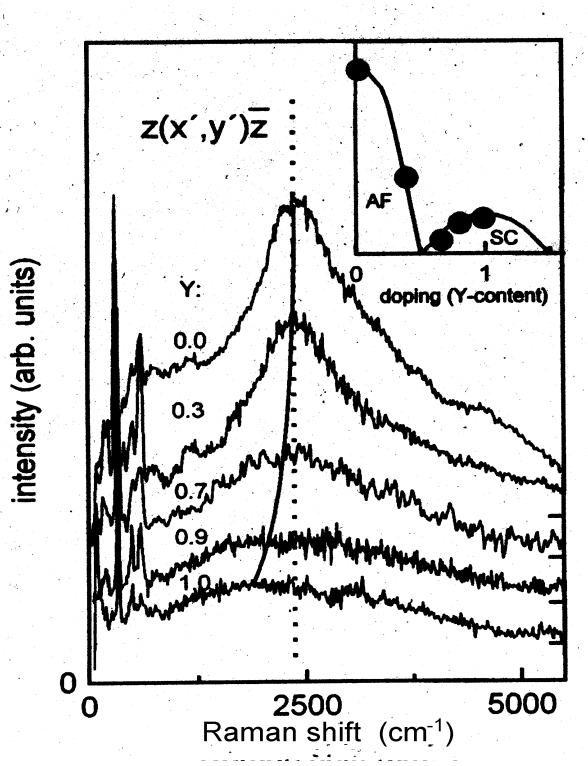

Figure 5.3: Doping dependence of the Raman spectra of $Y_xPr_{1-x}Ba_3Cu_{2.92}$ $Al_{0.08}O_7$ single crystals taken at a temperature of 14 K. Taken from Ref. [131].

[132, 133]. $(YBa_2Cu_3O_{7-x})_n/(PrBa_2Cu_3O_{7-y})_m$ superlattices with $n = 4$ and $m = 6, 9$ and 12 unit cells were analyzed by Raman spectroscopy (details of the experimental setup see Ref. [133]). The (4:6), (4:9) and (4:12) (in the following denoted as $YBCO_4/PBCO_6$, $YBCO_4/PBCO_9$ and $YBCO_4/PBCO_{12}$ respectively) samples were prepared as already described in chapter 2. Figure 5.4a shows the temperature dependence of the two–magnon excitation of the insulating $PrBa_2Cu_3O_{7-y}$ reference sample from room temperature down to 20 K. The signature of the spin–pair–excitation was observed around 2200 cm^{-1}. As the temperature decreases, the two–magnon peak grows continuously and becomes sharper. At low temperature a shoulder appears at high energies likely due to higher order processes. Figure 5.4b displays the Raman spectra of the superlattice $YBCO_4/PBCO_6$ at the same temperature as in Fig. 5.4a. Above T_c the shape of the two–magnon peak resembles the reference sample. Below T_c the $YBa_2Cu_3O_{7-x}$ slabs enter in the superconducting state, and their contribution to the Raman signal is negligible, the observed peak comes from the

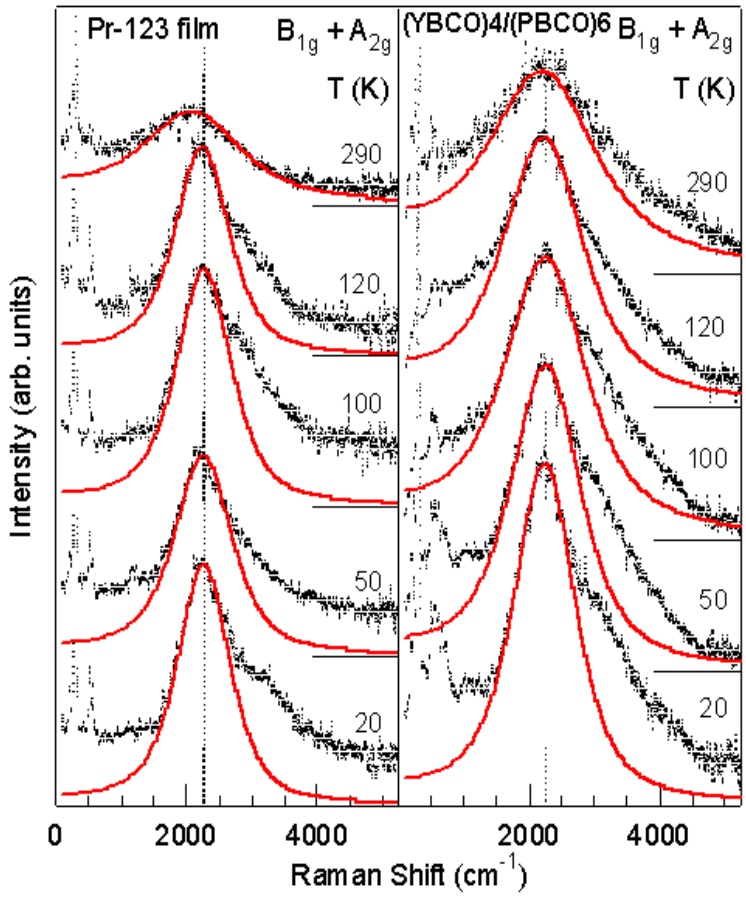

a) b)

Figure 5.4: Raman spectra of $PrBa_2Cu_3O_{7-y}$ (left) and a $YBCO_4/PBCO_6$ superlattice at different temperatures (right).

$PrBa_2Cu_3O_{7-y}$ spacers [131]. However, a sharpening of the two-magnon peak is observed. The measurements of the two–magnon excitation of the superlattices $YBCO_4/PBCO_{12}$, $YBCO_4/PBCO_9$ and $YBCO_4/PBCO_6$ at 20 K show a continuously decrease of the peak width with the decrease of the $PrBa_2Cu_3O_{7-y}$ thickness layer, it means that the life time of the two–magnon excitation is enhanced due to loss of decay channel in the superconducting phase.

The spin–pair–excitation peak was fitted using the extended Fleury–Loudon model based on the Heisenberg antiferromagnet. From this calculation, one can derive the values for the superexchange energy J from the resonance frequency and the damping Γ of the two magnon peaks from the peak width. The physical meaning of Γ is the scattering of a magnon accomplished with the absorption or emission of a photon. Figure 5.5a shows the comparison of the magnon damping

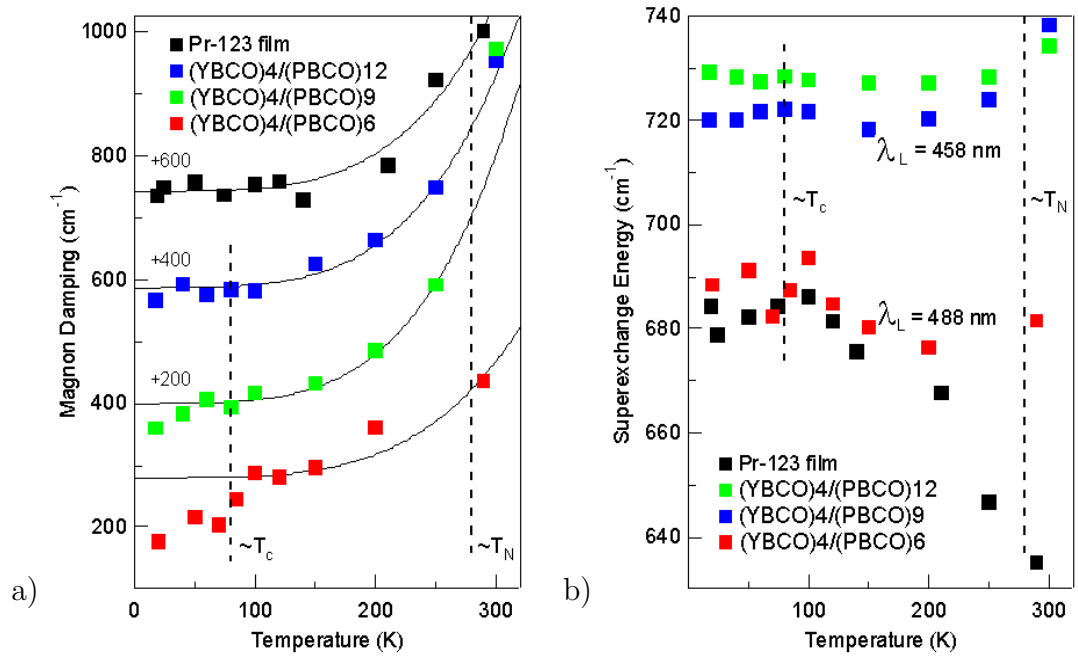

Figure 5.5: Temperature–dependence damping for all samples, superexchange energy for all samples.

Γ between the superlattices $YBCO_4/PBCO_6$, $YBCO_4/PBCO_9$, $YBCO_4/PBCO_{12}$ and the reference $PrBa_2Cu_3O_{7-y}$ film. The width of the two–magnon peak for all samples decreases strongly between 300 K and 200 K. Below 150 K the magnon damping of the $PrBa_2Cu_3O_{7-y}$ sample seem to be constant with a values around 170 cm^{-1}. The samples $YBCO_4/PBCO_{12}$ and $YBCO_4/PBCO_9$ exhibit similar behavior as the sample $PrBa_2Cu_3O_{7-y}$ with Γ saturating to values of around 190 cm^{-1} and 180 cm^{-1} respectively, whereas in sample $YBCO_4/PBCO_6$ at 150 K it reaches values of 300 cm^{-1} and below T_c, Γ drops to the value of 190 cm^{-1}. Figure 5.5b shows the calculated value of the superexchange constant $J = 4t^2/U$, where t is a hopping matrix element between two copper sites, which depends strongly on the Cu–Cu distance and U is the Coulomb on–site repulsion. The superexchange energy of the sample $PrBa_2Cu_3O_{7-y}$ increases with decreasing temperature. This is due to the lattice contraction, which increases t. Below 100 K, J saturates to values of about 680 cm^{-1}, this value is consistent with the literature [131]. On the other hand, the temperature dependence of the superexchange energy of all superlattices is nearly constant. This is likely due to a compensation of the different thermal expansion coefficient of $YBa_2Cu_3O_{7-x}$ and $PrBa_2Cu_3O_{7-y}$. At low temperature, the sample

with large modulation ($YBCO_4/PBCO_9$ and $YBCO_4/PBCO_{12}$) exhibits large superexchange J. This value is close to the single crystal measurement ($J \approx 720$ cm^{-1}) whereas for the sample $YBCO_4/PBCO_6$ has a value of 690 cm^{-1} very close to the value of the sample $PrBa_2Cu_3O_{7-y}$. This behavior can indicate a reduction of epitaxial stress for increasing $PrBa_2Cu_3O_{7-y}$ layer thickness in superlattices. The superconductivity–induced changes of the two–magnon excitation results in an enhancement of its life time, that depends on the thickness of the $PrBa_2Cu_3O_{7-y}$ layers. This observation reveals a strong interplay between superconductivity and magnetism. The values of the superexchange energy for all samples is consistent with the literature.

Chapter 6

Summary

In this work, the c–axis transport properties perpendicular to the CuO_2 planes depending on the substrate temperature during deposition of $(YBa_2Cu_3O_{7-x})_n$ /$(PrBa_2Cu_3O_{7-y})_m$ and $(YBa_2Cu_3O_{7-x})_n$ /$(PrBa_2Cu_{2.9}Ga_{0.1}O_{7-y})_m$ superlattices and $YBa_2Cu_3O_{7-x}$/$PrBa_2Cu_{2.9}Ga_{0.1}O_{7-y}$/$YBa_2Cu_3O_{7-x}$ trilayers were studied. The first part of this work concentrates on improving the crystalline quality of the heterostructures. With this purpose $SrTiO_3$ substrates were subjected to a thermal treatment at 900°C in oxygen atmosphere in order to regrowth and smooth their surfaces. Subsequently to prevent substrate induced strain in the superlattice a 50 nm $YBa_2Cu_3O_{7-x}$ thin film was deposited firstly as buffer layer before the multilayers growth starts.

The x-ray diffraction spectra of all multilayers show perfect c-axis orientation and the Full Width at Half Maximum (FWHM) of the rocking curve of the (005) reflexion was typically $\Delta\omega \approx 0.5°$. The number, position and sharpness of the satellite peaks of the (00ℓ) reflexions reveal excellent crystallographic quality of the superlattices. Low angle spectra were analyzed with the SUPREX refinement program, that allows one to estimate not only the superlattice modulation but also parameter related to disorder. Typical parameters in our samples were a roughnesses less than three tenths a unit cell, interdiffusion of 5% and step disorder between 5% and 10%.

In order to study the c-axis transport properties all multilayers were patterned into mesa structures between $(16\ \mu m)^2$ and $(50\ \mu m)^2$ size and 150 nm height using a combination of photolithography and ion milling techniques. Each mesa was embedded in photoresist that was used as electrical insulator, thereafter using photolithography a window was opened on the top on it with a size smaller than

the mesa area for avoiding short circuits. In order to improve this task a mask aligner was built which allows an alignment accuracy less than 5 μm, afterward a 150 nm gold layer was deposited. The junction fabrication was finished by patterning the gold into contact leads. Each mesa structure was contacted at the bottom via basis electrode and on the top with gold bonding pads. Unfortunately a four point measurement was not possible due the small mesa size. The contact resistance between gold and structure takes values between $0.5\times10^{-4}\,\Omega\mathrm{cm}^2$ and $2\times10^{-4}\,\Omega\mathrm{cm}^2$.

The third and main part of this work focuses on the c–axis transport properties in HTSC multilayers depending on the deposition temperature. The differential conductivity of samples with $(50\ \mu\mathrm{m})^2$ size mesas was considerably affected by overheating effects specially at low temperature. Because this effect is proportional to the mesa area, a notable reduction of the overheating was achieved with mesas of size between $(16\ \mu\mathrm{m})^2$ and $(20\ \mu\mathrm{m})^2$. In order to study the influence of the deposition temperature on the barrier and the interface, a series of multilayers at the substrate temperature of 840°C and 760°C were prepared and measured. Transport measurement of trilayers with 20 nm $PrBa_2Cu_{2.9}Ga_{0.1}O_{7-y}$ barrier prepared at 840°C showed a metallic junction behavior which was characterized with an excess of conductivity at bias voltage lower than the gap energy. This observation was unexpected due to the nominally insulating character of the $PrBa_2Cu_{2.9}Ga_{0.1}O_{7-y}$ barrier. The G–V curve of this sample was analyzed under the BTK theory of superconductor–normal metal junctions. The calculated barrier strength parameter was 0.45 which corresponds to a high barrier transparency. A possible reason can be a reaction of the materials at the interface which can be regarded as third material with intermediate properties. This material should allow some permeability to the order parameter into the barrier so that the conductance at zero bias increases. The current–voltage characteristic of this sample was similar to the I–V curve predicted by the RCSJ model with a critical current of $6.2\times10^2\ \mathrm{Acm}^{-2}$, however, the magnetic field dependence of the critical current did not show the behavior expected of a Josephson–like junction.

With the aim of reducing possible reactions at the interface the substrate temperature was lowered to 760°C. The differential conductance of trilayers with 20 nm $PrBa_2Cu_{2.9}Ga_{0.1}O_{7-y}$ barriers prepared at this temperature shows in contrast to samples prepared at 840°C tunnel–like junction behavior. At large voltages the differential conductance is proportional to the bias voltage but nearly independent of temperature. At low voltage regime below 20 mV the differential

conductance reduces as the temperature decreases. However, a zero bias conductance peak appears that hinders a gap development. The presence of a peak can suggest a supercurrent at zero bias, however, the current–voltage characteristic did not show any voltage region where a supercurrent was detected.

The temperature and voltage dependence of ΔG was analyzed with the Anderson –Appelbaum model, it was found that the excess of conductance at zero bias decreases linearly with $-\ln(T)$ between 10 K and 50 K. On the other hand, a linear dependence between ΔG and $-\ln|V|$ in a narrow region between 2 mV and 5 mV at low temperatures was observed. These features support a magnetic origin of the zero bias conductance peak which can be due to the scattering between quasiparticles and permanent magnetic moments. If the antiferromagnetic order of either copper atoms in the CuO_2 planes or Pr ions are altered for example via Ga doping or from incompleted $PrBa_2Cu_{2.9}Ga_{0.1}O_{7-y}$ unit cells it is likely to have some paramagnetic impurities in the barrier or at the surface. The conductance background of the trilayer with 20 nm $PrBa_2Cu_{2.9}Ga_{0.1}O_{7-y}$ barrier (produced at 760°C) was studied using the Simmons model of a normal metal–insulator–normal metal junction, from this analysis a barrier height of 6.4 V was calculated.

The differential conductance of superlattices prepared at 840°C and 760°C behave in the similar fashion as trilayers prepared at the respectively temperatures. The differential conductance of the samples prepared at 840°C shows a BTK tunnel junction i.e., with an excess conductance in the subgap region. The overshoots in the differential conductance of the sample $(YBa_2Cu_3O_{7-x})_2/(PrBa_2Cu_3O_{7-y})_{10}$ represent the increase of the quasiparticle density of states at the sum of twelve $YBa_2Cu_3O_{7-x}$ superconductive gaps. The metallic character of the barrier was confirmed by the observation of an excess current in the I–V characteristics.

The main results were observed with superlattices prepared at 760°C. The sample $(YBa_2Cu_3O_{7-x})_4/(PrBa_2Cu_{2.9}Ga_{0.1}O_{7-y})_{12}$ shows a linear dependence between voltage and the differential conductance. For low bias voltage the $G(V)$ depends strongly on the temperature, however, a gaplike structure was not observed. The shape of the conductance background of this superlattice is similar to the shape of the trilayer produced at 760°C and agrees very well with Kirtley's theory for high–resistance contacts. According to this theory the linear increase of the differential conductance with the bias voltage is attributed to inelastic tunnel processes. The main result was obtained with the superlattice $(YBa_2Cu_3O_{7-x})_4/(PrBa_2Cu_{2.9}Ga_{0.1}O_{7-y})_5$, the differential conductance exhibits

a strong dependence on voltage. In the high bias region the differential conductance is proportional to the voltage, whereas at low voltages a well–developed but smeared gap structure appears with maximum at 56 ± 5 mV. Between 4 K and 20 K the G–V curves are nearly temperature independent but at higher temperatures the tunneling behavior gradually disappears.

The effect of lowering the substrate temperature results in a change from metallic to tunneling junction behavior. An explanation is that the high substrate temperatures promote an interdiffusion or chemical reaction at the interface. This can be regarded as a layer with intermediate properties. This layer allows some permeability of the superconducting order parameter in the barrier so that the transmission coefficient is finite. Low substrate temperatures in contrast reduces such a reaction, therefore, the interface will be sharp an the order parameter should decay abruptly into the barrier. This effect was also confirmed with the value of the differential conductance in the normal state for the different samples. The superlattice with modulation (4/16) prepared at $T_s = 840°C$ has a value $G_n(V = 200\ mV)$ of 100 mS which results in approx. 14.3 mS per junction whereas the normal conductance of the sample with modulation (4/12) prepared at 760°C has a differential conductance at 200 mV of 14 mS i.e., 1.5 mS per junction. Despite a comparable barrier thickness the differential conductance of the first sample is almost an order of magnitude larger than the second one.

The interplay between superconductivity and magnetism was studied by the evolution of the two–magnon peak in $(YBa_2Cu_3O_{7-x})_4/(PrBa_2Cu_3O_{7-y})_m$ superlattices, with $m = 6$, 9 and 12 in collaboration with the group of applied physics of the university of Hamburg. Such a system represents an interesting scenario to study the competition between the order parameters, that are related to the antiferromagnetic and superconducting slabs only by adjusting the thickness of the respective layer. The dependence of the two–magnon excitation on the superlattices modulations shows a decrease of the line width as the antiferromagnetic $PrBa_2Cu_3O_{7-y}$ layer thickness decreases. The two–magnon spectra of the samples (4/12) and (4/9) share similar features with the spectrum of the sample $PrBa_2Cu_3O_{7-y}$, where the magnon damping decays strongly between between 300 K and 200 K and below 150 K saturates at approx. 180 cm^{-1}. On the other hand, the magnon damping of the sample $(YBa_2Cu_3O_{7-x})_4/(PrBa_2Cu_3O_{7-y})_6$ at 300 cm^{-1} at T = 150 K and below the critical temperature drops to 190 cm^{-1} i.e., the life time of the two magnon excitation increases. This observation is due to the loss of decay channels in the superconducting phase.

Bibliography

[1] R. A. Klemm, A. Luther, and M. R. Beasley. *Theory of the upper critical field in layered superconductors.* Phys. Rev. B **12**, 877 (1975).

[2] D. E. Prober, R. E. Schwall, and M. R. Beasley. *Upper critical fields and reduced dimensionality of the superconducting layered compounds.* Phys. Rev. B **21**, 2117 (1980).

[3] P. R. Broussard and T. H. Geballe. *Superconductivity and structure in sputtered Nb–Ta multilayers.* Phys. Rev. B **37**, 60 (1988).

[4] I. Banerjee, Q. S. Yang, C. M. Falco, and I. Schuller. *Anisotropic critical field in superconducting superlattices.* Phys. Rev. B **28**, 5037 (1983).

[5] W. E. Lawrence and S. Doniach. *Proceedings of the 12th International Conference on Low Temperature Physics, Kyoto, 1970*, edited by E. Kanda (Academic, Kyoto, 1971) p. 361.

[6] O. Brunner, J. -M. Triscone, L. Antognazza, M. G. Karkut, and Ø. Fischer. *Critical field anisotropy of artificial $YBa_2Cu_3O_{7-x}$ / $PrBa_2Cu_3O_{7-y}$ superlattices.* Physica B **165-166**, (1990) 469-470.

[7] K. Shimizu, H. Nobumaza, and T. Kawai. *Influence of the spacing of Cu–O_2 sheets on the superconducting transition temperature.* Supercond. Sci. Technol. **4**, (1991) 448–450.

[8] R. Kleiner, F. Steinmeyer, G. Kunkel, and P. Müller. *Intrinsic Josephson effects in $Bi_2Sr_2CaCu_2O_{10+y}$ single crystals.* Phys. Rev. Lett. **68**, 2394 (1992).

[9] Q. Li, X. Xi, X. D. Wu, A. Inam, S. Vadlamannati, W. L. McLean, T. Venkatesan, R. Ramesh, D. M. Hwang, J. A. Martínez, and L. Nazar.

Interlayer coupling in high–T_c superconductors probed by $YBa_2Cu_3O_{7-x}$ / $PrBa_2Cu_3O_{7-y}$ superlattices. Phys. Rev. Lett. **64**, 3086 (1990).

[10] R. Kleiner and P. Müller. *Intrinsic Josephson effects in high–T_c superconductor.* Phys. Rev. B **49**, 1327 (1994).

[11] A. Schattke. *PhD Thesis.* Johannes Gutenberg Universität–Mainz, 1998.

[12] J. Bardeen, L. N. Cooper, and J. R. Schriffer. *Theory of Superconductivity.* Phys. Rev. **108**, 1175 (1957).

[13] B. Batlogg, R. J. Cava, A. Jayaraman, R. B. van Dover, G. A. Kourouklis, S. Sunshine, D. W. Murphy, L. W. Rupp, H. S. Chen, A. White, K. T. Short A. M. Mujsce, and E. A. Rietman. *Isotope effect in the high–T_c superconductors $Ba_2YCu_3O_7$ and $Ba_2EuCu_3O_7$.* Phys. Rev. Lett. **58**, 2333 (1987).

[14] T. A. Faltens, W. K. Ham, S. W. Keller, K. J. Leary, J. N. Michaels, A. M. Stacy, H. –C. zur Loye, D. E. Morris, T. W. Barbee, L. C. Bourne, M. L. Cohen, S. Hoen, and A. Zettl. *Observation of and oxygen isotope shift in the superconducting transition temperature of $La_{1.85}Sr_{0.15}CuO_4$.* Phys. Rev. Lett. **59**, 915 (1987).

[15] M. Cyrot. *Superconductivity and high–T_c superconductors.* Ann. Phys. **10**, 75 (2001).

[16] E. L. Wolf. *Principles of electron tunneling spectroscopy.* New York, Oxford: Oxford University Press, 1989.

[17] A. Barone and G. Paterno. *Physics and Applications of the Josephson Effect.* New York, John Wiley & Sons, 1982.

[18] M. Tinkham. *Introduction to Superconductivity.* New York, McGraw–Hill, Inc. 1996.

[19] B. D. Josephson. *Possible new effects in superconductive tunneling.* Phys. Letters. **1**, 251 (1962).

[20] R. P. Feynman, R. B. Leighton, and M. Sands. *The Feynman Lectures on physics. 3: Quantum mechanics.* Addison–Wesley, Reading, MA 1965.

[21] D. E. McCumber. *Effect of ac impedance on dc voltage– current characteristics of superconductor weak–link junctions.* J. Appl. Phys. **39**, 3113 (1968).

[22] P. G. de Gennes. *Superconductivity of Metals and Alloys*. W. A. Benjamin, Inc. New York, 1966.

[23] G. E. Blonder, M. Tinkham, and T. M. Klapwijk. *Transition from metallic to tunneling regimes in superconducting microconstriction: Excess current, charge imbalance, and supercurrent conversion.* Phys. Rev. B **25**, 4515 (1982).

[24] A. P. van Gelder. *Energy Gaps in the Excitation Spectrum of a Superconductor.* Phys. Rev. **181**, 787 (1969).

[25] R. Kümmel. *Electronic Structure of the Intermediate State in Type–I Superconductor.* Phys. Rev. B **3**, 784 (1971).

[26] A. Hahn. *Quasiparticles in a Periodic Pair Potential: A Density of States Model for* $YBa_2Cu_3O_{7-x}$. Physica B **165–166**, 1065 (1990).

[27] U. Schüssler and R. Kümmel. *Andreev scattering, Josephson currents, and coupling energy in clean superconductor–semiconductor–superconductor junctions.* Phys. Rev. B **47**, 2754 (1993).

[28] H. Plehn, O. J. Wacker, and R. Kümmel. *Electronic structure of superconducting multilayers.* Phys. Rev. B **49**, 12140 (1994).

[29] S. E. Shafranjuk and T. Yamashita. *Minisubbands in electron excitation spectra of layered short–coherence–length superconductor.* Phys. Rev. B **54**, 15380 (1996).

[30] K. Nakajima, T. Arai, S. E. Shafranjuk, T. Yamashita, I. Tanaka, and H. Kojima. *Odd–gap spikes observed by tunneling spectroscopy for La–Sr–Cu–O single crystal.* Physica C **293**, (1997) 292.

[31] T. I. Baturina, D. R. Islamov, and Z. D. Kvon. *Subgap anomaly and above–energy–gap structure in chains of diffusive SNS juntions.* cond–matt/0202467.

[32] T. M. Klapwijk, G. E. Blonder, and M. Tinkham. *Explanation of subharmonic energy gap structures in superconducting contacts.* Physica C **109–110B**, (1982) 1657.

[33] M. Octavio, M. Tinkham G. E. Blonder, and T. M. Klapwijk. *Subharmonic energy gap structures in superconducting constrictions.* Phys. Rev. B **27**, 6739 (1983).

[34] J. C. Martínez, A. Schattke, G. Jakob, and H. Adrian. *Perpendicular transport properties of $YBa_2Cu_3O_{7-x}$ / $PrBa_2Cu_3O_{7-y}$ superlattices.* Physica B **284–288**, (2000) 553–554.

[35] M. Leskeä. *Chemical Vapor Deposition of high–T_c superconducting films.* Supercond. Sci and Technol. **6**, (1993) 627–656

[36] M. Schieber. *Deposition of high temperature superconducting films by physical and chemical methods.* J. Crystal Growth **109**, (1991) 401–417.

[37] I. Leon and I. Maissel. *Handbook of thin films technology.* New York, MacGraw–Hill, 1970.

[38] R. G. Humphreys, J. S. Satchell. N. G. Chew, J. A. Edwards, S. W. Goodyear, S. E. Blenkinsop, O. D. Dosser, and A. G. Cullis. *Physical vapor deposition techniques for the growth of $YBa_2Cu_3O_{7-x}$ thin films.* Supercond. Sci. Technol. **3**, (1990) 38–52.

[39] G. Jakob. *PhD Thesis.* Technische Hochschule Darmstadt, 1993.

[40] S. B. Qadri, L. E. Toth, M. Osofsky, S. Lawrence, D. U. Gubser, and S. A. Wolf. *X–ray identification of the superconducting high–T_c phase in the Y–Ba–Cu–O system.* Phys. Rev. B **35**, 7235 (1987).

[41] C. Allgeier, J. S. Schilling, and E. Amberger. *Meissner effect in Y–Ba–Cu–O and La–Sr–Cu–O high–temperature superconductors.* Phys. Rev. B **35**, 8791 (1987).

[42] R. Sum, H. P. Lang, and H. J. Güntherodt. *Scanning force microscopy study of single–crystal substrates used for thin–film growth of high–temperature superconcuctor.* Physica C **242**, (1995) 174–182.

[43] J. G. Wen, C. Traeholt, and H. W. Zandbergen. *Stacking sequence of $YBa_2Cu_3O_{7-x}$ thin films on $SrTiO_3$ substrate.* Physica C **205**, (1993) 354–362.

[44] J. Mannhart, D. Anselmetti, J. G. Bednorz, A. Catana, Ch. Gerber, K. A. Müller, and D. G. Schlom. *Correlation between J_c and screw dislocation density in sputtered $YBa_2Cu_3O_{7-x}$ films.* Z. Phys. B –Condensed Matter **86**, 177–181 (1992).

[45] D. G. Schlom, D. Anselmetti, J. G. Bednorz, R. F. Broom, A. Catana, T. Frey, Ch. Gerber, H. J. Güntherodt, H. P. Lang, and J. Mannhart. *Screw dislocation mediated growth of sputted and laser–ablated $YBa_2Cu_3O_{7-x}$ films.* Z. Phys. B –Condensed Matter **86**, 163–175 (1992).

[46] J. Burger, M. Lippert, W. Dorsch, P. Bauer, and G. Saemann–Ischenko. *Observation of the early stages of growth and the formation of growth spirals in epitaxial $YBa_2Cu_3O_{7-x}$ thin films by AFM.* Appl. Phys. A **58**, 49–56 (1994).

[47] E. Sodtke, C. Andrzejak, D. Guggi, and Y. Xu. *Preparation of a–axis oriented $YBa_2Cu_3O_{7-x}$ and $PrBa_2Cu_{3-x}Ga_xO_7$ thin films.* Physica C **180**, (1991) 50–53.

[48] W. Eidelloth and R. L. Sandstrom. *Wet etching of gold films compatible with high T_c superconducting thin films.* Appl. Phys. Lett. **59**, 1632 (1991).

[49] N. W. Ashcroft and N. D. Mermin. *Solid States Physics.* Philadelphia, Saunders College, 1976.

[50] Y. Le Page, T. Siegrist, S. A. Sunshine, L. F. Schneemeyer, D. W. Murphy, S. M. Zahurak, J. V. Waszczak, W. R. McKinnon, J. M. Tarascon, G. W. Hull, and L. H. Greene. *Structural properties of $Ba_2RCu_3O_7$ high–T_c superconductors.* Phys. Rev. B **36**, 3617 (1987).

[51] T. Hahn. *Diploma–Thesis.* Technische Hochschule Darmstadt, 1992.

[52] E. E. Fullerton, I. K. Schuller, H. Vanderstraeten, and Y. Bruynseraede. *Structural Refinement of Superlattices from X–ray Diffraction.* Phys. Rev. B **45**, 9292 (1992).

[53] A. R. Elshabini–Riad, F. D. Barlow. *Thin Film Technology Handbook.*

[54] M. Engelmann. *Diploma–Thesis.* Johannes Gutenberg Universität–Mainz, 1997.

[55] J. G. Adler and J. E. Jackson. *System for observing small nonlinearities in tunnel junctions.* Rev. Sci. Inst. **37**, 1049 (1966).

[56] T. Becherer. *PhD Thesis.* Technische Hochschule Darmstadt, 1994.

[57] M. Jourdan. *PhD Thesis.* Johannes Gutenberg Universität–Mainz, 1999.

[58] U. Poppe, P. Prieto, J. Schubert, H. Soltner, K. Urban, and Ch. Buchal. *Epitaxial multilayers of $YBa_2Cu_3O_{7-x}$ and $PrBa_2Cu_3O_{7-y}$ as possible basis for superconducting electronics devices.* Solid State Comm. **71**, 569 (1989).

[59] K. Char, L. Antognazza, and T. H. Geballe. *Study of interface resistance in epitaxial $YBa_2Cu_3O_{7-x}$ /barrier/$YBa_2Cu_3O_{7-x}$ junction.* Appl. Phys. Lett. **63**, 2420 (1993).

[60] K. Char, M. S. Colclough, T. H. Geballe, and K. E. Myers. *High T_c superconductor–normal–superconductor Josephson junctions using $CaRuO_3$ as the metallic barrier.* Appl. Phys. Lett. **62**, 196 (1993).

[61] Q. Y. Ying and C. Hilbert. *All–$YBa_2Cu_3O_{7-x}$ trilayer tunnel junctions with Sr_2AlTaO_6 barrier.* Appl. Phys. Lett. **65**, 3005 (1994).

[62] S. Hontu, N. Mukai, J. Ishii, T. Kawai, and S. Kawai. *Epitaxial growth and properties of $YBa_2Cu_3O_{7-x}$ / $LaSrGaO_4$/ $YBa_2Cu_3O_{7-x}$ trilayer structures.* Appl. Phys. Lett. **64**, 779 (1994).

[63] Y. Xu and W. Guan. *Hopping conductivity in the $PrBa_2Cu_{3-x}O_{7-y}$ system.* Physica C **206**, (1993) 59-69.

[64] U. Tipprach, T. P. Chen, J. L. Wagner, K. Wu, Q. Y. Chen, J. T. Wang, H. C. Yang, and H. E. Horng. *Fabrication and transport studies on $PrBa_2(Cu_{1-x}M_x)_3O_7$: M = Ga, Zn and Co.* Physica C **364-365**, (2001) 404-407.

[65] B. Ghyselen, M. A. Bari, E. J. Tarte, M. G. Blamire, R. E. Somekh, Y. Yan, and J. E. Evetts. *Josephson junctions based on c–axis oriented YBaCuO/ PrBaCuO/ YBaCuO trilayers.* Physica C **230**, (1994) 327-339.

[66] E. Fujimoto, H. Sato, T. Yamada, and H. Akoh. *All $YBa_2Cu_3O_{7-x}$ trilayers junctions with $YBa_2Cu_3O_{7-x}$ wiring layers.* Appl. Phys. Lett. **80**, 3985 (2002).

[67] B. Ghyselen, M. A. Bari, E. J. Tarte, M. G. Blamire, R. E. Somekh, Y. Yan, and J. E. Evetts. *Josephson junctions based in c–axis oriented YBaCuO/ PrBaCuO /YBaCuO trilayers.* Physica C **230**, (1994) 327-339.

[68] P. G. de Gennes. *Boundary Effects in Superconductors.* Rev. Mod. Phys. **36**, 225 (1964).

[69] G. Deutscher and P. G. de Gennes. *Superconductivity, Vol II.* (R. D. Parks. eds) Marcel Dekker Inc. New York, 1969, Chap 17.

[70] R. P. Robertazzi, A. W. Kleinsasser, R. B. Laibowitz, R. H. Koch, and K. G. Stawiasz. *In situ $Ag/YBa_2Cu_3O_{7-x}$ contacts for superconductor–normal metal–superconductor devices.* Phys. Rev. B **46**, 8456 (1992).

[71] M. Y. Kupriyanov and K. K. Likharev. *Toward the quantitative theory of the high–T_c Josephson junction.* IEEE Trans. Mag. **27**, 2460 (1991).

[72] G. Deutscher and R. W. Simon. *On the proximity effect between normal metals and cuprates superconductors.* J. Appl. Phys. **69**, 4137 (1991).

[73] Y. M. Boguslavskij, J. Gao, A. J. H. M. Rijnders, D. Terpstra, G. J. Gerritsma, and H. Rogalla. *Transport processes in $YBa_2Cu_3O_{7-x}$ /$PrBa_2Cu_3O_{7-y}$ /$YBa_2Cu_3O_{7-x}$ ramp type Josephson junctions.* Physica C **194**, (1992) 268-276.

[74] H. Srikanth and A. K. Raychaudhuri. *Microshort–to–tunneling transition in Au–$YBa_2Cu_3O_{7-x}$ single–crystal point contacts.* Phys. Rev. B **45**, 383 (1992).

[75] W. F. Brinkman, R. C. Dynes, and J. M. Rowell. *Tunneling conductance of asymmetrical barriers.* J. Appl. Phys. **41**, 1915 (1970).

[76] J. G. Simmons. *Generalized formula for the electric tunnel effect between similar electrodes separated by a thin insulating film.* J. Appl. Phys. **34**, 1793 (1963).

[77] A. M. Cucolo, R. D. Leo, and A. Nigro. *An analysis of the natural tunnel barrier in liquid–etched Y–Ba–Cu–O systems.* Physica C **207**, (1993) 21-24.

[78] D. J. van Harlingen. *Phase–sensitive tests of the symmetry of the pairing state in the HTSC's–Evidence for $d_{x^2-y^2}$ symmetry.* Rev. Mod. Phys. **67**, 515 (1995).

[79] M. Convington, M. Aprili, E. Paraoanu, and L. H. Greene. *Observation of surface–induced broken time–reversal symmetry in $YBa_2Cu_3O_{7-x}$ tunnel junctions.* Phys. Rev. Lett. **79**, 277 (1997).

[80] T. Löfwander, V. S. Shumeiko, and G. Wendin. *Andreev bound states in high–T_c superconducting junctions.* Supercond. Sci. Technol. **14**, (2001) R53.

[81] L. Alff, S. Kleefisch, U. Schoop, M. Zittartz, T. Kemen, T. Bauch, A. Marx, and R. Gross. *Andreev bound states in high temperature superconductors.* Eur. Phys. J. B. **5**, 423 (1998).

[82] J. Lesueur, L.H. Greene, W. L. Feldmann, and A. Inam. *Zero bias anomalies in $YBa_2Cu_3O_{7-x}$ tunnel junctions.* Physica C **191**, (1992) 325–332.

[83] O. Madelung. *Introduction to the solid state theory.* Springer Verlag, Berlin Heidelberg, 1996.

[84] P. W. Anderson. *Localized magnetic states and Fermi–surface anomalies in tunneling.* Phys. Rev. Lett. **17**, 95 (1966).

[85] J. A. Appelbaum. *Exchange model of zero–bias tunneling anomalies.* Phys. Rev. **154**, 633 (1967).

[86] A. F. G. Wyatt and R. H. Wallis. *Exchange scattering in Ti–doped Al/Al oxide/Ag tunnel junctions: I. Zero magnetic field.* J. Phys. C: Solid State Phys. **7**, 1279 (1974).

[87] A. M. Cucolo and R. Di Leo. *Zero–bias anomalies in high–T_c superconductor tunnel junctions.* Phys. Rev. B **47**, 2916 (1993).

[88] R. H. Wallis and A. F. G. Wyatt. *Exchange scattering in Ti–doped Al/Al oxide/Ag tunnel junctions: II. Magnetic field.* J. Phys. C: Solid State Phys. **7**, 1293 (1974).

[89] S. Skanthakumar, J. W. Lynn, N. Rosov, G. Cao, and J. E. Crow. *Observation of magnetic order in $PrBa_2Cu_3O_{7-y}$.* Phys. Rev. B **55**, R3406 (1997).

[90] J. M. Triscone, Ø. Fischer, O. Brunner, L. Antognazza, and A. D. Kent. *$YBa_2Cu_3O_{7-x}$ / $PrBa_2Cu_3O_{7-y}$ Superlattices: Properties of ultrathin superconducting layers separated by insulating layers.* Phys. Rev. Lett. **64**, 804 (1990).

[91] Ø. Fischer, J. M. Triscone, L. Antognazza, O. Brunner, A. D. Kent, L. Mieville, and M. G. Karkut. *Artificially prepared $YBa_2Cu_3O_{7-x}$ / $PrBa_2Cu_3O_{7-y}$ superlattices: growth and superconducting properties.* J. of the Less–Common Metals **164–165**, (1990) 257–268.

[92] L. Antognazza, J. M. Triscone, O. Brunner, M. G. Karkut, and Ø. Fischer. *Superconducting critical temperatures of artificial $YBa_2Cu_3O_{7-x}$ / $PrBa_2Cu_3O_{7-y}$ superlattices.* Physica B **165–166**, (1990) 471–472.

[93] I. Bozovic and J. N. Eckstein. *Superconductivity in cuprate superlattices (Physical properties of high temperature superconductors vol. 5)* (ed. G. M. Ginsberg.) Singapore: World Scientific, 1996.

[94] G. Jakob, Th. Hahn, C. Stölzel, C. Tomé–Rosa, and H. Adrian. *Transport properties of $YBa_2Cu_3O_{7-x}$/$PrBa_2Cu_3O_{7-y}$superlattices.* Europhys. Lett. **19**, 135 (1992).

[95] G. Jakob, M. Schmitt, Th. Hahn, C. Stölzel, and H. Adrian. *Superconductivity of $YBa_2Cu_3O_{7-x}$ /$PrBa_2Cu_3O_{7-y}$ superlattices.* IEEE Trans. Appl. Supercond. **3**, 1624 (1993).

[96] G. Jakob, Th. Hahn, Th. Kluge, P. Wagner, and H. Adrian. *Characterization of $YBa_2Cu_3O_{7-x}$ / $PrBa_2Cu_3O_{7-y}$ superlattices.* J. Supercond. **7**, 197 (1994).

[97] D. P. Norton, D. H. Lowndes, S. J. Pennycook, and J. D. Budai. *Depression and broadening of the superconducting transition in superlattices based on $YBa_2Cu_3O_{7-x}$: Influence of the barrier layers.* Phys. Rev. Lett. **67**, 1358 (1991).

[98] L. M. Wang, H. C. Yang, and H. E. Horng. *Normal–state transport properties of $YBa_2Cu_3O_{7-x}$ / $PrBa_2Cu_3O_{7-y}$ superlattices.* Phys. Rev. B **56**, 6231 (1997).

[99] D. H. Lowndes, D. P. Norton, and J. D. Budai. *Superconductivity in nonsymmetric epitaxial $YBa_2Cu_3O_{7-x}$/ $PrBa_2Cu_3O_{7-y}$ superlattices: The superconducting behavior of Cu–O bilayers.* Phys. Rev. Lett. **65**, 1160 (1990).

[100] L. I. Glazman and K. A. Matveev. *Inelastic tunneling across thin amorphous films.* Sov. Phys. JETP. **67**, 1276 (1988).

[101] Y. Xu, D. Ephron, and M. R. Beasley. *Directed inelastic hopping of electrons through metal–insulator–metal tunnel junctions.* Phys. Rev. B **52**, 2843 (1995).

[102] J. Yoshida and T. Nagano. *Tunneling and hopping conduction via localized states in thin $PrBa_2Cu_3O_{7-y}$ barriers.* Phys. Rev. B **55**, 11860 (1997).

[103] M. A. Bari, F. Baudenbacher, J. Santiso, E. J. Tarte, J. E. Evetts, and M. G. Blamire. *C–axis tunneling in $YBa_2Cu_3O_{7-x}$ trilayer junctions with $PrBa_2Cu_3O_{7-y}$ barrier.* Physica C **256**, (1996) 227–235.

[104] R. Dömel, C. Horstmann, M Siegel, and A. I. Braginski. *Resonant tunneling transport across $YBa_2Cu_3O_{7-x}$ –$SrRuO_3$ interfaces.* Appl. Phys. Lett. **67**, 1775 (1995).

[105] J. Yoshida, T. Nagano, and T. Hashimoto. *Characterization of localized states in thin $PrBa_2Cu_3O_{7-y}$ tunnel barriers.* J. Low Temp. Phys. **106**, 327 (1997).

[106] P. J. Thomas, J. C. Fenton, G. Yang, and C. E. Gough. *Intrinsic c–axis transport in 2212–BSCCO.* Physica C **341–348**, (2000) 1547–1550.

[107] A. Yurgen, D. Winkler, Y. M. Zhang, N. Zavaritsky, and T. Claeson. *Intrinsic Josephson tunnel junctions fabricated on the surfaces of Bi2212 single crystals by photolithography.* Physica C **235–240**, (1994) 3269–3270.

[108] K. Schlenga, G. Hechtfischer, R. Kleiner, W. Walkenhorst, P. Müller, H. L. Johnson, M. Veith, W. Brodkorb, and E. Steinbeiss. *Subgap structures in intrinsic Josephson junctions of $Tl_2Ba_2Ca_2Cu_3O_{10-y}$, and $Bi_2Sr_2CaCu_2O_{8+y}$* Phys. Rev. Lett. **76**, 4943 (1996).

[109] V. N. Zavaritsky. *Intrinsic tunneling or Joule heating?.* cond–mat/0306081.

[110] V. N. Zavaritsky. *Heating–free I–V of the "intrinsic" Josephson effect.* cond–mat/0309429.

[111] V. M. Krasnov. *Properties of small HTSC mesa structures: common problems of interlayer coupling.* cond–mat/0109079.

[112] V. M. Krasnov, A. Yurgens, D. Winkler, and P. Delsign. *Self–heating in small mesa structures.* J. Appl. Phys. **89**, 5578 (2001).

[113] J. M. Valles, Jr., R. C. Dynes, A. M. Cucolo, M. Gurvitch, L. F. Schneemeyer, J. P. Garno, and J. V. Waszczak. *Electron tunneling into single crystal of* $YBa_2Cu_3O_{7-x}$. Phys. Rev. B **44**, 11986 (1991).

[114] P. W. Anderson and Z. Zou. *"Normal" tunneling and "normal" transport: Diagnostic for the Resonanting–Valence–Bond state.* Phys. Rev. Lett. **60**, 132 (1988).

[115] C. M. Varma, P. B. Littlewood, S. Schmitt–Rink, E. Abrahams, and A. E. Ruckenstein. *Phenomenology of the normal state of Cu–O High–Temperature superconductors.* Phys. Rev. Lett. **63**, 1996 (1989).

[116] J. C. Phillips. *States in the superconductive energy gap of high–*T_c *cuprates.* Phys. Rev. B **41**, 8968 (1990).

[117] J. R. Kirtley and D. J. Scalapino. *Inelastic–tunneling model for the linear conductance background in the high–*T_c *superconductors.* Phys. Rev. Lett. **65**, 798 (1990).

[118] J. R. Kirtley. *Inelastic transport through normal-metal–superconductor interfaces.* Phys. Rev. B **47**, 11379 (1993).

[119] I. Iguchi and Z. Wen. *Tunnel gap structures and tunneling model of the anisotropic YBaCuO/I/Pb junctions.* Physica C **178**, (1991) 1.

[120] S. Uchida, T. Ido, H. Takagi, T. Arima, Y. Tokura, and S. Tajima. *Optical spectra of* $La_{2-x}Sr_xCuO_4$*: Effect of carrier doping on the electronic structure of the* CuO_2 *plane.* Phys. Rev. B **43**, 7942 (1991).

[121] D. M. Newns, C. C. Tsuei, P. C. Pattnaik, C. L. Kane, C. C. Chi, H. R. Krishnamurthy, and M. Daumling. *Cuprates: Back to the Fermi surface.* Mat. Res. Soc. Symp. Proc. **275**, 3 (1992).

[122] A. Damascelli, Z. Hussain, and Z. –X. Shen. *Angle–resolved Photoemission studies of the cuprate superconductors.* Rev. Mod. Phys. **75**, 473 (2003).

[123] E. Manousakis. *The spin–*$\frac{1}{2}$ *Heisenberg antiferromagnet on a square lattice and its application to the cuprous oxides.* Rev. Mod. Phys. **63**, 1 (1991).

[124] R. J. Elliott and M. F. Thorpe. *The effects of magnon–magnon interaction on the two–magnon spectra of antiferromagnets.* J. Phys. C: Solid St. Phys. **2**, 1630 (1969).

[125] J. B. Parkinson. *Optical properties of layer antiferromagnets with K_2NiFe_4 structure.* J. Phys. C: Solid St. Phys. **2**, 2012 (1969).

[126] R. Lui, C. Thomsen, K. Kress, M. Cardona, B. Gegenheimer, F. W. de Wette, J. Prade, and A. D. Kulkarni. *Frequencies, eigenvectors, and single–crystal selection rules of k = 0 phonons in $YBa_2Cu_3O_{7-x}$; Theory and experiment.* Phys. Rev. B **37**, 7971 (1988).

[127] M. Cardona, R. Lui, C. Thomsen, M. Bauer, L. Genzel, W. König, U. Amador, M. Barahona, F. Fernández, C. Otero, and R. Sáenz. *Infrared and Raman spectra of the new superconducting cuprate perovskites $MBa_2Cu_3O_7$, M = Nd, Dy, Er, Tm.* Solid State Commun. **65**, 71 (1988).

[128] K. B. Lyons, P. A. Fleury, L. F. Schneemeyer, and J. V. Waszczak. *Spin fluctuations and superconductivity in $YBa_2Cu_3O_{7-x}$.* Phys. Rev. Lett. **60**, 732 (1988).

[129] A. Chubukov and D. M. Frenkel. *Resonant two–magnon Raman scattering in antiferromagnetic insulators.* Phys. Rev. Lett. **74**, 3057 (1995).

[130] K. B. Lyons, P. E. Sulewski, P. A. Fleury, H. L. Carter, A. S. Cooper, G. P. Espinosa, Z. Fisk, and S. W. Cheong. *High–energy spin and charge excitation in La_2CuO_4.* Phys. Rev. B **39**, 9693 (1989).

[131] M. Rübhausen, C. T. Rieck, N. Dieckmann, K. –O. Subke, A. Bock, and U. Merkt. *Inelastic light scattering at high–energy excitations in doped cuprates superconductors.* Phys. Rev. B **56**, 14797 (1997).

[132] D. Budelmann, J. Holmlund, J. Andreasson, H. Rodríguez, J. Bäckström, L. Börjesson, H. Adrian, U. Merkt, and M. Rübhausen. *Antiferromagnetic and superconducting proximity effects in $YBa_2Cu_3O_{7-x}$ /$PrBa_2Cu_3O_{7-y}$ superlattices.* Phys. Rev. B **67**, 140507 (2003).

[133] D. Budelmann. *PhD. Thesis.* Institut für Angewandte Physik, University of Hamburg, 2003.

Danksagung

Besonders danken möchte ich Herrn Prof. Dr. H. A. für die Möglichkeit, meine Dissertation in seiner sehr gut ausgestatteten Arbeitsgruppe durchführen zu dürfen. Darüber hinaus danke ich ihm für die zahlreichen Diskussionen und Anregungen im Verlauf dieses Projekts, sowie für die Korrekturen und Anmerkungen zu dieser Arbeit.

Ein besonderer Dank geht auch an Herrn Prof. Dr. M. H. für seine Bereitschaft zu Diskussionen, seine zahlreichen Anregungen, die zum Gelingen dieser Arbeit beigetragen haben und das sorgfältige Korrekturlesen der Kap. 3 und 4.

Ebenfalls bedanken möchte ich mich bei Herrn Dr. Habil. G. J. für die Hilfe bei Fragen zur Herstellung und Charkterisierung der Übergitter sowie für das kritische Lesen des Manuskripts. Weiterhin danke ich Herrn PD. Dr. M. J. für das Korrekturlesen sowie die Unterstützung im Rahmen der Tunnelspektroskopie.

Für seine Betreuung und Unterstützung in der ersten Zeit meiner Promotion bedanke ich mich bei Herrn Dr. M. B..

Ein herzlicher Dank geht an Herrn Dr. D. B. für die gute Zusammenarbeit und viele wertvolle Diskussionen zu Frage der Raman Spektroskpie.

Ein Dankeschön ebenfalls an:

– Dipl. Phys. J. O. für seine deutschsprachige Unterstützung.

– Dipl. Phys. N. A. für ihre Hilfe mit der BTK Simulation.

– Dipl. Phys. O. S., A. Z., sowie A. C., M. F. und alle Mitglieder der Arbeitsgruppe für das gute Klima und die angenehme Arbeitsatmosphäre.

Bei Señor Dipl. -Ing. J. H. bedanke ich mich für seine Hilfe bei allen technischen Fragen und der Lösung zahlreicher Probleme. Frau A. D. danke ich für ihre Hilfe bei der Anfertigung von REM Aufnahmen und Herrn Dipl. Biol. R. “el” B. gilt mein Danke für seine Hilfe mit den 3D Bildern.

Darüber hinaus möchte ich mich bei Herrn G. und Herrn G. für die Versorgung mit flüssigem Helium und beim Werkstatt–Team für die Anfertigung des benötigen Arbeitsmaterials bedanken.

Für die Vorbereitung der Zusammensetzung der Targets danke ich Herrn J. S.

Ganz besonders danke ich meiner Freundin C. für ihre Unterstützung und viele aufmunternde Worte.

Eidesstattliche Erklärung

Hiermit erkläre ich an Eides Statt, daß ich die vorliegende Arbeit selbstsändig und nur unter Verwendung der angegebenen Hilfsmittel angefertigt habe.

Bisher habe ich noch keinen Promotionsversuch unternommen.

Mainz, im Juli 2004